**Boston University**

**OpenBU** **http://open.bu.edu**

Theses & Dissertations Boston University Theses & Dissertations

2017

# Optical tracking of nerve activity using intrinsic changes in birefringence

https://hdl.handle.net/2144/20825

*Boston University*

BOSTON UNIVERSITY

COLLEGE OF ENGINEERING

Dissertation

# OPTICAL TRACKING OF NERVE ACTIVITY USING INTRINSIC CHANGES IN BIREFRINGENCE

by

**ALI H. BADREDDINE**

B.S., Vanderbilt University, 2009
M.S., Boston University, 2013

Submitted in partial fulfillment of the

requirements for the degree of

Doctor of Philosophy

2017

© 2017 by
ALI H. BADREDDINE
All rights reserved

Approved by

First Reader _____

Irving J. Bigio, PhD
Professor of Electrical and Computer Engineering
Professor of Biomedical Engineering
Professor of Medicine

Second Reader _____

Jerome C. Mertz, PhD
Professor of Biomedical Engineering

Third Reader _____

Xue Han, PhD
Assistant Professor of Biomedical Engineering
Assistant Professor of Pharmacology & Experimental Therapeutics

Fourth Reader _____

Darren Roblyer, PhD
Assistant Professor of Biomedical Engineering

Fifth Reader _____

Jen-Wei Lin, PhD
Associate Professor of Biology

ACKNOWLEDGEMENTS

Traveling through the long course of a PhD program requires not just perseverance, but the concerted efforts of everyone around you. Without others to fund you, feed you, advise you, lecture you, challenge you, support you, and just make you laugh, it's easy to find yourself lost in the fog of graduate school. Help is more a necessity than an aid, and the following have contributed substantially to getting me to this point.

This work would not have been possible without the NIH/NIBIB grant (R21 EB007943) that initially funded it, and the Biomedical Engineering Department for their contributions. The Quantitative Biology and Physiology program is to be thanked for giving me the opportunity to travel to a conference.

The members of the Biomedical Optics Lab over the years have given me the knowledge and opportunity that allowed me to obtain a PhD. Professor Irving Bigio provided me with countless guidance and utmost patience that was more than I deserved. The former student Dr. Kurt Schoener paved a path for my work. Dr. Ousama A'amar could be found many times over the years toiling away on the cables in my setups and showing me how to improve my electronics. Dr. Katherine Calabro and Dr. Christine Mulvey gave me a lot of early support and guidance. Bobby Liu has been an invaluable source of knowledge and support that only a fellow grad student in your lab can provide. Joseph Angelo and Mark Bucklin had provided me with help in my early research while doing rotations in the lab. Anna Slatterty was an exceptional summer student who helped me obtain data presented in Aim 3.

My committee members, Professors Jerome Mertz, Xue Han, Darren Roblyer, and Jen-Wei Lin, are to be thanked for their helpful advice and continual guidance. Multiple times, their input has given me the opportunity to attempt new areas of research. A special thanks is given to Professor Han for helping me obtain samples for Aim 3. Many thanks also are owed to Kimberly Young, Michael Brown, Dr. Michele Ferrante, Susie Cha, and Dr. Howard Griffin for their help in allowing me to use their research specimen to obtain samples for my work.

As equally important as the scientific help is the emotional support of loved ones. My mother Mary served as a source of strength and encouraged me when I was troubled not just during the PhD, but throughout my life. Without her devotion and care, I would never have had the strength to make it this far. My uncle Joe and aunt Candice here in Massachusetts were available whenever I needed help or to just visit. A final thanks goes to my wife Yasha, whose unwavering, unconditional love and support gave me the final boost of confidence and energy needed to reach this point.

**OPTICAL TRACKING OF NERVE ACTIVITY USING**

**INTRINSIC CHANGES IN BIREFRINGENCE**

**ALI H. BADREDDINE**

Boston University, College of Engineering, 2017

Major Professor: Irving J. Bigio, PhD, Professor of Electrical and Computer Engineering, Professor of Biomedical Engineering, Professor of Medicine

ABSTRACT

Changes in birefringence (or dynamic birefringence) provide an arguably cleaner method of measuring IOS as compared to scattering methods. Other imaging methods have substantial limitations. Nerves inherently exhibit a static (rest condition) birefringence that is associated with the structural anisotropies of axonal protein filaments, membrane phospholipids and proteins, as well as surrounding tissues, which include Schwann cells and axon sheaths. The dynamic birefringence, or "crossed-polarized signal" (XPS), in neurons arises from activity in axons and occurs with a rapid momentary change, typically a decrease, in the birefringence when action potentials (APs) propagate along them.

We improved the signal-to-noise to make detecting this signal an easier task, and present the XPS as a viable candidate for detecting AP activity in anisotropic nervous tissue. Our data collectively serves as a strong indication that there is a capacitive-charging-like effect directly inducing a gradual recovery (long tail) of the XPS to baseline, and also causing a smoothing of the XPS trace. A setup was constructed that successfully demonstrated the feasibility of tracking propagating compound APs in a

peripheral nerve using the XPS. We made significant progress in the attempt to investigate birefringence of myelination. For the first time, the XPS in a myelinated tissue was detected, and it appears to be bipolar in nature. Further work in investigating the nature of this signal is needed, and is currently underway.

Since changes in birefringence in neurons are associated instantaneously with electrophysiological phenomena, they are well-suited for fast imaging of propagating action potentials in neuronal tissue. In summary, imaging based on polarization sensing of changes in birefringence offers promise for an improved noninvasive method of detecting and tracking AP activity in myelinated and unmyelinated nerves and could be designed for pre-clinical and surgical applications.

CONTENTS

List of Figures ..... xi
List of Abbreviations ..... xv
Chapter 1. Introduction ..... 1
Chapter 2. Background ..... 6
2.1. Introduction ..... 6
2.2. Light polarization and birefringence ..... 8
2.2.1. Light polarization and the electric field ..... 8
2.2.2. Uniaxial Birefringence ..... 9
2.3. Experimental specimen tissue structures ..... 11
2.3.1. Unmyelinated peripheral nerves ..... 11
2.3.2. Myelinated peripheral nerves ..... 13
2.4. 'Static' birefringence in nervous tissue ..... 16
2.4.1. Birefringence of the axon/nerve ..... 16
2.4.2. Myelination and birefringence ..... 18
2.4.3. Mouse brain slices ..... 20
2.5. The 'dynamic' birefringence signal in unmyelinated nerves ..... 21
2.5.1. Action potentials (APs) and electric field changes ..... 21
2.5.2. Lawrence Cohen's work on squid giant axons and crab leg nerves ..... 23
2.6. Exploring the origins and characteristics of the birefringence signals in unmyelinated nerves ..... 24
2.6.1. Lawrence Cohen and squid giant axons ..... 24
2.6.2. Ichiji Tasaki ..... 28
2.6.3. David Landowne ..... 28
2.6.4. David Rector ..... 28
2.6.5. Our lab (Kurt Schoener) (Schoener 2010) ..... 32
Chapter 3. Aim 1: Improving signal-to-noise and further characterizing the birefringence signal ..... 35
3.1. Introduction ..... 35
3.1.1. Part 1: Improving methods and SNR ..... 35
3.1.2. Part 2: Further characterizing the XPS ..... 37

3.2. General methods ..... 38
3.3. Part 1: Improvements to methods and SNR of the birefringence signal ..... 42
3.3.1. Nerve trunk size and XPS ..... 42
3.3.2. Illumination field size and XPS ..... 43
3.3.3. Use of quarter waveplate to reduce static birefringence ..... 44
3.3.4. Improved cable shielding and grounding ..... 45
3.3.5. Improved enclosure/shielding and electronic setup ..... 46
3.3.6. Use of anti-vibration materials in setup ..... 47
3.3.7. Stability and output of light source ..... 48
3.3.8. Digital filtering ..... 50
3.3.9. Discussion ..... 51
3.4. Part 2: Further characterizing the birefringence signal in lobster walking leg nerves ..... 53
3.4.1. Revisiting wavelength dependence of the XPS ..... 53
3.4.2. Reassessment of the XPS peak and gradual recovery timecourse ..... 55
3.4.3. Arrival-time-based AP model of the XPS ..... 57
3.4.4. Correlation with electrical recording ..... 61
3.4.5. Live and 'dead' nerve XPS response comparison ..... 62
3.4.6. Linear electro-optic response ..... 64
3.4.7. Sinusoidal electric fields ..... 67
3.4.8. Discussion ..... 70
3.5. Aim 1 Conclusions ..... 76
Chapter 4. Aim 2: "Real-time" tracking of the birefringence signal ..... 77
4.1. Introduction ..... 77
4.2. General methods ..... 78
4.3. Repeated-stimulus-averaged tracking ..... 83
4.4. Extracted "real-time" single stimulus tracking ..... 85
4.5. Varying stimulus frequency and amplitude ..... 87
4.6. Discussion ..... 89
4.7. Aim 2 Conclusions ..... 91
Chapter 5. Aim 3: Myelinated tissue and the birefringence signal ..... 92

5.1. Introduction ..... 92
5.2. Mammalian hippocampal neuron cultures ..... 93
5.2.1. Methods ..... 93
5.2.2. Results and analysis ..... 95
5.3. Mouse brain slices ..... 96
5.3.1. Specific background and methods ..... 96
5.3.2. Results and analysis ..... 101
5.4. Songbird laryngeal nerve ..... 104
5.4.1. Methods ..... 104
5.4.2. Results and analysis ..... 106
5.5. Mouse sciatic nerve ..... 106
5.5.1. Extraction methods ..... 106
5.5.2. Investigating static birefringence under a modified DIC microscope ..... 108
5.5.3. Manipulating the static birefringence intensity using a quarter waveplate ..... 118
5.5.4. Measuring the XPS ..... 122
5.6. Discussion ..... 129
5.7. Aim 3 Conclusions ..... 131
Chapter 6. Conclusions ..... 132
6.1. Summary of Specific Aims ..... 132
6.2. Future Directions ..... 134
6.3. Final conclusion ..... 135
References ..... 136
VITA ..... 141

LIST OF FIGURES

Figure 2-1. Depiction of light polarization. ..... 9

Figure 2-2. Depictions of birefringence. ..... 10

Figure 2-3. Birefringent example from our setup. ..... 11

Figure 2-4. Furusawa's pullout method for lobster walking leg nerve (Wininger et al. 2009). ..... 12

Figure 2-5. Cross sections of the lobster walking leg nerve (Darin De Lorenzo et al. 1968). ..... 12

Figure 2-6. Horseshoe crab lateral optic nerve cross section (Fahrenbach 1971). ..... 13

Figure 2-7. Myelination. ..... 14

Figure 2-8. Laryngeal nerve (da Silva et al. 2016). ..... 15

Figure 2-9. Mouse sciatic nerve cross section. ..... 16

Figure 2-10. Direction of polarization to maximize birefringence signal. ..... 17

Figure 2-11. Simplest setup for detecting birefringence. ..... 18

Figure 2-12. Birefringence of myelinated nerve (de Campos Vidal et al. 1980). ..... 19

Figure 2-13. Sciatic nerve myelin and collagen birefringence in treated nerves (Maturana et al. 2013). ..... 20

Figure 2-14. Schaffer collaterals of mouse brain slice. ..... 21

Figure 2-15. Depiction of action potential. ..... 22

Figure 2-16. The first reported change in birefringence from action potentials (Cohen et al. 1968). ..... 23

Figure 2-17. Demonstration of birefringence over other optical signals (Cohen et al. 1970). ..... 25
Figure 2-18. Location of the changes in birefringence in an axon (Cohen et al. 1970). .. 26
Figure 2-19. Voltage-clamped squid giant axon shows Kerr effect (Cohen et al. 1970). 27
Figure 2-20. A depiction of the windowed chamber and birefringence timecourses (Carter et al. 2004). ..... 29
Figure 2-21. Single-pass trial of changes in birefringence (Carter et al. 2004). ..... 30
Figure 2-22. Comparison of VSD, BIR and 90S signals (Foust et al. 2008). ..... 31
Figure 2-23. Custom nerve chamber designed in our lab (Schoener 2010). ..... 32
Figure 2-24. Measurements of the XPS as a function of distance (Schoener 2010). ..... 33
Figure 2-25. A comparison of the lateral optic nerve with the walking leg nerve (Badreddine et al. 2015). ..... 34
Figure 3-1. Simple diagram of setup and nerve chamber (Badreddine et al. 2015). ..... 40
Figure 3-2. New custom-built system dual enclosures. ..... 47
Figure 3-3. Vibration noise. ..... 48
Figure 3-4. Stability of light sources ..... 49
Figure 3-5. Testing wavelength dependence of the XPS. ..... 55
Figure 3-6. Features of XPS as a function of distance (Badreddine et al. 2015). ..... 57
Figure 3-7. AP model comparison to distance-based XPS peak and recovery timecourse (Badreddine et al. 2015). ..... 60
Figure 3-8. XPS overlaid with the electrical recordings. ..... 62

Figure 3-9. XPS response at stimulus site to applied fast current pulses (Badreddine et al. 2015). ..... 64

Figure 3-10. XPS relationship to applied electric field magnitudes (Badreddine et al. 2015). ..... 66

Figure 3-11. XPS in response to sinusoidal applied fields. ..... 68

Figure 3-12. XPS magnitude and phase lag relative to sinusoidal frequency ..... 70

Figure 4-1. The setup for AP tracking using a linear array (Badreddine et al. 2016)..... 80

Figure 4-2. Example of the Labview software for stimulating and recording. ..... 81

Figure 4-3. Images showing the setup. ..... 83

Figure 4-4. Distribution of light intensity on photodiode array. ..... 84

Figure 4-5. The propagating AP averaged over multiple stimuli (Badreddine et al. 2016). ..... 85

Figure 4-6. Real-time tracking of APs (Badreddine et al. 2016). ..... 86

Figure 4-7. Traces of the XPS for averaged and real-time data (Badreddine et al. 2016).87

Figure 4-8. Traces for the faster stimulus. ..... 88

Figure 4-9. Sample frames from movie of XPS at faster stimulation rate (Badreddine et al. 2016). ..... 89

Figure 5-1. DIC image of axonal projections in hippocampal culture. ..... 94

Figure 5-2. Static optical signal of neuron culture. ..... 95

Figure 5-3. Image of the mouse brain slice and entorhinal-hippocampal area of interest (Canto et al. 2008)..... 97

Figure 5-4. Iterative brain slice chamber designs. ..... 99

Figure 5-5. Temperature controller for aCSF. ..... 100

Figure 5-6. Brain slice positioning of the electrodes and light. ..... 101

Figure 5-7. Electrical recording of the brain slice. ..... 102

Figure 5-8. Birefringence verification for brain slice. ..... 103

Figure 5-9. Songbird trachea segment. ..... 104

Figure 5-10. Smaller nerve chamber. ..... 105

Figure 5-11. Extraction procedure for maximum length of sciatic nerves (Bala et al. 2014). ..... 107

Figure 5-12. Extracted sciatic nerves at maximum length (Bala et al. 2014). ..... 108

Figure 5-13. Birefringence of whole nerve. ..... 110

Figure 5-14. A crooked section of the nerve shows intensity pattern. ..... 111

Figure 5-15. Angle dependence of nerve subset birefringence. ..... 112

Figure 5-16. Birefringence of nodes of Ranvier. ..... 114

Figure 5-17. Depiction of birefringence from myelin sheath and axonal membrane. .... 115

Figure 5-18. Crisscrossing nerve sections canceling-out birefringence. ..... 117

Figure 5-19. Setup for quarter waveplate experiment. ..... 118

Figure 5-20. Verification of birefringence in setup without a quarter waveplate. ..... 119

Figure 5-21. Effect of QWP angle on intensity from sciatic nerve. ..... 121

Figure 5-22. Sciatic nerve XPS in response to applied field. ..... 125

Figure 5-23. Electrical recordings of AP activity at various stimulus amplitudes. ..... 127

Figure 5-24. XPS recording of a sciatic nerve. ..... 128

Figure 6-1. XPS measured in reflection geometry (Yao et al. 2005). ..... 135

# LIST OF ABBREVIATIONS

| | |
|---|---|
| ABS | Acrylonitrile butadiene styrene |
| AP | Action potential |
| DAQ | Data acquisition card |
| EMI | Electromagnetic interference |
| FOV | Field of view |
| IOS | Intrinsic optical signal |
| LED | Light-emitting diode |
| LSI | Linear stimulus isolator |
| NI | National Instruments |
| PG | Pulse generator |
| QWP | Quarter waveplate |
| SLD | Superluminescent diode |
| SNR | Signal-to-noise ratio |
| SR | Sampling rate |
| TTX | Tetrodotoxin |
| VSD | Voltage-sensitive dye |
| XPS | Crossed-polarization signal |

# CHAPTER 1. INTRODUCTION

Fast, noninvasive methods for imaging activity in peripheral nerves and other organized neuronal structures are limited for both research and clinical applications. The development of minimally invasive, high-resolution modalities for imaging neuronal activity, both for research and pre-clinical applications, is an ongoing endeavor that will allow for a greater understanding of neuronal network processes involved in complex functions, as well as neuropathies such as epilepsy, stroke and cortical spreading depressions associated with migraines (Luft et al. 2005; Briggman et al. 2005; Ba et al. 2002; Brázdil et al. 2005). Current methods for monitoring neuronal activity, while informative, have substantial limitations. Microelectrodes provide high temporal resolution, but at the expense of irreversible tissue damage and insufficient spatial resolution due to volume conduction effects and the limited number of electrodes (Csicsvari et al. 2003; Rector et al. 1997). Methods such as functional magnetic resonance imaging (fMRI), and autofluorescence of flavin adenine dinucleotide (FAD) and nicotinamide adenine dinucleotide phosphate (NADP-H), are limited in that they image metabolic activity indirectly associated with neural activity through the measurement of mitochondrial or hemodynamic responses, which present with a delay after neural impulses propagate (Shuttleworth 2010; Logothetis & Pfeuffer 2004). Small-scale imaging methods generally use markers such as voltage sensitive dyes (VSDs) and calcium indicators and can provide a fairly high spatial resolution, but are limited by the dyes' temporal responsivities, and are cytotoxic and thus not suitable for clinical imaging (Grinvald & Hildesheim 2004; Smetters et al. 1999), although recently dyes are

becoming less toxic (Rowland et al. 2015), and genetically encoded voltage indicators have removed some of these barriers for research purposes (Broussard et al. 2014).

Fast intrinsic optical signals (IOS), including changes in intensity, scattering and optical birefringence, have previously been explored as markers to measure neuronal activity directly in single neurons, nerves, and *in vivo* brain tissue, and can potentially be developed with high spatiotemporal resolution to study neural network activity with minimal invasiveness (Cohen et al. 1969; Stepnoski et al. 1991; Carter et al. 2004; Yao et al. 2005). Scattering signals have been studied extensively, both *in vivo* and *ex vivo*; they have been attributed predominantly to cellular swelling and are small (signal-to-background = $\sim 10^{-5}$) and challenging to record (Cohen et al. 1969; Carter et al. 2004). These signals are difficult to measure consistently with an acceptable signal-to-noise ratio (SNR) and are limited in spatial resolution in highly scattering tissue such as the cortex of the brain (Cohen, LB and Keynes et al. 1971; Stepnoski et al. 1991)

Nerves inherently exhibit a static (rest condition) birefringence that is associated with the structural anisotropies of axonal microtubules, myelin sheaths, membrane phospholipids and proteins, as well as surrounding tissues, which include Schwann cells and axon sheaths (Cohen et al. 1970; Ross et al. 1977; Schmitt & Bear 1937; de Campos Vidal et al. 1980) The dynamic birefringence, or "crossed-polarized signal" (XPS), in neurons arises from activity in axons and occurs with a rapid momentary change, typically a decrease, in the birefringence when action potentials (APs) propagate along them (Cohen et al. 1969). The XPS (signal-to-background = $\sim 10^{-4}$) is typically one order of magnitude larger than the scattering signal and has been detected successfully in single

trials in large crustacean nerves (Carter et al. 2004). While transmission geometry (between crossed linear polarizers) is typically used to detect the XPS, it has also been detected using a reflection geometry, demonstrating the possibility of using birefringence to track neuronal activity in cortical tissue *in vivo* (Yao et al. 2005).

Changes in birefringence (or dynamic birefringence) provide an arguably cleaner method of measuring IOS as compared to scattering methods (Cohen et al. 1970; Carter et al. 2004). Despite being studied extensively, the physiological mechanisms underlying the cause of these changes in birefringence in neuronal tissue remain under discussion. Both mechanical (Tasaki & Byrne 1993; Yao et al. 2003) and electrical (Cohen 1973; Landowne 1985; Tasaki et al. 1968) mechanisms have been suggested, but the timing suggests that the signal occurs directly with APs (Cohen et al. 1970). Furthermore, when the timing of the signals from VSDs and intrinsic birefringence were measured simultaneously, it was found that the birefringence signal was directly correlated with, and possibly even preceded, the VSD signal (Foust & Rector 2007). These changes have been reliably demonstrated to occur simultaneously with action potential (AP) propagation over a variety of scales, from single axonal membranes to complex nerve bundles (Cohen et al. 1969; Stepnoski et al. 1991; Carter et al. 2004; Tasaki & Byrne 1992; Badreddine et al. 2015). Changes in birefringence are likely a product of induced polarizability by electric-field fluctuations in the vicinity of axonal membranes that occur directly with AP propagation, providing a cleaner method of measuring these activities as compared to other optical methods (Cohen et al. 1970; Carter et al. 2004; Foust & Rector 2007; Badreddine et al. 2015; Badreddine et al. 2016). Thus, changes in birefringence

provide a means of directly measuring AP propagation in real-time.

For single axons, the XPS was found to predominantly be isolated to areas near or through the membrane; and in nerve bundles, an appreciable contribution to static birefringence from Schwann cells and connective tissue was noted (Cohen et al. 1970). This complexity in optical signals caused by contributions from adjacent tissue structures presents a significant barrier to the full understanding of the underlying physiological origins of the XPS in higher-order neuronal structures. Additional information would lead to a more complete understanding of the causes of the XPS in nerves and brain tissues. The study of these signals would be expedited by an improved setup and SNR. It would also be aided by a method of tracking the signal and studying its evolution in time and distance from the stimulus. Adapting this technology for the goal of imaging activity in myelinated tissues will require a more thorough understanding of the effects that myelination may have on the signal.

The work presented in this dissertation reaches toward the goal of imaging mammalian neuronal activity using AP-induced changes in birefringence. The dissertation is organized into six chapters. Chapter 2 provides a general background necessary to understand this work. It begins by first reviewing birefringence as a concept and then providing an overview of the relevant previous work in the field, including work done by a former student in the Biomedical Optics Lab, Kurt Schoener. Chapters 3 through 5 provide all results and analysis of the work for this dissertation, broken into three aims. Aim 1 in Chapter 3 is split into two parts; in Part 1, improvements done to the setup and to SNR are described in detail, and in Part 2, the experiments performed to

further understand the XPS are provided. In Chapter 4, a new setup used to track 'real-time' changes in birefringence is described. Chapter 5 provides new work to study the effects of myelination of the XPS and to image AP activity in mouse sciatic nerves, the first detection of its kind. Chapter 6 provides the conclusions and future directions for this work.

# CHAPTER 2. BACKGROUND

## 2.1. Introduction

The development of minimally invasive, high-resolution modalities for imaging neuronal activity, both for research and pre-clinical applications, is an ongoing endeavor that will allow for a greater understanding of neuronal network processes involved in complex functions, as well as neuropathies such as epilepsy, stroke and cortical spreading depressions associated with migraines (Luft et al. 2005; Briggman et al. 2005; Ba et al. 2002; Brázdil et al. 2005). Current methods for monitoring neuronal activity, while informative, have substantial limitations. Microelectrodes provide high temporal resolution, but at the expense of irreversible tissue damage. They also have insufficient spatial resolution due to volume conduction effects and the limited number of electrodes (Csicsvari et al. 2003). Methods such as functional magnetic resonance imaging (fMRI), and autofluorescence of flavin adenine dinucleotide (FAD) and nicotinamide adenine dinucleotide phosphate (NADP-H), are limited in that they image metabolic activity indirectly associated with neural activity through the measurement of mitochondrial or hemodynamic responses, which present with a delay after neural impulses propagate (Shuttleworth 2010; Logothetis & Pfeuffer 2004). Voltage sensitive dyes (VSDs) and calcium indicators can provide a fairly high spatial resolution, but are limited by the dyes' temporal responsivities, and are cytotoxic and thus not suitable for clinical imaging (Grinvald & Hildesheim 2004; Smetters et al. 1999).

Fast intrinsic optical signals (IOS), including changes in intensity, scattering and optical birefringence, have previously been explored as markers to measure neuronal

activity directly in single neurons, nerves, and *in vivo* brain tissue, and can potentially be developed with high spatiotemporal resolution to study neural network activity with minimal invasiveness (Cohen et al. 1969; Stepnoski et al. 1991; Carter et al. 2004; Yao et al. 2005). Scattering signals have been studied extensively, both *in vivo* and *ex vivo*; they have been attributed predominantly to cellular swelling and are small (signal-to-background = $\sim 10^{-5}$) and challenging to record (Cohen et al. 1969; Carter et al. 2004). These signals are difficult to measure consistently with an acceptable signal-to-noise ratio (SNR) and are limited in spatial resolution in highly scattering tissue such as the cortex of the brain (Cohen, LB and Keynes et al. 1971; Stepnoski et al. 1991)

Changes in birefringence (or dynamic birefringence) provide an arguably cleaner method of measuring IOS as compared to scattering methods (Cohen et al. 1970; Carter et al. 2004). Nerves inherently exhibit a static (rest condition) birefringence that is associated with the structural anisotropies of axonal protein filaments, membrane phospholipids and proteins, as well as surrounding tissues, which include Schwann cells and axon sheaths (Cohen et al. 1970; Ross et al. 1977) The dynamic birefringence, or "crossed-polarized signal" (XPS), in neurons arises from activity in axons and occurs with a rapid momentary change, typically a decrease, in the birefringence when action potentials (APs) propagate along them(Cohen et al. 1969).

A more in-depth exploration of these background materials is presented in the following sections in this chapter. First, section 2.2 provides a review of light polarization and uniaxial birefringence, insofar as those subjects pertain to this thesis. Then, in section 2.3, the relevant morphology of the specimen used in these studies is described. Section

2.4 presents an overview of the nature of 'static' birefringence intrinsic to nervous systems of significance here, and section 2.5 describes the change in birefringence associated with action potential propagation. Finally, a summary of the relevant studies performed by various research groups to analyze the nature of the birefringence signals is provided in section 2.6. This background aims to provide the reader with a focused understanding of the most relevant features of this field of research with regards to this dissertation.

## 2.2. Light polarization and birefringence

### *2.2.1. Light polarization and the electric field*

Light is composed of photons which have oscillating electric and magnetic fields orthogonal both to one another and to the direction of propagation of the photons. The photons of light along one direction of propagation exhibit a combination of their electric fields. The time and position of the overall electric field of propagating light's wavefront defines its polarization. If the electric field of the wavefront is completely out of phase, the light is said to be randomly polarized. When the electric field of the wavefront oscillates along one axis, it's said to be linearly polarized, as depicted in Figure 2-1 on the left. In that case, the projected x and y components of the electric field (assuming direction of propagation z) of the wavefront are exactly in phase, or exactly 180° out of phase. Circular polarization occurs when the electric field components are exactly 90° out of phase, creating a rotation of the electric field in time that, when projected onto the x-y plane, takes the form of a circle. Elliptical polarization happens when the electric field

components are at some oblique angle out of phase. Circular polarization can be thought of as a special condition of elliptical polarization.

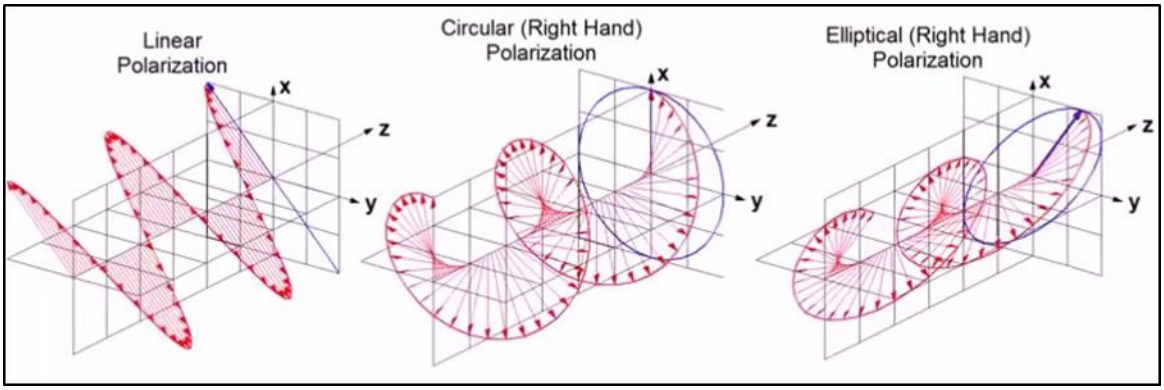


Figure 2-1. Depiction of light polarization.

*Left:* Linearly polarized light, or light whose electric field components are in phase (or exactly 180° out of phase). *Middle:* Circularly polarized light, or light whose electric field components are exactly 90° out of phase. *Right:* Elliptically polarized light where the electric field components are somewhere in between. Image extracted from https://www.youtube.com/watch?v=Q0qrU4nprB0.

### *2.2.2. Uniaxial Birefringence*

Birefringence is a rotation of the electric field of light resulting from structural or electrical anisotropies in a medium. In the case of uniaxial birefringence (for simplicity in this thesis we consider only this condition), the axis of anisotropy is called the optic axis. The electric field of light oscillating along that axis experiences an index of refraction, the extraordinary index of refraction ($n_e$), that is different than that experienced at other angles. The electric field components orthogonal to the optic axis follow the ordinary index of refraction, $n_o$. When unpolarized light propagates at an oblique angle to the optic axis, upon entering the medium, it splits into two wavefronts, the extraordinary and the ordinary, as depicted in Figure 2-2A.

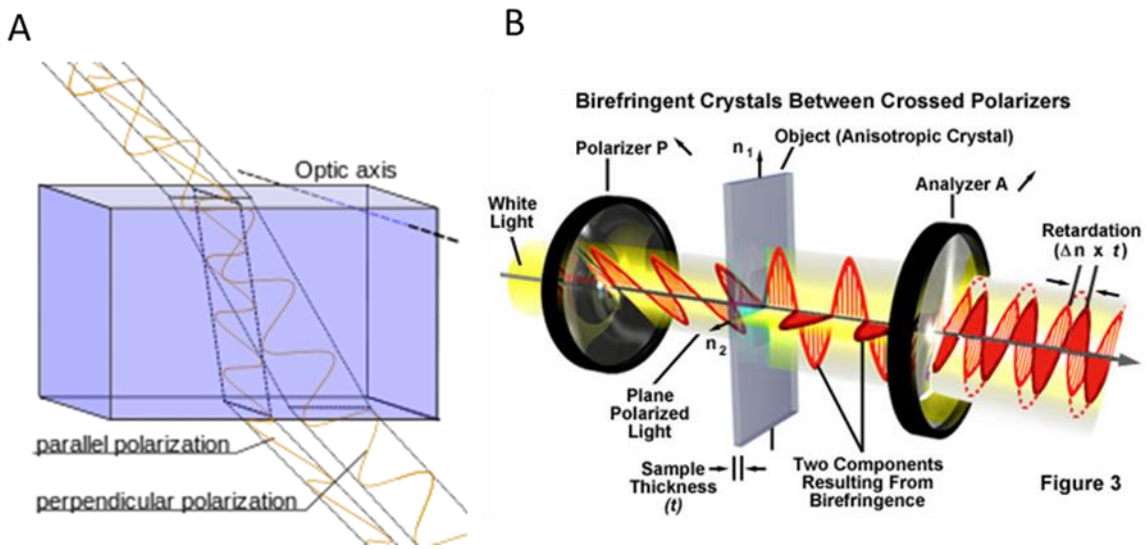


Figure 2-2. Depictions of birefringence.

A) Unpolarized light entering a birefringence material at an oblique angle to the optic axis is split into the extraordinary and ordinary wavefronts, exiting the material at different points. Image taken from https://en.wikipedia.org/wiki/Birefringence#/media/File:Positively_birefringent_material.svg. B) When linearly polarized light propagates through a birefringent material perpendicular to the optic axis then the differences in the indices of refraction present as a phase shift in the electric field components, which can be detected when sent through a crossed polarizer. Image taken from https://micro.magnet.fsu.edu/optics/lightandcolor/birefringence.html.

When a birefringent material is placed between a pair of crossed linear polarizers, linearly polarized light incident to the material undergoes a rotation due to a shift in the phases of the two electric field components, causing the light to be elliptically polarized, allowing a portion of the light to pass through the analyzer, as shown in Figure 2-2B. Figure 2-3 shows this in our setup, with a birefringent piece of twisted tape placed between the polarizer pair. Without the material, most of the light is absorbed by the analyzer.

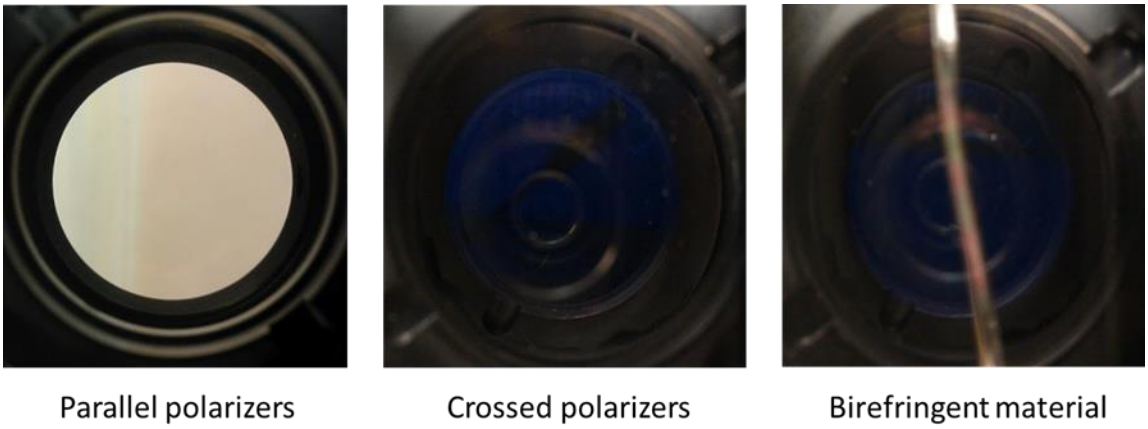


Figure 2-3. Birefringent example from our setup.

When linear polarizers are parallel, 50% of the light passes through, but when the polarizers are crossed, most of the light is blocked. A birefringent piece of tape between the polarizers allows light to pass through.

## 2.3. Experimental specimen tissue structures

### *2.3.1. Unmyelinated peripheral nerves*

#### 2.3.1.1. Lobster walking leg nerve

Aims 1 and 2 of this thesis focus on data collected from the four rostral-most walking leg nerves (WLN) of lobsters, *Homarus americanus*. An example of a WLN is shown in Figure 2-4. The WLN is easily extracted using Furusawa's pullout method (Furusawa 1929), and its ends are ligated. The WLN is an unmyelinated nerve composed of three groups of axon diameters: the giant axons (50–100 $\mu$m), medium axons (20–30 $\mu$m), and the small axons (0.1–5 $\mu$m) (Darin De Lorenzo et al. 1968), as shown in cross sections in Figure 2-5. This heterogeneous distribution of axon sizes results in a large range of conduction velocities (Hodgkin 1954). Many axons are embedded in sheaths such as Schwann cells, and others are grouped into a bundle that is sheathed by

connective tissues (Darin De Lorenzo et al. 1968). Additionally, the whole nerve trunk has a connective tissue sheath around its entirety. The structure of the nerve is maintained by a combination of cytoskeletal proteins such as microtubules and extracellular collagen.


Figure 2-4. Furusawa's pullout method for lobster walking leg nerve (Wininger et al. 2009).

This is an image showing the lobster's walking leg nerve after extraction using Furusawa's pullout method.

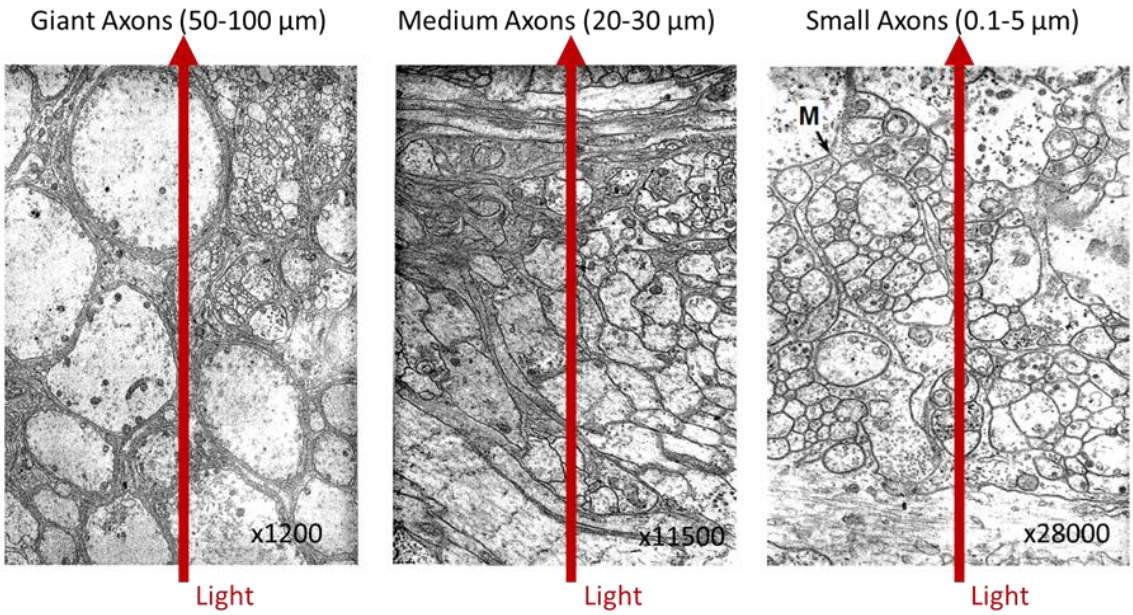


Figure 2-5. Cross sections of the lobster walking leg nerve (Darin De Lorenzo et al. 1968).

The lobster walking leg nerve has a heterogeneous distribution of axon diameters in three

size groups, the giant, medium and small, and thus has a broad range of conduction velocities.

2.3.1.2. Horseshoe crab lateral optic nerve

The lateral optic nerve (LON) of the horseshoe crab, *Limulus polyphemus*, extends through the optic tract, where >1500 eccentric axons may be present, with diameters varying within a narrow range (~10–20 μm), and without other axon types (Battelle 2006; Fahrenbach 1975). The section of the LONs of concern here extends from the end organ to the end of the optic tract. The homogeneous nature of the size range of eccentric axons in this section leads to a narrow distribution of conduction velocities. A cross section of the LON is shown in Figure 2-6.

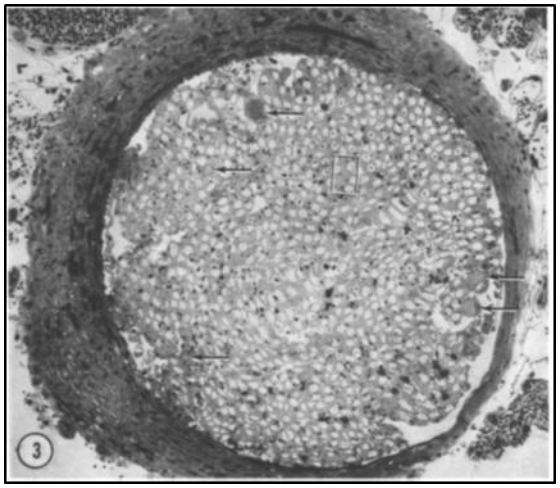


Figure 2-6. Horseshoe crab lateral optic nerve cross section (Fahrenbach 1971).
A cross section of the LON shows a homogeneous range of axon sizes resulting in a narrow distribution of conduction velocities.

*2.3.2. Myelinated peripheral nerves*

Myelination in peripheral axons presents as a series of sheaths wrapping around the axon, formed by Schwann cells, as shown in Figure 2-7. These sheaths are composed

of several overlapping layers of phospholipid bilayers which restrict the movement of ions across the membrane and are held together by filamentous proteins. By increasing membrane resistance, myelin speeds up the conduction velocity. Repeated nodes of Ranvier, or openings in the myelin, allow the signal to be retriggered.

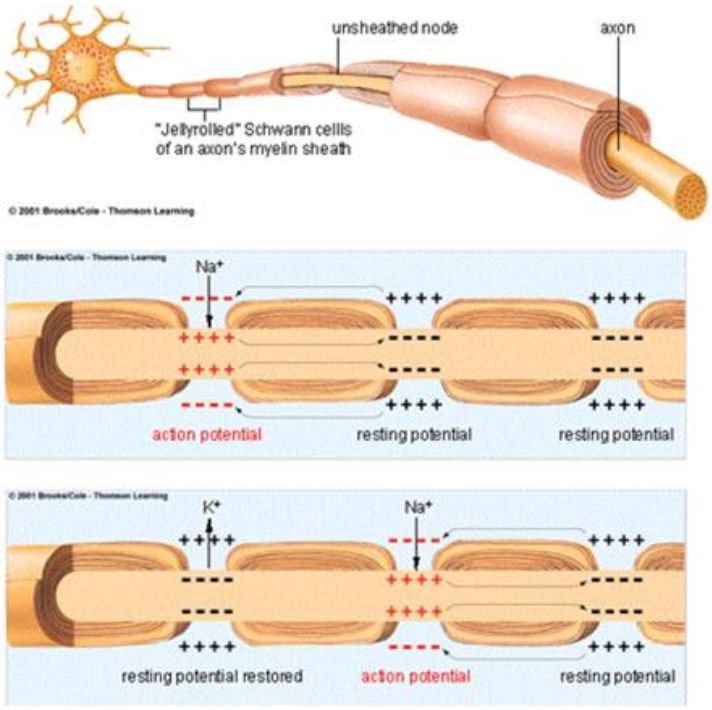


Figure 2-7. Myelination.

In peripheral nerve axons, myelin acts as an electrical insulator and is formed by a series of Schwann cells which are wrapped in a spiral around the axon. Action potentials are retriggered at the nodes of Ranvier, or openings in the myelin sheath. Image from http://www231.pair.com/fzwester/courses/bis10v/week10/12circuits.html.

2.3.2.1. Songbird laryngeal nerve

The distribution of axon diameters of the laryngeal nerve spans <1 $\mu$m up to around 10 $\mu$m, skewed to the smaller diameter axons (da Silva et al. 2016). An image

showing the laryngeal nerve of a rat is provided in Figure 2-8. The axons are all myelinated and the AP velocity is at least 10 mm/ms.

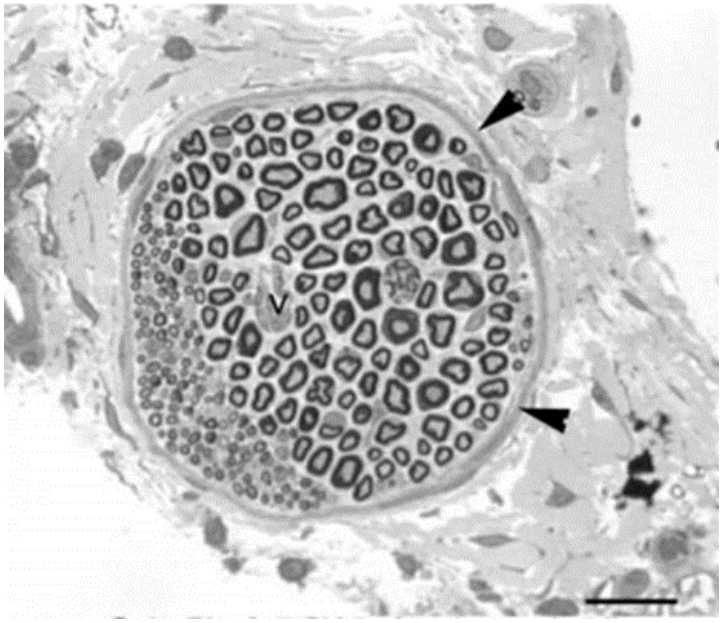


Figure 2-8. Laryngeal nerve (da Silva et al. 2016).
A rat laryngeal nerve cross section is shown, but the songbird nerve is similar. The distribution of axon sizes in the laryngeal nerve span the range of < 1 $\mu$m up to around 10 $\mu$m, with the majority being on the smaller side. The heavy degree of myelination results in signals which propagate at a minimum velocity of 10 mm/ms.

2.3.2.2. Mouse sciatic nerve

The sciatic nerve axons vary in diameter from < 1 to 20 $\mu$m, with the mode around 4 $\mu$m (Assaf et al. 2008), and this translates to conduction velocities of 0.2 to 150 mm/ms. A cross section of this nerve is shown in Figure 2-9. The axons are divided into types. Type A fibers have the largest diameters and thicker myelin sheaths with conduction velocities from about 30 to 150 mm/ms. Type B fibers have less pronounced myelin sheaths, so their conduction velocities range from 3 to 15 mm/ms. The smallest

diameter fibers, type C fibers, do not have myelin sheaths and so have the lowest conduction velocities (< 2 mm/ms).

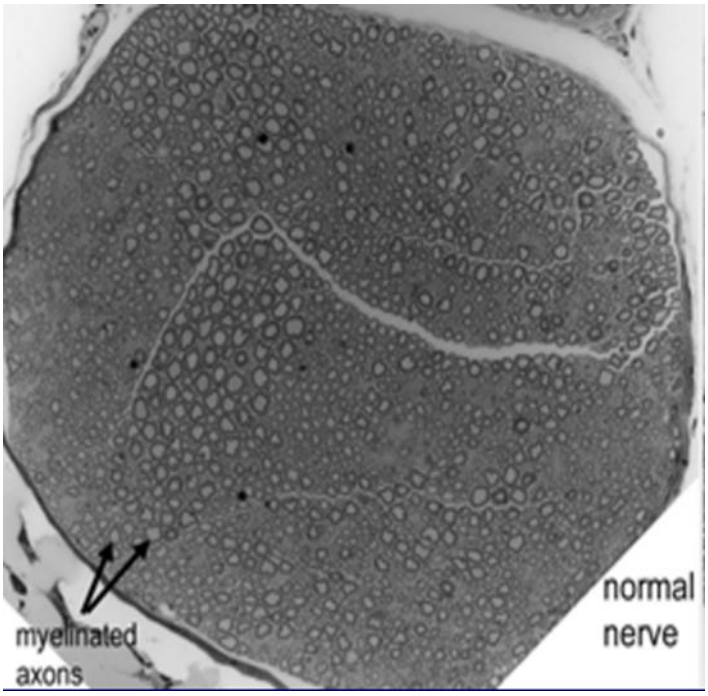


Figure 2-9. Mouse sciatic nerve cross section.

The large range of axon diameters in the sciatic nerve is apparent in this image, with a large proportion of the axons being myelinated and some being smaller and unmyelinated. Image taken from http://orion.umdnj.edu/NM-PROJECT-2012.html.

## 2.4. 'Static' birefringence in nervous tissue

### *2.4.1. Birefringence of the axon/nerve*

The structural anisotropy of nerves results in an intrinsic birefringence, called 'static' birefringence in this work to indicate that it is independent of action potential activity. Each axon can be approximated as a long cylinder with cytoskeletal components oriented along the longitudinal axis (and other orientations) and a phospholipid bilayer with membrane proteins and lipid molecules oriented radially (Schmitt & Bear 1937).

The cellular membrane electric fields established by ion gradients also are thought to contribute directly to the birefringence (Cohen et al. 1970; Badreddine et al. 2015). This structural arrangement has an optic axis oriented either radially or along the axon (Chinn & Schmitt 1937; Cohen et al. 1970). To maximize measurement of birefringence, a linear polarizer must filter light to 45° relative to the optic axis, in the manner depicted in Figure 2-10. At this angle, linearly polarized light experiences a maximum rotation through the tissue, producing varying degrees of elliptically polarized light, dependent on spatial location. A depiction of the simplest setup used to detect birefringence is shown in Figure 2-11.

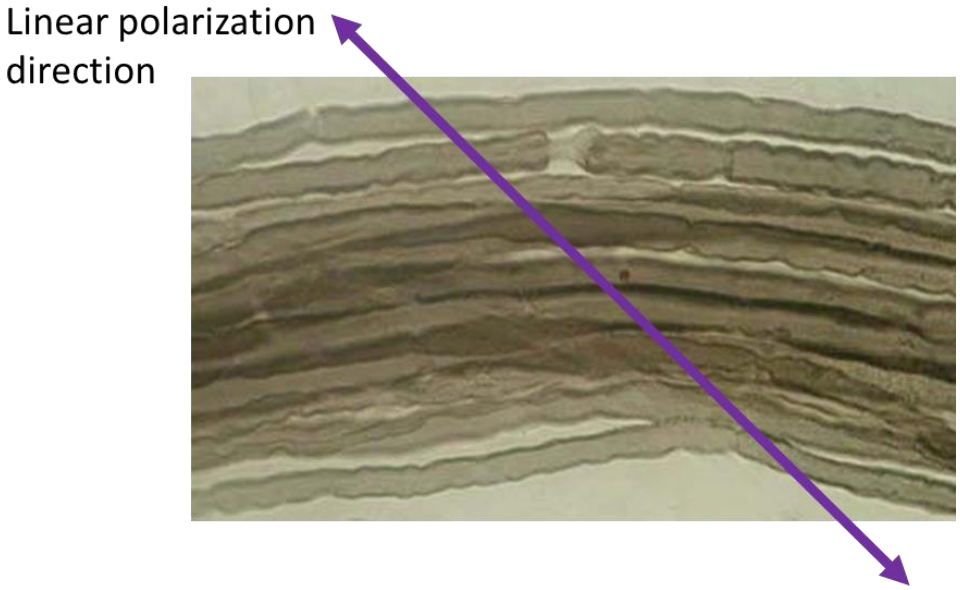


Figure 2-10. Direction of polarization to maximize birefringence signal.

An image of a nerve bundle with a representation of light polarized at 45° to the long axis of the nerve to maximize the measurement of birefringence. Image taken from http://www.histol.ru/atlas-en/nerv-01-en.htm.

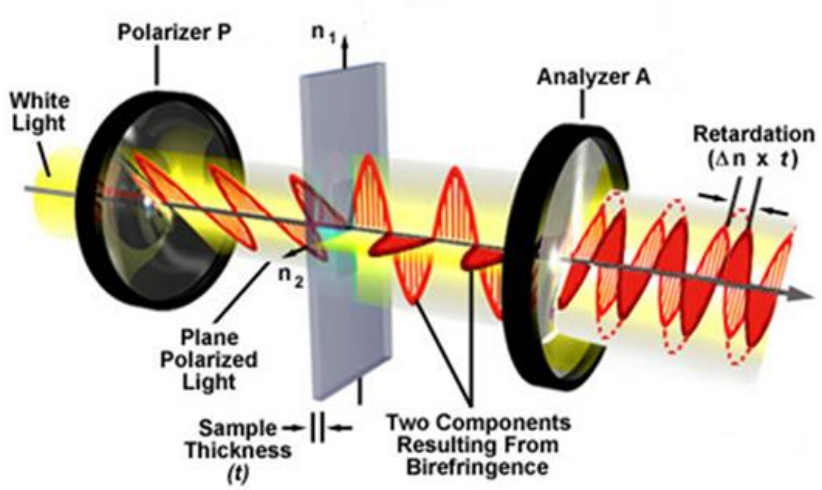


Figure 2-11. Simplest setup for detecting birefringence.

This is a depiction of the simplest arrangement of optics possible to detect birefringence. A pair of crossed linear polarizers are used, with the incident polarizer axis set to 45°. Image taken from https://micro.magnet.fsu.edu/optics/lightandcolor/birefringence.html.

### *2.4.2. Myelination and birefringence*

Intrinsic static birefringence of myelin has been revealed to occur predominately at the periphery of axons in nerves (de Campos Vidal et al. 1980), as shown in Figure 2-12. The myelin was found to have negative form birefringence (relative to long axis), resulting from the array of lipids in the myelin sheath, occurring alongside the positive birefringence displayed by other axonal structures, specifically the network of protein filaments, such as those involved in the cytoskeleton. A newer study revealed these features more clearly, and also demonstrated the birefringence of the nerve bundle's collagen organization within and surrounding the tissue (Figure 2-13) (Maturana et al. 2013).

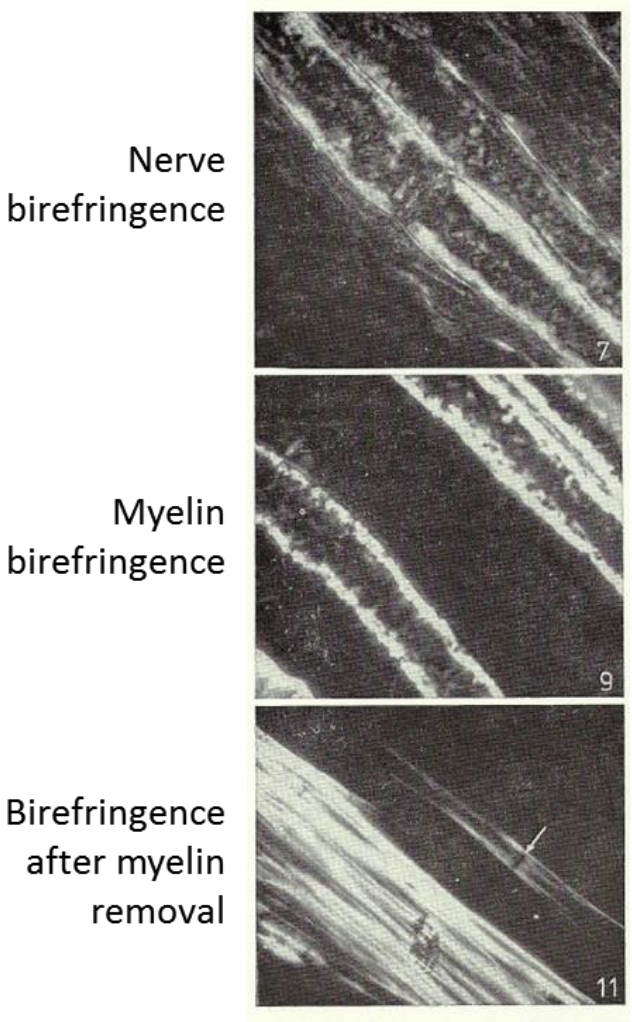


Figure 2-12. Birefringence of myelinated nerve (de Campos Vidal et al. 1980).

The top image shows whole nerve birefringence, zoomed into a few axons. The middle image shows birefringence of just the myelin sheaths, showing most of the signal originating near the periphery. The bottom image shows birefringence from the protein filament network after removing the myelin lipids.

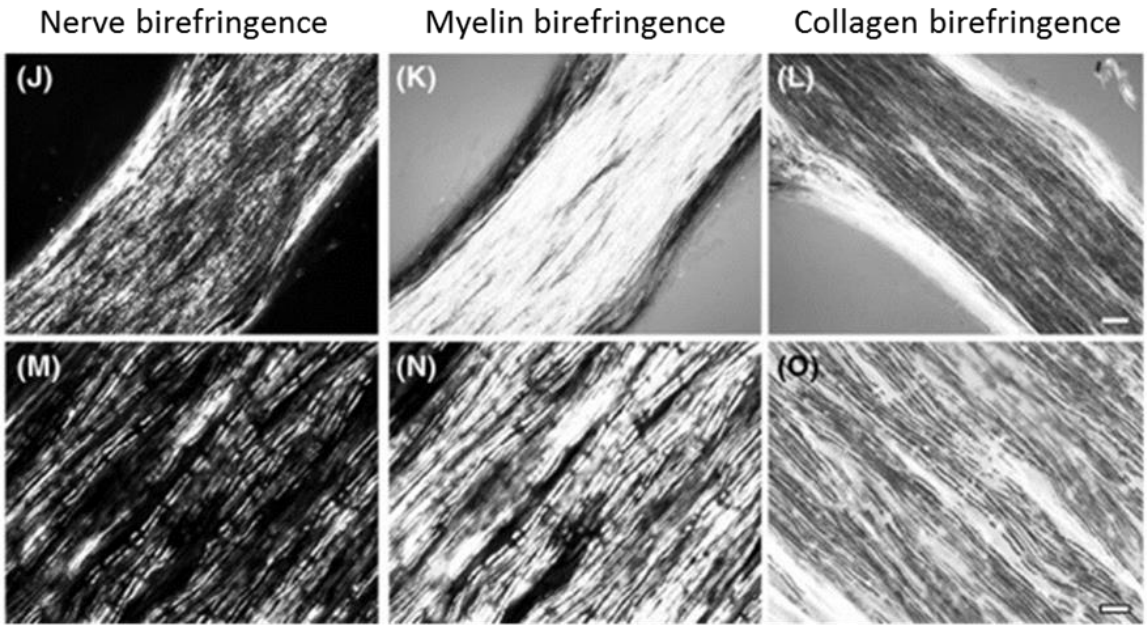


Figure 2-13. Sciatic nerve myelin and collagen birefringence in treated nerves (Maturana et al. 2013).

Images here show the birefringence of the myelin sheath in collagen-enhanced, treated nerves. The extensive collage network around the nerve and within it, is shown to have a contrasting birefringence to that of the myelin.

### *2.4.3. Mouse brain slices*

Brain slices contain many areas of high degrees of anisotropy which could be utilized to image birefringence of axons. One such area is the Schaffer collaterals pathway, which leads from the dentate gyrus (DG) through the CA3 neurons and from there downstream to the CA1 pyramidal neurons, as shown in Figure 2-14. This pathway can be represented as a group of parallel-oriented fiber tracts, the overall anisotropy of which may yield a birefringence signal. If neurons in the DG are indiscriminately stimulated electrically, APs may be picked up downstream, and the birefringence signal

can be detected in the pathway between the CA3 and CA1 neurons. The best slice for this would be a sagittal slice, which divides the brain into left and right.

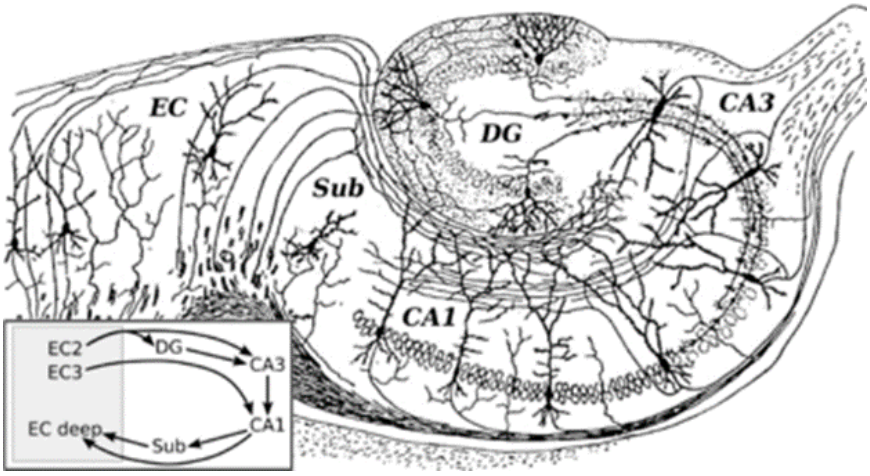


Figure 2-14. Schaffer collaterals of mouse brain slice.

The Schaffer collaterals pathway leads from the dentate gyrus through the CA3 neurons to the CA1 pyramidal neurons. The pathway contains white matter, or myelinated axon tracts, which can be used to image birefringence. Image from https://en.wikipedia.org/wiki/Hippocampus_anatomy#/media/File:CajalHippocampus_(modified).png.

## 2.5. The 'dynamic' birefringence signal in unmyelinated nerves

### *2.5.1. Action potentials (APs) and electric field changes*

Action potentials are the method by which signals are conducted through an axon. They occur as a threshholded, rapid depolarization and repolarization of the transmembrane voltage over just a few milliseconds, which is mediated by voltage-gated ion channels (Figure 2-15). When a depolarizing stimulus reaches an axon, if the membrane voltage reaches the threshold, $Na^+$ channels open, causing a rapid depolarization, which induces $K^+$ channels to open, repolarizing the membrane rapidly.

The change in electric field across the membrane is quite high. For a resting membrane voltage of around -70 mV, and a depolarization to around +30 mV, that is a change of 100 mV. Since the membrane is only around 5 nm thick, this translates to a change in the electric field of around 2 x $10^5$ V/cm, which is considerably high, and includes a polarity reversal. Therefore, it is reasonable to assume that a traveling AP can be detected optically.

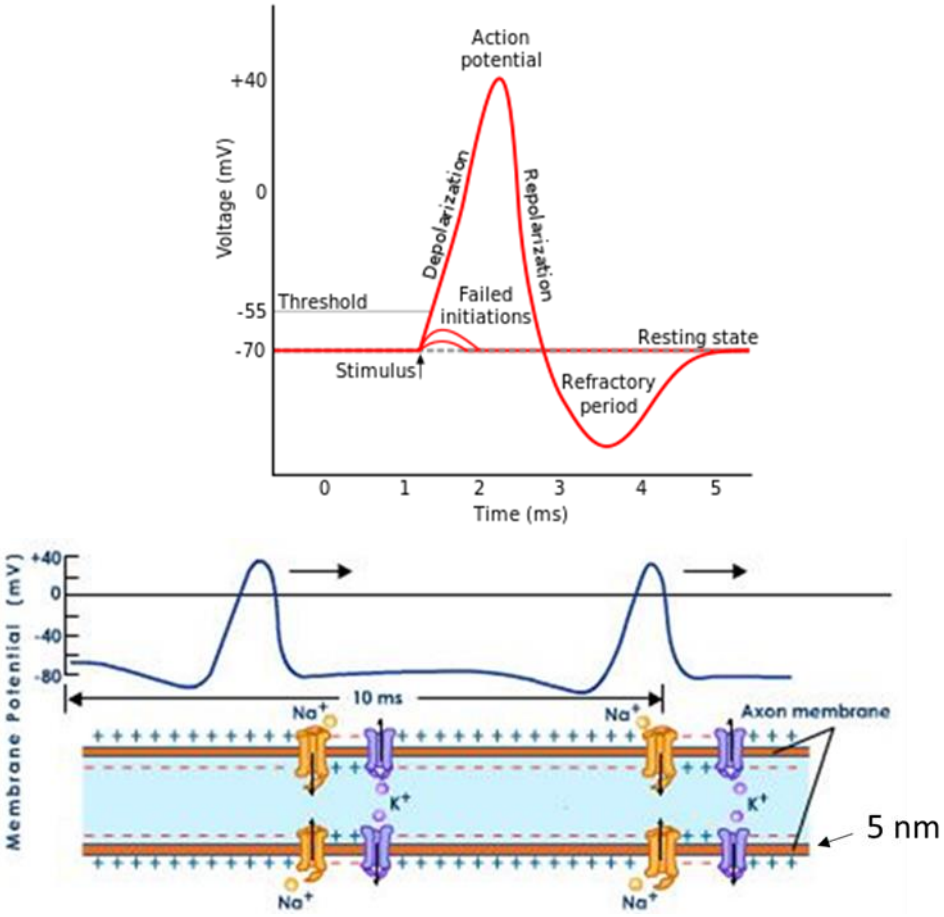


Figure 2-15. Depiction of action potential.

*Top:* Action potentials (APs) are threshholded and result when the membrane is depolarized, resulting in a rapid depolarization then repolarization mediated by voltage-gated ion channels. Image from https://en.wikipedia.org/wiki/Action_potential#/media/File:Action_potential.svg. *Bottom:*

An AP is caused by a depolarization of the membrane reaching a threshold, opening the $Na^+$ channels, followed by a repolarization from the opening of $K^+$ channels. The AP travels from the downstream depolarization due to ion flow. Image taken from http://www.tutorvista.com/content/biology/biology-iv/nervous-coordination/transmission-messages.php.

### *2.5.2. Lawrence Cohen's work on squid giant axons and crab leg nerves*

Changes in birefringence were first detected in squid giant axons in 1968 (Cohen et al. 1968). Using a high number of averages of repeated stimuli, it was found that the birefringence signal (shown in Figure 2-16) lasts only around 2 ms, which closely imitates the timecourse of the action potential. This was the first strong indication that changes in birefringence seem to be directly correlated to AP activity. Later work by the same group demonstrated the signal could be reliably detected in crab nerve bundles (Cohen et al. 1970).

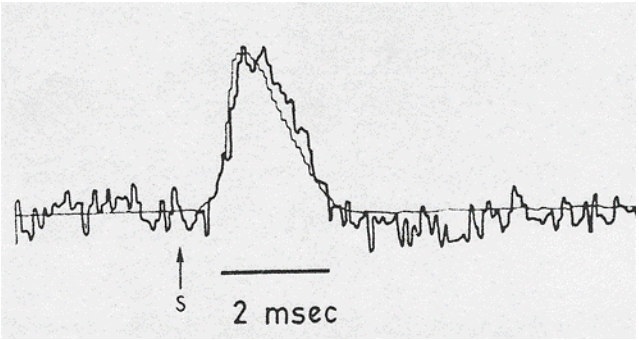


Figure 2-16. The first reported change in birefringence from action potentials (Cohen et al. 1968).

Shown is the timecourse for a squid giant axon, of the change in birefringence from the average of repeated propagating action potentials. The timing closely matches the timing of an action potential.

## 2.6. Exploring the origins and characteristics of the birefringence signals in unmyelinated nerves

### *2.6.1. Lawrence Cohen and squid giant axons*

#### 2.6.1.1. Birefringence vs. scattering

Distinguishing the origins of the signal first requires verifying that what is seen is indeed birefringence, rather than another optical signal, such as scattering or linear dichroism. It is possible that randomly polarized light scattered by the tissue is detected through the crossed polarizers as opposed to birefringence. If birefringence dominates, then the polarization state is simply altered due to a phase shift between the extraordinary and ordinary wavefronts. The intensity of light detected through a pair of crossed polarizers would exhibit a dependence on the angle of the birefringent medium (Cohen et al. 1970). It was found that this was indeed the case, as shown in Figure 2-17. The birefringence signal is a maximum at 45°, as mentioned previously, and is a minimum when the linear polarizers are oriented parallel or perpendicular to the axon's optic axis.

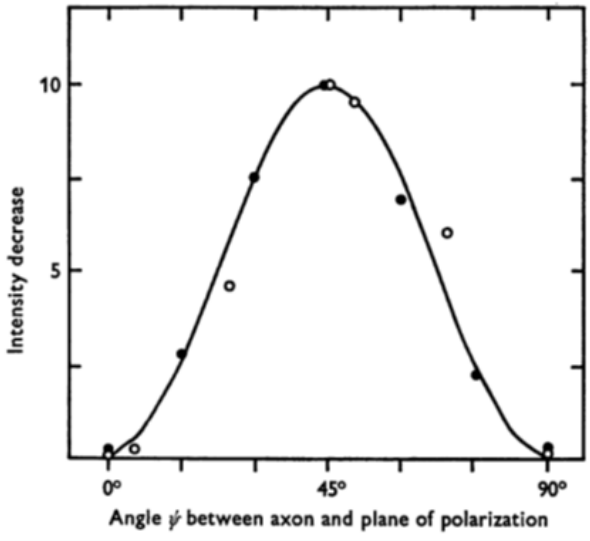


Figure 2-17. Demonstration of birefringence over other optical signals (Cohen et al. 1970).

This curve demonstrates that birefringence dominates when using crossed polarizers, since the signal is a maximum at 45°, and a minimum at 0° and 90°.

2.6.1.2. Location of the birefringence changes

To determine the location of the origin of changes in birefringence in an axon, small strips were used to image a portion of the axon from the left edge to the right edge. The data presented in Figure 2-18 are changes relative to the baseline at that location. It was found that the signal originates near the edges, or near the membrane, as might be expected from action potential propagation.

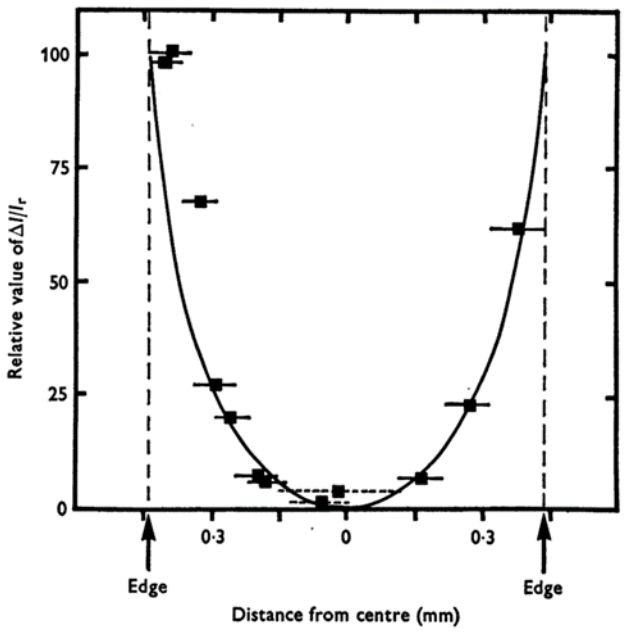


Figure 2-18. Location of the changes in birefringence in an axon (Cohen et al. 1970). The change in birefringence relative to the baseline was measured from the left edge to the right edge of a squid giant axon and the signal was found to originate near the membranes.

2.6.1.3. Voltage-clamping and Kerr effect

Voltage-clamping the squid giant axon was thought to possibly yield insightful information into the origins of the birefringence signal. It can indicate the range of possible membrane voltages and any relationship that may exist between the birefringence and the applied fields, or an electro-optic effect. The nature of an electro-optic effect can give clues as to what type of molecular structures are involved. Cohen et al. (Cohen et al. 1970) determined that the axon responds rapidly to the applied voltage (left in Figure 2-19), both in onset and recovery, and that the birefringence of the axon follows a quadratic relationship (Kerr effect, or quadratic electro-optic effect) with membrane voltage (right in Figure 2-19) in the range of -200 mV to approximately 225

mV, presumably saturating beyond that range. This implies that the signal originating in the membrane has inversion symmetry, but the structures involved remained unknown. It was inferred that a reorientation of membrane dipoles may be responsible for the signal.

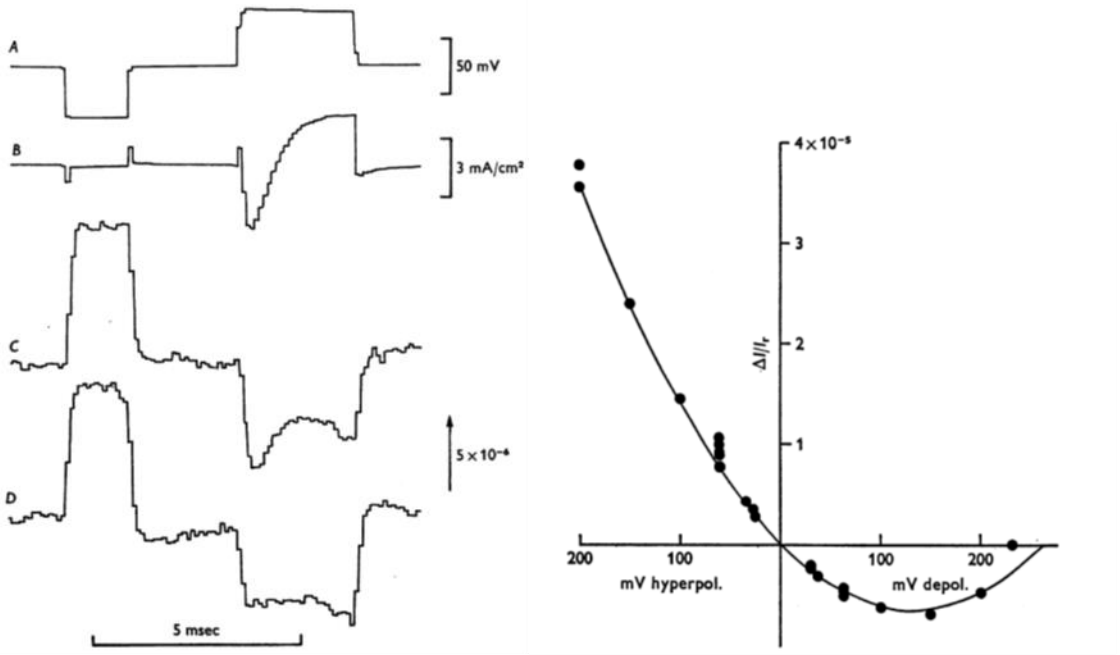


Figure 2-19. Voltage-clamped squid giant axon shows Kerr effect (Cohen et al. 1970). The membrane of a squid giant axon was voltage-clamped at a range of voltages, showing a rapid onset and recovery response time, and a quadratic relationship with the applied voltage magnitude, over both positive and negative polarities.

2.6.1.4. Comparison to light scattering

Forward scattering and right angle scattering from the nerve was measured and compared to the forward transmission birefringence measurements. The time constants of the two signals were found to be similar, but the response to tetrodotoxin (TTX) was found to be different, which suggests a different origin for the signals.

### *2.6.2. Ichiji Tasaki*

By measuring the reflectance of light from a mirror placed on the surface of a nerve bundle, swelling of the nerve was demonstrated during a propagating AP (Iwasa et al. 1980). A comparison of the birefringence and scattering signals in the garfish olfactory nerve to the swelling timecourse suggested that swelling of the superficial layers of the axons is responsible for both optical signals. This behavior was later further explored by another group with optical lever measurements on the lobster nerve bundle (Yao et al. 2003).

### *2.6.3. David Landowne*

It was suggested that the birefringence changes in squid giant axons appear to follow the integral of the gating current of membrane ions and that the cause for the signal is a reorientation of membrane protein channel peptide bonds (Landowne 1993).

### *2.6.4. David Rector*

#### 2.6.4.1. Simultaneous scattering and birefringence measurements

A setup was used to allow for simultaneous measurements of birefringence and right-angle scattering (Carter et al. 2004). They found that the birefringence signal was faster and agreed with previous work (Cohen & Haven 1973) that it be closely related to a change in membrane potential, but that it may be confounded by structural changes such as axonal swelling and phospholipid reorientation (Carter et al. 2004).

#### 2.6.4.2. Chamber design and delayed arrival of peaks

A nerve chamber was designed (shown in Figure 2-20) with a slit aperture to

allow light through at a variety of distances, facilitating a comparison of the compound birefringence peak as a function of distance and time (Carter et al. 2004). The timecourse peaks as measured 3 mm apart were compared, revealing that different portions of the peak are delayed by different amounts, due to grouped AP velocities. This indicates that the signal is sensitive enough to detect axon components contributing to the compound signal, while demonstrating some of the important features of the timecourse, such as a fast onset and a slow recovery.

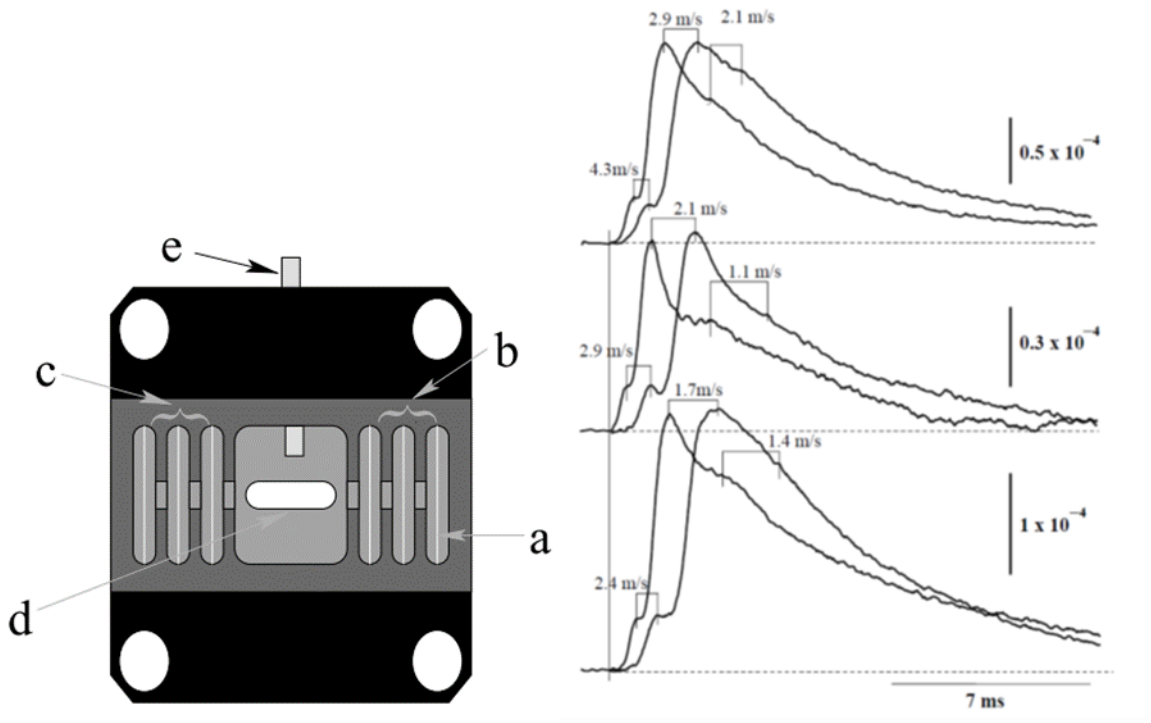


Figure 2-20. A depiction of the windowed chamber and birefringence timecourses (Carter et al. 2004).

*Left:* The nerve chamber with a slit aperture to enable a study of the birefringence peak evolution. *Right:* Data taken 3 mm apart indicating a different amount of delay with different portions of the peak timecourse.

2.6.4.3. Single trial detection

With improved optics and electronics, namely the use of a low-noise photodiode, the birefringence signal was detected in a single-pass trial for the first time with good signal-to-noise, shown in Figure 2-21 (Carter et al. 2004).

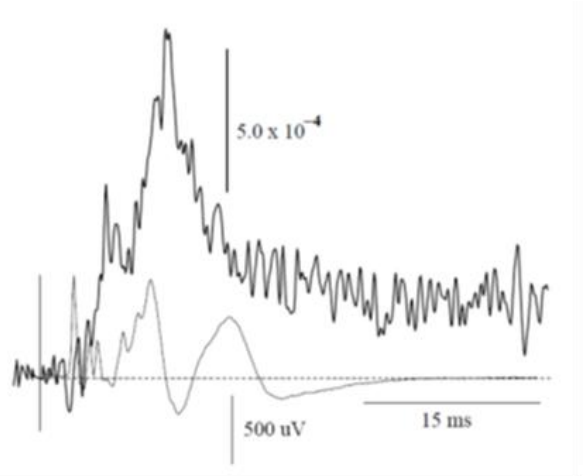


Figure 2-21. Single-pass trial of changes in birefringence (Carter et al. 2004).
This is the first recorded single-pass trial of changes in birefringence with good signal-to-noise.

2.6.4.4. Birefringence directly correlated to AP

The birefringence signal was compared to the signal from 90° scattering, and the signal from a voltage-sensitive dye (VSD), as shown in Figure 2-22 (Foust & Rector 2007). The birefringence signal was found to be more closely related to (and even preceded) the VSD signal, verifying that it is a membrane potential phenomenon. Furthermore, using TTX, ouabain and other neurochemical substances, it was found that the birefringence signal followed the changes to membrane potential that were induced by the drugs. The authors concluded that changes in birefringence must be caused by “a

combination of modifications in the membrane dielectric and changes in membrane protein conformation states."

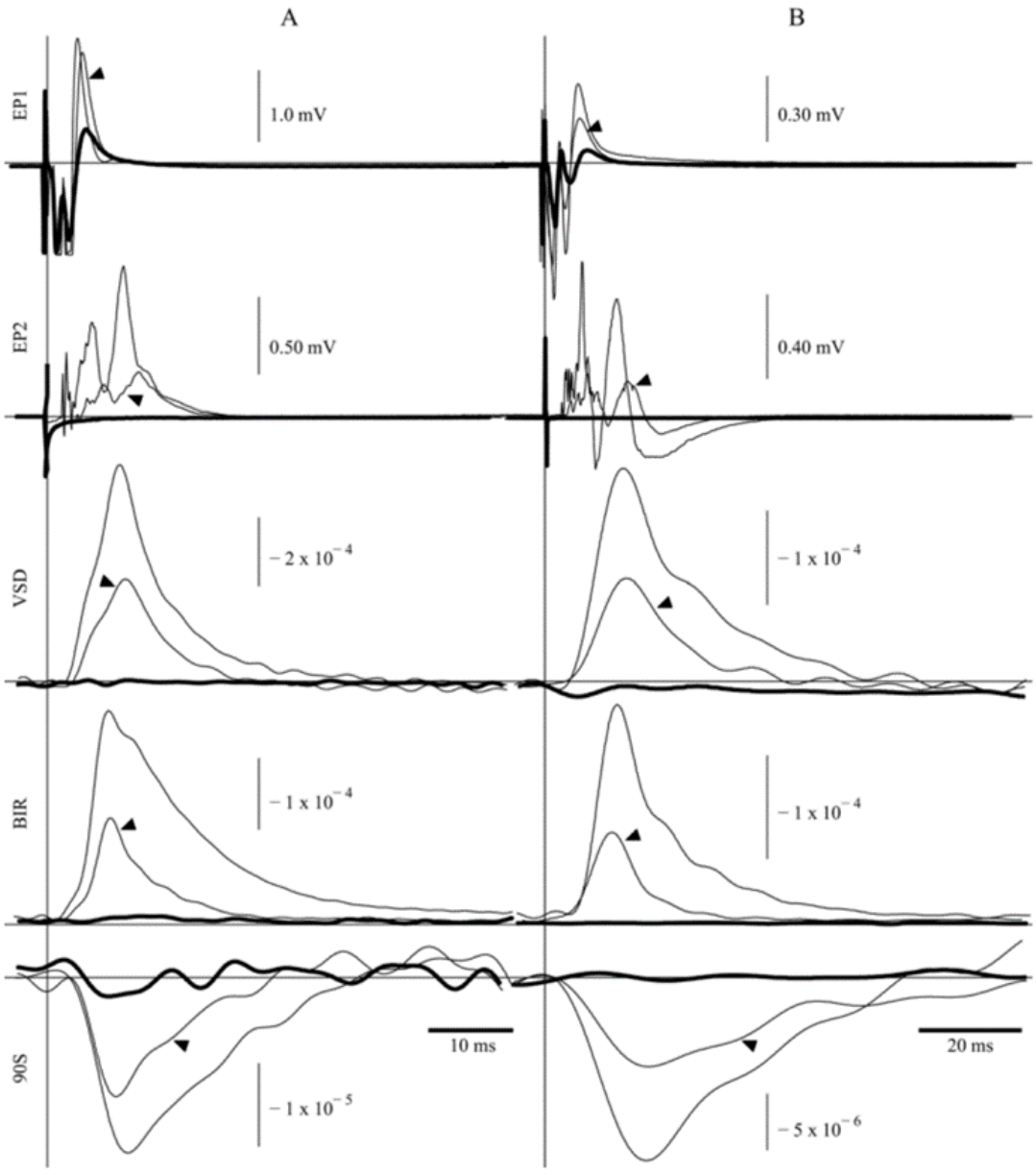


Figure 2-22. Comparison of VSD, BIR and 90S signals (Foust et al. 2008).

The signals measured from VSDs, birefringence and scattering are shown for the addition of TTX before and after. VSD and BIR signals precede the scattering signal, and the BIR peak leads all signals.

### *2.6.5. Our lab (Kurt Schoener) (Schoener 2010)*

#### 2.6.5.1. Custom nerve chamber design

A new nerve chamber was designed that allowed for detecting changes in birefringence anywhere along the length of an excised lobster WLN, including at the sites of electrical stimulation and recording, as shown in Figure 2-23. 99% silver electrodes were used for electrical activity, which was coupled to the nerve through Ringer's solution. This provided a more consistent method to facilitate comparison across nerve samples, and enabled a more thorough investigation of the nature of the XPS.

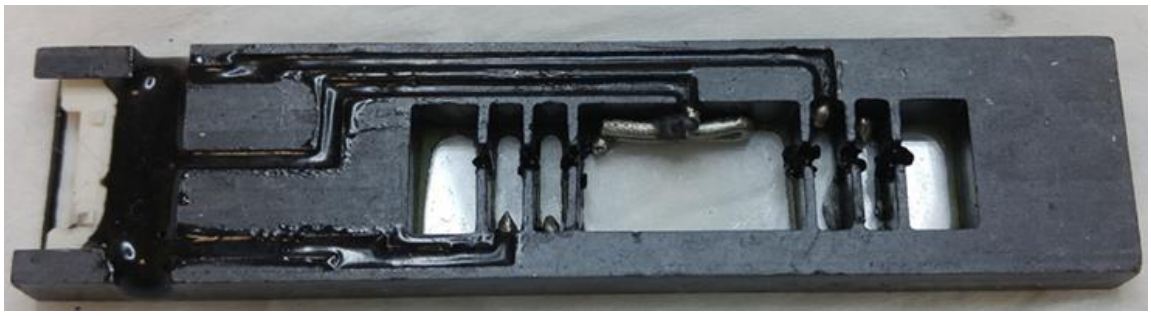

Figure 2-23. Custom nerve chamber designed in our lab (Schoener 2010).
A new nerve chamber contains a transparent window over the whole length of the nerve, allowing for measurements of changes in birefringence at the stimulation and recording sites, and everywhere in between.

#### 2.6.5.2. Peak and slow recovery timecourse as function of distance

Measurements of the XPS as a function of distance are shown in Figure 2-24. A fast onset and slow recovery are apparent, but the slow recovery is more gradual than previously observed. This was attributed to better recording methods that are more sensitive. The peak was found to spread out in time with the magnitude of the slope decreasing, which is consistent with spreading APs in the compound signal.

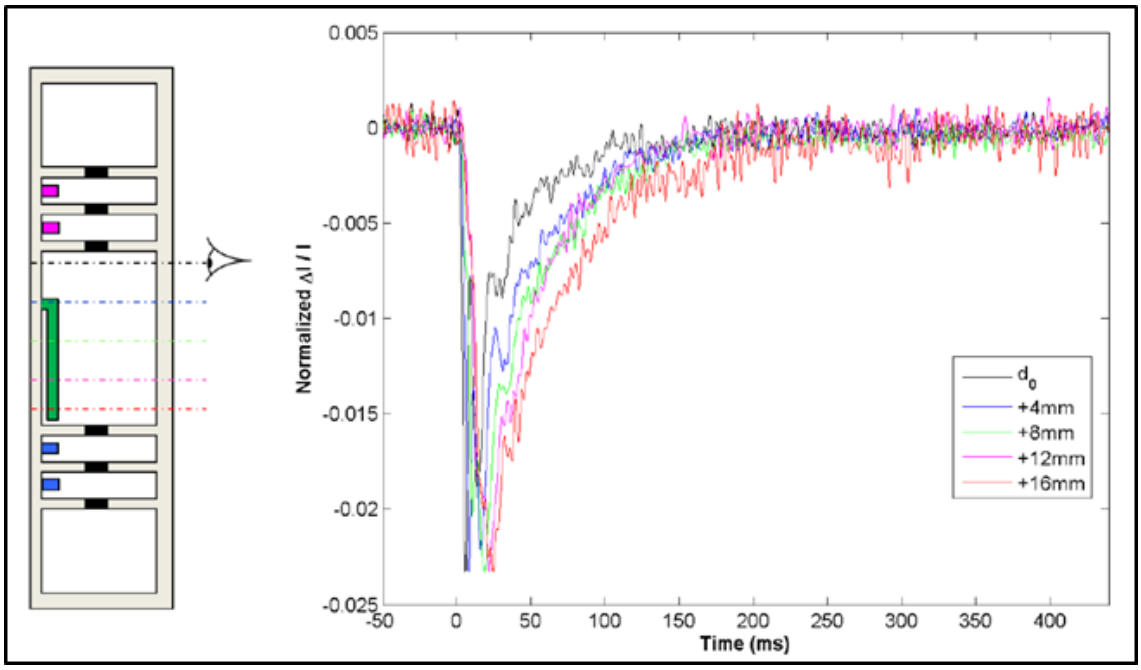


Figure 2-24. Measurements of the XPS as a function of distance (Schoener 2010).
The peak spread out in time and distance, with the slopes decreasing in magnitude, indicative of spreading APs in the compound signal.

2.6.5.3. Horseshoe crab lateral optic nerve

A comparison of the XPS of a complex nerve, such as the lobster WLN, with a relatively simple nerve (with narrow axon size-distribution) has not been shown before, and is instructive because it can yield new information regarding the contribution of axon heterogeneity to the XPS time-course. As shown in Figure 2-25 on the left, at 12 mm from the stimulus site, the XPS of the horseshoe crab LON (with a small variance in axon sizes, see section 2.3.1) shows a significantly narrower peak than that of the WLN, with its broader size distribution. This temporal shape of the XPS for the LON was found to be relatively independent of the distance from the stimulation site, consistent with the size distribution of its constituent axons. The electrical recording corresponding to this LON XPS measurement is shown in Figure 2-25 on the right (overlaid with the XPS), which

shows that the APs in the LON last for a duration of <10 ms, even though the electrical recording is taken at a distance 24 mm from the stimulus. This AP activity matches the width of the peak of the XPS. These data suggest that the peak of the XPS primarily is due to AP activity, while the slow recovery is due to other factors.

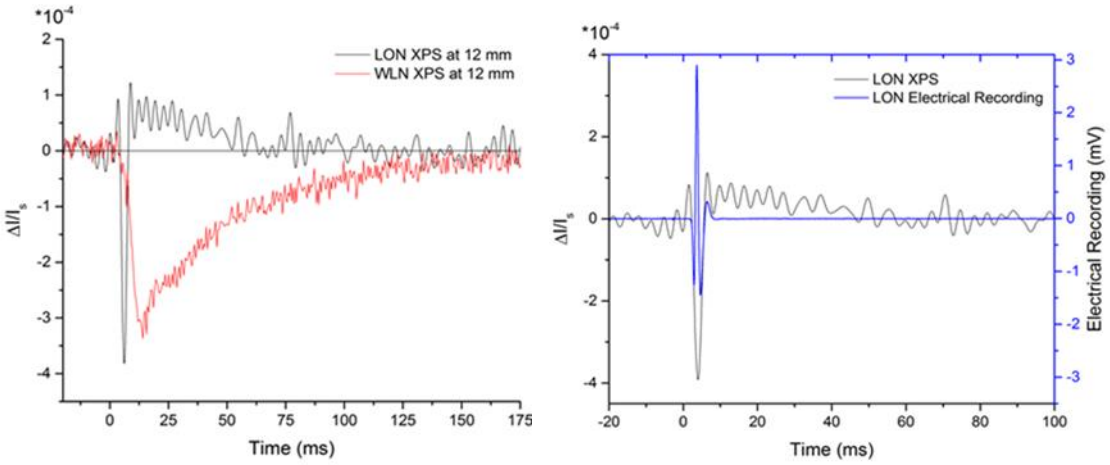


Figure 2-25. A comparison of the lateral optic nerve with the walking leg nerve (Badreddine et al. 2015).

*Left:* The WLN XPS overlaid with the LON XPS. The peak is much narrower for the LON, and the slow recovery happens from above baseline. *Right:* The electrical recording of the LON overlaid with the XPS demonstrates that the peak is entirely confined with the duration of changes in the membrane potential due to APs.

Kurt Schoener also demonstrated a polarity and amplitude dependence on the birefringence signal from applied fields. It was concluded from Kurt Schoener's work that changes in birefringence are driven by direct changes in the electric field, implying that the nerve has a polarizability, and that residual effects may contribute to a slow recovery.

# CHAPTER 3. AIM 1: IMPROVING SIGNAL-TO-NOISE AND FURTHER CHARACTERIZING THE BIREFRINGENCE SIGNAL

## 3.1. Introduction

### *3.1.1. Part 1: Improving methods and SNR*

The crossed-polarized signal (XPS) in nerves (and individual axon) is small, approximately $10^{-4}$ relative to baseline (Cohen et al. 1970; Carter et al. 2004; Badreddine et al. 2015). As such, the signal is often masked by noise so significant that a heavy degree of repeated-stimulus averaging and digital filtering is often needed for it to be detected. Improving the signal-to-noise would make detecting this signal an easier task, and present the XPS as a viable candidate for detecting AP activity in anisotropic nervous tissue. The data presented in section 2.6.4 shows a single-pass trial, but only through heavy filtering (Carter et al. 2004), and it may not have been very repeatable.

The change in birefringence is directly correlated to membrane potential, which *in vivo* conditions exists only within a small pre-established range based on the resting and action potential (AP) states. Therefore, it is not possible to enhance those changes directly, except by recruiting as many APs as possible. However, because the signal is measured relative to baseline, or the static birefringence, it may be possible to reduce the apparent static birefringence to improve the relative signal, which is where we first focused.

Another method to improve the signal-to-noise is by determining the primary sources of noise and reducing them carefully without degrading the integrity of the

signal. There are many type of photodetector noise which can be mediated by the right selection of a detector. Thermal noise, readout noise and dark noise are examples of noises that can be reduced to tolerable levels by selecting the correct detector. The use of stable, low noise photodiodes was the first step to this end, carried over from previous work. Selecting the correct type of light source is also important, as any instabilities would be another source of noise.

One major type of noise which cannot be reduced simply by selecting the right detector is shot noise, which is due to the stochastic nature of the arrival of photons and the conversion to the flow of electrons in the detector. As a random statistical noise, there is no way to decrease shot noise directly, so it is important to select the appropriate detection electronics and to reduce as much other noise as possible. Shot noise is usually dealt with by averaging repeated stimuli, but this won't work if there is any hope of using a signal in real-time studies. Shot noise follows a Poisson distribution, and increases as the square root of the intensity of incident light. The XPS, however, increases linearly with the intensity of light (Schoener 2010). Therefore, the signal-to-noise increases by the square root of the intensity of light.

Improvements to our methodology and to the SNR of the signal in our setup were investigated and the results are summarized in Aim 1, Part 1. The first improvements described involve the sample itself and the field of view (FOV). Then, an optical technique for reducing the static birefringence is investigated using a QWP. The next three described improvements involve a reduction in EMI through better shielding and organization, and a reduction in environmental vibrational noise. A study on light source

stability was also carried out, insofar as it can affect the apparent SNR of the XPS. Finally, a brief discussion on the effective use of digital filtering techniques for improving SNR is provided. These improvements help facilitate the collection of good data.

### *3.1.2. Part 2: Further characterizing the XPS*

The physiological mechanisms underlying the cause of these changes in birefringence in neuronal tissue remain under discussion. One suggested mechanism is cellular swelling, which was found to occur rapidly with the onset of the XPS and to last 10–20 ms in both squid giant axons (Tasaki & Byrne 1993) and nerve bundles (Yao et al. 2003). Cellular swelling was found to be highly correlated with the scattering signal, but not to the birefringence signal, which seemed to precede the scattering signal (Carter et al. 2004). Furthermore, when the timing of the signals from VSDs and intrinsic birefringence were measured simultaneously, it was found that the birefringence signal was directly correlated with, and possibly even preceded, the VSD signal (Foust & Rector 2007).

Other proposed mechanisms responsible for the XPS relate the dynamic electric field of propagating APs to membrane molecular and electron-cloud changes. In one proposition, the reorientation of dipoles (including membrane proteins and phospholipids) away from the radial axis may result in a decrease in birefringence of polarized light (Cohen 1973; Landowne 1985; Tasaki et al. 1968).

For single axons, the XPS was found to predominantly be isolated to areas near or

through the membrane; and in nerve fibers, an appreciable contribution to static birefringence from Schwann cells and connective tissue was noted (Cohen et al. 1970). This complexity in optical signals caused by contributions from adjacent tissue structures presents a significant barrier to the full understanding of the underlying physiological origins of the XPS in higher-order neuronal structures. Additional information would lead to a more complete understanding of the causes of the XPS in nerves and brain tissues.

We carried out a series of experiments with a goal of better understanding the XPS. First, wavelength dependence of XPS was reinvestigated, as there was some previous controversy. Then, distinct features of the XPS timecourse are studied, and our custom model of AP propagation and axonal contributions to the XPS are compared to the empirical data. Patterns of the electrical traces are compared to those of the XPS for overlap. Then, several investigations of the response of the nerve to applied fields are performed. A comparison of the live and 'dead' nerve response, and the response to square (DC-like) applied voltage and sinusoidal field oscillations are studied. These results provide us with valuable insights into the XPS in the lobster WLN.

## 3.2. General methods

A diagram of the optical system used is shown in Figure 3-1A, and is based on Kurt Schoener's work (Schoener 2010). All optical elements were housed in 30 mm cage mounts (Thorlabs, Inc.). Illumination was provided by a 625-nm high-power LED (Thorlabs, Inc. M625L3) for minimizing noise due to source variability (Foust et al. 2008). The LED was driven by an LED driver (Thorlabs, Inc. T-Cube) with variable output current control. Light from the LED was focused using a spherical plano-convex

lens first onto the central plane of the nerve, and then reimaged using a second lens onto a 2.4 mm x 2.4 mm photodiode with pre-amplifier (Hamamatsu S8745-01). The incident light was polarized by a "wire-grid" linear polarizer ($LP_i$) (Moxtek PPL04C), and the light transmitted through the nerve was analyzed by another linear polarizer ($LP_a$) oriented 90º to $LP_i$. The pair of polarizers were placed with their optic axes at ±45° relative to the length of the nerve, providing the maximum birefringence signal (Cohen et al. 1970). Before placing a specimen in the chamber, the measured extinction ratio (transmission ratio of perpendicular to parallel transmission axes) of the crossed polarizers was verified to be ≥1000, to ensure minimal effects of the crossed-polarizer efficiency on the comparison of data sets.

The nerve chamber Figure 3-1B was fabricated from a thermally-conducting but electrically-insulating polymer (Cool Polymers, Inc.) and was cooled using a copper heat pipe of 4 mm diameter (water vapor medium: Enertron HP-HD04DI30000BA), with its distal end in an ice bath, thus maintaining the Ringer's solution (fluid medium specific to the lobster nerve) at ~1–4º C to maintain the normal physiological temperature of the nerve. Petroleum jelly (mixed with painter's charcoal to reduce light scattering) was used to surround the nerve in the openings between the wells to electrically isolate the wells. Two pairs of silver electrodes served to stimulate and record the AP propagation through the electrically conducting Ringer's solution, and were located as indicated in Figure 3-1B. The central chamber electrode was grounded to reduce the effects of charge accumulation in the chamber. The top and bottom of the chamber were sealed with quartz slides, to contain the Ringer's medium, such that optical measurement windows were

available in all fluid sections (wells) of the chamber, as shown in Figure 3-1B. The top window reduced the effects of system vibrations on the fluid-air interface that can introduce optical noise. The chamber was positioned such that the illuminated area laid, typically, in the middle of the central well, ~12 mm from the positive stimulus well, but with that distance being adjusted for specific experiments.

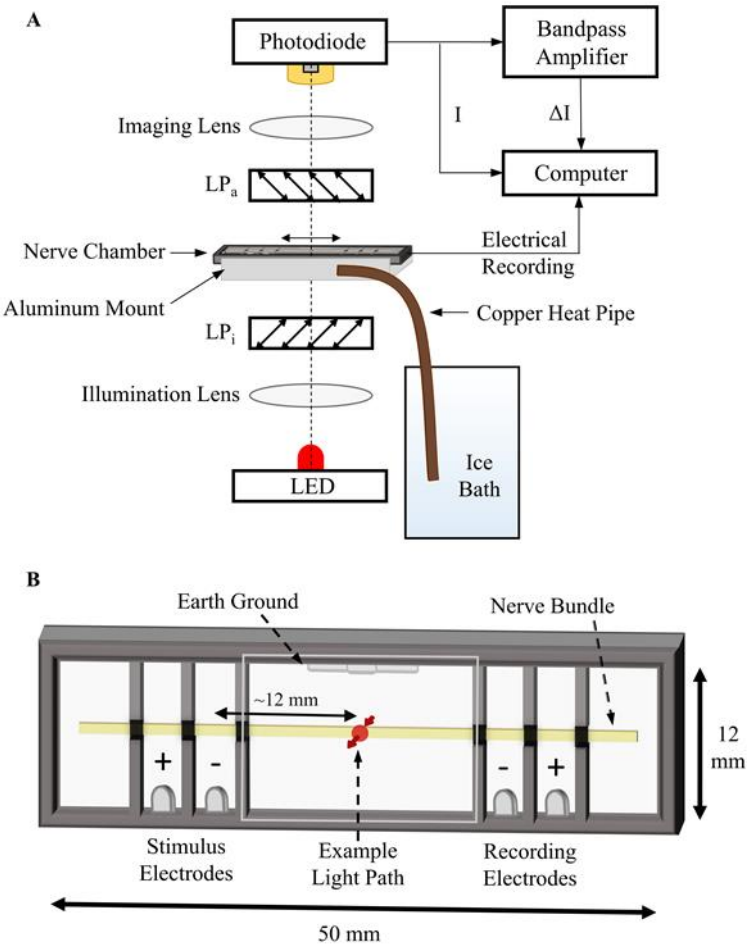


Figure 3-1. Simple diagram of setup and nerve chamber (Badreddine et al. 2015).

A) Diagram of the optical components and readout. B) An expanded depiction of the nerve chamber with quartz top and bottom. Blackened petroleum jelly was used to electrically insulate the areas around the nerve between each well. An example of the illumination area on the nerve in a typical experiment is shown, at ~12 mm from the positive stimulus well.

The photodiode (PD) with preamplifier was operated using a custom, isolated power supply with a set of 9V batteries, and the output signal from the PD preamplifier was split into two lines, as shown in Figure 3-1A. The static birefringence, $I_s$, was measured as light transmitted through the crossed polarizers with no stimulation of APs, and was evaluated directly from one line of the PD's unfiltered output, prior to administering a stimulus pulse. The dynamic birefringence signal, $\Delta I$, was measured by feeding the second PD output line to a low-noise amplifier (A-M Systems, 3000) with a bandpass filter set for cutoffs of 0.l Hz (high-pass) and 1 kHz (low-pass) and amplified by a factor of 100. The high-pass portion of this filter removes the DC component, leaving only the AC component, which is the dynamic birefringence in this case. The electrical signal was measured from the recording electrodes, shown in Figure 3-1B, amplified by a factor of 1000 and filtered between 1 Hz and 10 kHz using another identical amplifier.

For a typical experiment, a walking leg nerve (WLN) from one of the four rostral-most walking legs of a lobster, *Homarus americanus,* was removed using the Furusawa pull-out method (Furusawa 1929) and placed into the nerve chamber, which is shown in detail in Figure 3-1B. The nerve was immersed in *Homarus* Ringer's solution, consisting of 523 mM NaCL, 52.7 mM $MgCl_2$, 13.3 mM KCl, 20.0 mM $CaCl_2$, 5.56 mM Glucose, and 5.0 mM HEPES (Factor 1995).The lobster WLN has ~1000 axons , described in detail in section 2.3.1. The nerve was typically stimulated using a 1-ms, 1-mA (single-polarity) square current pulse from a linear stimulus isolator (WPI, Inc. A395R-C), initiated by a pulse generator (Berkeley Nucleonics, BNC 555) that was gated by a

computer trigger. The stimulation parameters were decided upon through empirical trial-and-error, as well as through communication with other research groups (Schoener 2010). The interference of electrical capacitance between the stimulation electrodes was tested by applying a stimulus with no nerve in the chamber, and the effects were found to be significantly less than when a nerve is placed in the chamber (Badreddine et al. 2015).

The optical birefringence and electrical signals were collected using a 16-bit, 1 MS/s analog-to-digital converter (National Instruments, PXI-6120). System control and data analysis were performed using Matlab®. The XPS, expressed as the relative dynamic birefringence $\Delta I/I_s$, was calculated by dividing the dynamic birefringence signal for each stimulus period by a 50-ms pre-stimulus mean of the static birefringence signal, after adjusting for the gain of 100 from the amplifier. Unless otherwise specified, $\Delta I/I_s$ was calculated by first averaging the traces generated by 100 consecutive stimuli, and then applying a computational bandpass filter between 0.1 Hz and 1000 Hz to the averaged traces, which will not remove relevant signal information, since an AP spike lasts around 1–2 ms.

## 3.3. Part 1: Improvements to methods and SNR of the birefringence signal

### *3.3.1. Nerve trunk size and XPS*

One of the biggest problems with using whole nerve trunks (around 2–3 mm in diameter) was that neurons near the center of the nerve bundle may not be stimulated. During an experiment, any light that passed through those fibers resulted in a direct increase in $I_s$, which resulted in a decrease in the signal, as in $\frac{I_{dynamic}-I_{static}}{I_{static}}$, because

those fibers were not stimulated but still contributed to the static birefringence. The signal received by the photodiode must be thought of as a combination of ΔI/I for each neuron. The interstitial tissue does not contribute substantially to the peak of the dynamic signal (Ross et al. 1977). Therefore, it was concluded that for a given irradiance, the net signal would be higher for smaller subsets of the nerve trunk.

The lobster WLN trunk is generally 2–3 mm in diameter. It can be readily teased apart into subsets of varying sizes. For this experiment, we took subsets of the nerve bundles that were 0.25 mm, 0.5 mm and 1 mm. The stimulation magnitude had to be adjusted accordingly. The stimulation strength was increased for each subset until a maximum electrophysiological (ephys) response presented, at which point the stimulation current was reduced slightly to prevent overstimulating and killing the outermost axons. Usually, this stimulation strength was close to the standard stimulus magnitude of 1 mA. The best signal came from a nerve subset with a diameter around 0.5 mm, which produced signals around $3 \times 10^{-4}$ with an SNR~6 after only 50 trial averages, a substantial improvement. It also is possible that reducing the nerve diameter also reduces the likelihood that light undergoing birefringence loses its polarization state due to scattering effects.

### *3.3.2. Illumination field size and XPS*

Due to linear polarizer deficiencies, the extinction ratio, which can be defined as the ratio of light which traverses through two polarizers when parallel to that which propagates through when the polarizers are crossed, was limited to around 1000:1. For smaller nerve subsets, light which did not pass through the tissue but was detected (and

therefore not filtered appropriately by the polarizers) was a bigger concern than for whole nerve trunks. This light directly reduced the signal by acting as a 'false positive' for static birefringence when there could consequently be no contribution to $I_{AP}$.

Using a nerve subset of 0.5 mm in diameter (explained in section 3.3.1), we changed the illumination field from 0.25 mm to 0.5 mm to 1 mm while focusing all of the light onto the photodiode. It was found that the signal increased substantially when the illumination field size was matched to the nerve diameter (roughly 0.5 mm) when compared to the 0.25 mm diameter. This may be due to an overall loss of light. The 1 mm field averaged some light that passed through the polarizers due to efficiency limitations with light from the nerve tissue which had experienced birefringence effects. We concluded that the best signal-to-noise is generated when the illumination field matches the bundle size. A more thorough experiment would use a stable light source (minimal high frequency variance in light output) with an even-intensity distribution across the illumination field.

### *3.3.3. Use of quarter waveplate to reduce static birefringence*

A quarter waveplate (QWP) is a birefringent material that can induce a circular polarization from incident linearly polarized light at a given wavelength. The addition of a QWP before the LP analyzer in our setup could improve the signal by canceling out some of the elliptical polarization induced by the nerve, reducing the overall static birefringence. However, nerves are highly complex structures, and each point within the bundle may induce a different ellipticity on incident light, based on molecular dipole and E-field variations along the axolemma (axon membrane). Due to those microscopic

variations in optical activity, light that is transmitted through several layers of neurons may experience different degrees of rotation, represented by varying states of ellipticity along the nerve bundle upon passing through the QWP and LP.

Using a QWP designed for visible light, light illuminated in the manner described in section 3.3.2 was manipulated slightly (keeping its fast axis near the optic axis of the incident polarizer) and the signal measured. This modified-XPS was not found to improve the SNR, which may be due to at least two factors. First, a QWP is truly only capable of behaving perfectly at one discrete wavelength. Second, applying a single QWP across the whole field and sensing all of the light on the detector serves to sum areas where the ellipticity was increased with areas where the ellipticity may be decreased, which cancels out any gain from using the QWP. The setup needs to be modified to use a 2D detector array and a single-wavelength source. A helium-neon laser and a QWP would be good options.

### *3.3.4. Improved cable shielding and grounding*

Electromagnetic interference (EMI) is a common means of noise entering a measurement setup. Noisy electronics that are improperly grounded or too close in proximity to sensitive recording devices and cables carrying weak signals can introduce artifacts and sinusoidal noise that masks those signals. Even worse, the noise can be mistaken for a signal. Therefore, it is extremely important to carefully arrange the electronics and sensitive device cables to minimize EMI. Any cables used have to be thoroughly insulated and made to avoid contact with adjacent cables.

The stimulation and recording cables were better insulated from one another and the grounding was improved (grounded to a single point on the table, then to earth ground). This minimizes feedback through the grounding cables and also reduces EMI. The photodiode readout cable was better insulated and diverted from the power, control and stimulation cables. The NI DAQ chassis and amplifiers were separated from the other electronics and the data input cables were better insulated. These improvements led to a reduction in the pickup of random spikes, sinusoidal EMI and ground feedback.

### *3.3.5. Improved enclosure/shielding and electronic setup*

A new custom enclosure, shown in Figure 3-2, was built from plywood. Sheets of aluminum were used around the exterior to act as a Faraday cage to prevent exogenous sources of EMI from introducing noise to the system. A copper mesh was used to construct a malleable 'door', with a black curtain attached to reduce ambient light. The analog stimulation and amplifier devices were placed in the enclosure with the optics, while the remaining electronics were placed in the other enclosure. This served to prevent EMI from being picked up in the pre-amplified signals. This new enclosure system, coupled with improvements to the cabling, served to increase the effective SNR by reducing random and interference noises.

Figure 3-2. New custom-built system dual enclosures.

The enclosure on the right houses the optics, amplifiers and current-source stimulator, while the enclosure on the left houses the remaining (mostly digital) electronics.

### *3.3.6. Use of anti-vibration materials in setup*

Often during experiments, vibrations from the environment would arise. The optical bench is floating but vibrations could still find their way into the setup and be picked up by the sensitive electronics and optics. A few steps were taken to ensure the vibrations would be reduced. First, sorbothane pads (Isolate It!©) were added under the NI DAQ chassis to reduce vibration from its cooling fan from being transferred to the bench. Then, the computer was removed from the bench, and the chassis was moved into the middle of the enclosure further from the optics. Finally, more sorbothane pads and a medium-dense foam (Du-Bro) were added under a mounting plate used to mount the optics, which isolates the optics from vibrations. An example of the results of these steps is shown in Figure 3-3.

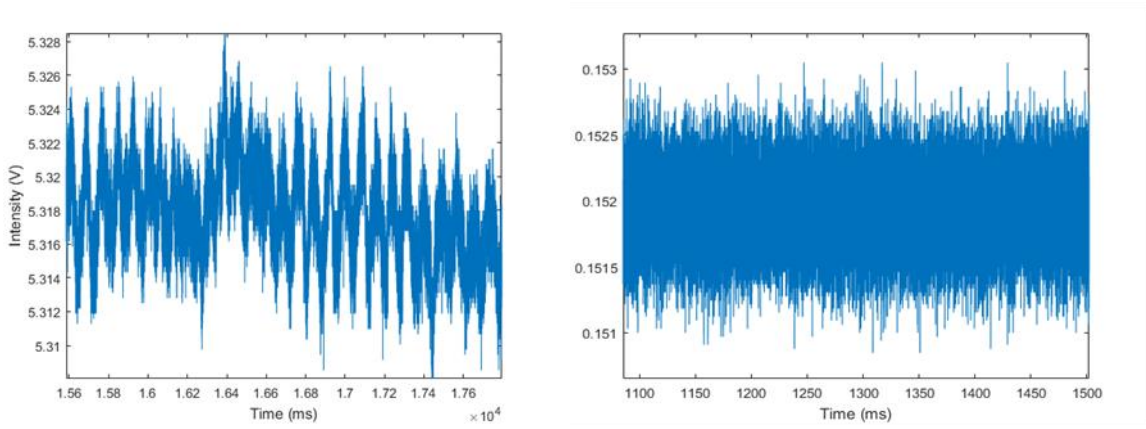


Figure 3-3. Vibration noise.

*Left:* Noise from vibrations in the setup. *Right:* A signal after implementing anti-vibration steps.

### *3.3.7. Stability and output of light source*

The choice of light source affects the apparent stability of the readout intensity, which in turn affects the system noise. If the light is too unstable (not perfectly DC, or flat) in the range of frequencies involved in the XPS, then that instability could mask any change in birefringence for a given stimulus period. So, when averaging multiple stimulus periods, the dynamic birefringence may be recorded as lower than it should be. This, coupled with increased noise from the instability itself, significantly reduces the SNR. Multiple light sources were investigated, producing the intensity readouts shown in Figure 3-4. Plot A is from a He-Ne laser, B is from a laser diode at 633 nm, C is from a superluminescent diode (SLD) (Superlum SLD-260-HP1-TOW2-PD), and D is from the standard red LED mentioned in section 3.2. For our purposes, the He-Ne laser and laser diode are not compatible with these studies, as they are too unstable in the span of time typically involving changes in birefringence, and will especially complicate any study

attempting to record ‘real-time’ signals. Some of this instability could be caused by vibrations in the setup, or particles in the air. Both our SLD standard LED are fairly stable. The SLD can be focused more tightly, so for smaller nerves it was found to be more useful, but for lobster WLN, the LED is used because it is slightly more stable, although random spikes in the output do occur.

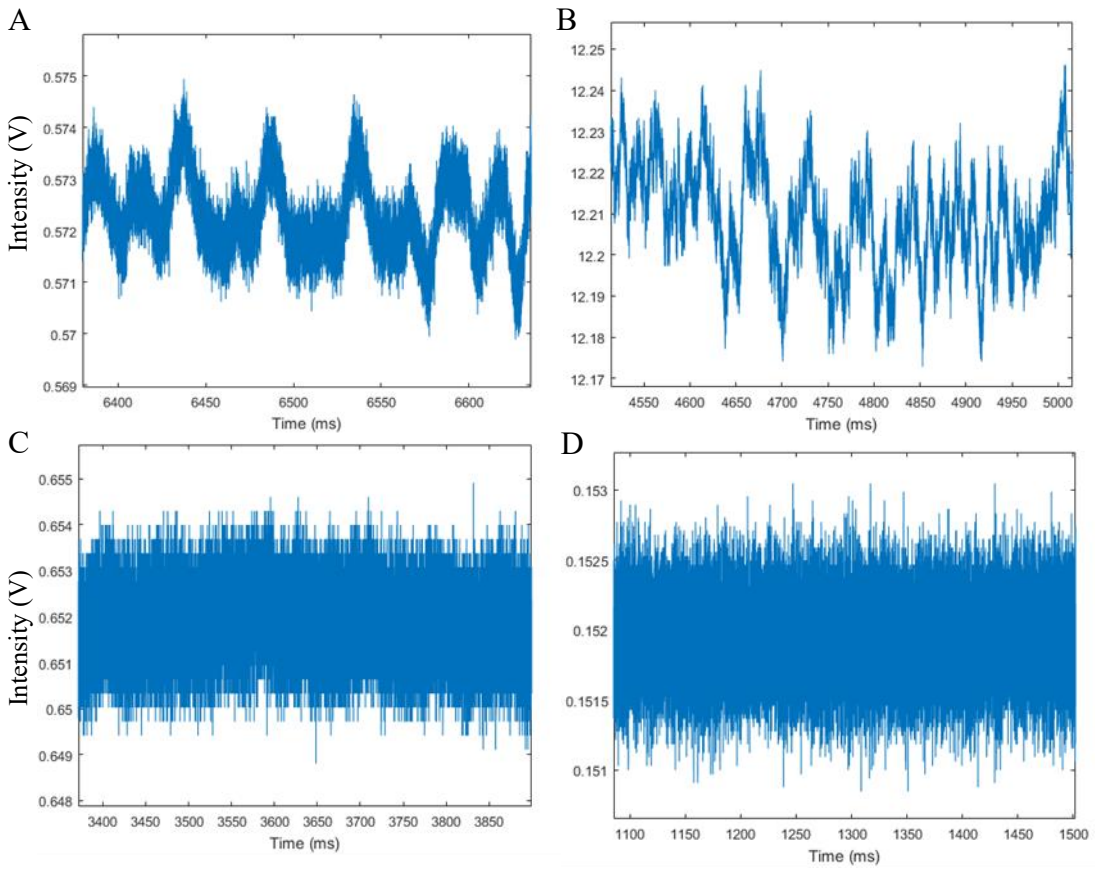


Figure 3-4. Stability of light sources

The intensity of light as read out by the amplified photodiode is shown for a helium-neon laser (A), 633 nm laser diode (B), super luminescent diode (C), and standard red LED (D).

### *3.3.8. Digital filtering*

A variety of digital and analog filtering techniques were tested to investigate the most feasible way of improving the effective SNR of the data. The analog filter is described in section 3.2 and involves a bandpass between 0.1 Hz and 10 kHz. This is an improvement on previous work which suggests that a range of only 1 – 300 Hz is sufficient to obtain the optical signal (Schoener 2010). While initially some of the data here was collected using an analog bandpass filter, it was found that the SNR appears better when no analog filter is used and instead only digital filters are applied. These are to remove drift, random spikes, vibration noise, interference where needed, and any components of the data that are outside the expected frequency range of the signals.

Drift is a relatively slow, DC change in the data which can affects the signal insofar as it is a measure of dynamic birefringence relative to baseline. The drift is removed by first parsing the data into each stimulus period, and then taking the mean of the last few values and subtracting the mean of the first to values. The resulting slope is used to calculate a line which is used to weight the data values accordingly and correct the drift. This correction is done before averaging because an increasing drift averaged with a decreasing one may result in a removal of relevant signal components. If the optics are performing well, this is not generally a concern, but it was a common problem.

Random spikes occur regardless of light source, but especially for the MLED (Thorlabs). These spikes were treated as any part of the intensity readout which were greater than 2 standard deviations from a local mean of the data (say, 100 points at a SR of 100 kHz). These outliers were replaced with an average of the two values immediately

preceding and following them.

Vibration noise and aliased electromagnetic interference (EMI) generally present as sinusoidal oscillation noises. As such, they were easily removed by using a notch filter set to the apparent noise frequency. However, vibration noise often occurs in the range of frequencies that correspond to signal components. So, for those, high order (sharp) cutoffs were selected so that only a particular frequency was removed, maintaining a maximum amount of information of the signal.

To remove non-relevant frequency components of the data, a few filters were attempted, both finite-impulse response (FIR) and infinite-impulse response (IIR). For FIR, a simple moving average window filter of 50 points (for SR of 100 kHz) proved to be the most useful in smoothing the data. The best IIR filter was one designed as a $4^{th}$ order Butterworth bandpass from 0.1 Hz to 1 khZ in Matlab's filter toolbox. Combining these two filters (in the order presented) provided the best SNR of filter combinations attempted.

### *3.3.9. Discussion*

Because the XPS is so small, it is often masked by noise which requires multiple stimulus periods to be averaged to remove shot noise, and digital filtering is often needed for it to be detected. Additionally, while previous research has yielded signals which are relatively good and even work in single-pass trials (Carter et al. 2004), further improvements to the electronics and optics setups are necessary to further improve the SNR and make the XPS a viable means of monitoring neuronal activity *in vivo*.

To this end, testing the effects of a reduction in the nerve trunk size and illumination field size on the effective SNR proved useful. This served as an indication that a control on the sample placement in the setup as well as the positioning of the light source and field of view can be carefully manipulated to improve the SNR of the XPS. While the use of a quarter waveplate did not provide any gains, it did provide some insights and its implementation could be more carefully performed in future studies. Namely, the use of 2D arrays with the QWP may provide more information, since the effect of the QWP can be positive or negative on the birefringence of a given position, averaging out any improvements if you sum them all together across the field.

Improvements to the entire setup by reorganizing the electronics and optics into a custom-built enclosure with a Faraday cage served to improve SNR by reducing internal sources of vibrations, and external EMI. It also made managing the cables and electronics easier and provided more maneuverability around the setup. Further improvements were made by adding or improving the cable shielding and grounding of the electronics. These improvements served to reduce signal loss and EMI.

Various forms of instability in the setup contributed to forms of noise. These came in both a mechanical form through vibrations, and an electronic form through light source instability. These were dealt with by careful investigation and selection and implementation of materials. When they could not be successfully removed, digital filtering helped to remove the rest. By selecting the appropriate filters, the SNR of the processed XPS was improved. Together, these improvements made studies of the XPS easier to perform and provided cleaner looking data than in the past.

## 3.4. Part 2: Further characterizing the birefringence signal in lobster walking leg nerves

### *3.4.1. Revisiting wavelength dependence of the XPS*

Static birefringence is known to have a wavelength dependence due to the interaction of light with dipoles (or quadrupoles, etc.) or dielectric media in neurons which induce the optical phenomenon (Cohen, LB, Keynes, RD and Landowne 1972; Ross et al. 1977). However, the possibility of wavelength dependence on the XPS was unknown. Since it could have implications on both the physiological origins of the XPS as well as on improvements to system SNR, it was explored here. Initial measurements were made by Kurt Schoener, but rigorous measurements were not carried out and the system was not designed to allow for switching between LEDs of different wavelengths without inadvertently manipulating the apparent XPS magnitude. Switching LEDs was of primary concern here because errors to source-related and optics-related variations in the optical path of each LED through the tissue, as well as LED positioning errors, needed to be minimized to facilitate an adequate comparison of the XPS and wavelength. Therefore, principles of Kohler illumination were implemented in the setup.

The basic idea of Kohler illumination is to evenly illuminate the sample by collimating the light from the source. This is done by using a collector before condenser. In short, the collector contains a lens and an aperture. This aperture limits the field-of-view on the sample. The light passing through the collector is focused onto the condenser's aperture. The condenser is adjusted in position so as to provide approximately parallel illumination over the sample, and the light is then shifted twice by two lens sets to focus it onto a detector. In the case of studying wavelength dependence,

this is useful because the two apertures used in Kohler illumination effectively control the optical path, eliminating variations in the light source. This way, only the irradiance varies between the wavelengths, which is not a problem because the signal is not dependent on the static birefringence, as it scales linearly with the XPS (Schoener 2010).

The data collected in this experiment is shown in Figure 3-5. Due to limitations on the efficiency of the polarizers with regards to wavelength range, only three wavelengths could be chosen: 470, 530 and 629nm. The other option was to use Moxtek polarizers, but those were only efficient enough for two accessible wavelengths at the time, 629 and 800nm. Therefore, the Edmond Optics polarizers with the aforementioned three wavelengths were used. In order to calculate the data shown, the signal (representing the peak of the response) at each wavelength in a trial was divided by the average of the signals for the three wavelengths. The average of those values across 18 trials was taken for each wavelength and is shown with an average standard deviation of 0.036. No wavelength dependence was observed, as the error bars overlap substantially and no point was more than ~1% off of the mean after averaging. This averaging even included possible outliers in the data. A lack of wavelength dependence is coincident with Cohen et al.'s (Cohen et al. 1970) briefly mentioned observation in crab leg nerves, and implies that the structural and electrical properties of the nerve responsible for the dynamic birefringence are also at least a component of that responsible for the static birefringence.

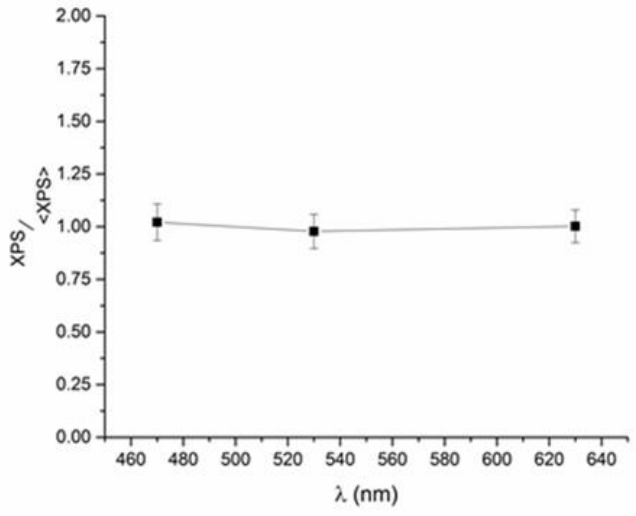


Figure 3-5. Testing wavelength dependence of the XPS.

There is no wavelength dependence on S (ΔI/I), as demonstrated by the use of three wavelengths, 470, 530 and 629nm. $S_{avg}$ was calculated by averaging S for all three wavelengths for each trial individually. N=18 trials of log(S/Savg) were averaged.

*3.4.2. Reassessment of the XPS peak and gradual recovery timecourse*

The nerve chamber facilitated the study of the birefringence signal in the lobster walking leg nerve (WLN) at the negative and positive stimulation wells (see Figure 3-1B) and at various distances from the stimulus site (Schoener 2010). The lobster WLN is composed of ~1000 axons of variable diameter, which give rise to a compound crossed-polarized signal (XPS) that changes in shape as a function of distance from the stimulus. Each nerve has a unique distribution of axons, and while the corresponding XPS as a function of distance varies, the general temporal pattern is consistent across nerves.

Figures 3-6A and 3-6B show the XPS data as a function of distance from the point of stimulus for a WLN (plotted for distances of 6 mm, 12 mm and 24 mm). Figure 3-6B presents the same data as Figure 3-6A, but adjusted in time to account for delays in the onset and to facilitate an analysis of the relative temporal shape of the signal. As can

be seen, the peak of the XPS is incrementally delayed as a function of distance from the stimulus point, and its magnitude decreases while the peak width increases. We found that the delays in the peaks are consistent with Carter et al. (Carter et al. 2004). Here, we extend the measurements to a 24-mm range and demonstrate a much clearer picture of the spreading XPS peak as a function of distance. By carefully translating the nerve chamber without changing the optics, we were able to facilitate an accurate comparison of the XPS amplitude as a function of distance, showing a decrease and broadening of the peak, as well as the recovery of the signal to baseline at each distance. The peak of the XPS at the stimulus wells is larger than the typical signals presented here and by others and is due to the effect of a direct perturbation of the applied electric field on the biophysical structures responsible for the birefringence signal.

We found that the XPS of the WLN presents with four distinct phases, as identified in Figure 3-6B; 1) a slower initial onset, 2) a faster second-stage of the onset, 3) a fast initial recovery of the peak, followed by 4) a gradual recovery to baseline. The four phases are not all evident at the stimulation site, most likely due to direct interference from the stimulus pulse. The slow and fast onset phases are present in the traces at all distances from the stimulus site. After a distance of ~12 mm, the fast recovery in the trace begins to merge with the gradual recovery. The gradual recovery appears to be approximately the same at any distance from the stimulus site; however, at the stimulus site, the gradual recovery begins at a smaller magnitude. This provides new information about the features of the timecourse of the XPS.

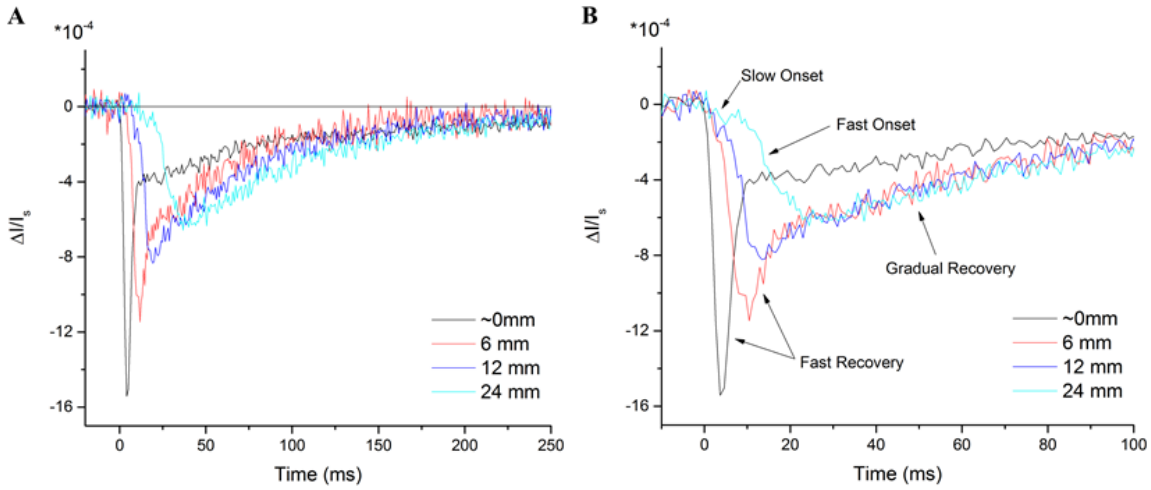


Figure 3-6. Features of XPS as a function of distance (Badreddine et al. 2015).

A) Crossed-polarizer signal (XPS) for the lobster walking leg nerve (WLN) from a 1-ms, 1-mA stimulus pulse, measured at the negative stimulus electrode (origin of APs) as well as at 6 mm, 12 mm and 24 mm from the site of stimulation. The XPS peak decreases in magnitude and widens in time as a function of distance. Four phases are noted: a slow onset, a fast onset, a fast recovery of the peak, and a gradual recovery to baseline. The gradual recovery takes ~300–400 ms to return fully to baseline (not shown). B) The same data is temporally shifted to match the start of the onset of the XPSs to compare the onset and recovery times. The gradual recovery is similar for any distance from the stimulus, but is different at the stimulus site.

### *3.4.3. Arrival-time-based AP model of the XPS*

The cause of the observed long tail of the gradual recovery of the XPS was not understood or well-explained. To study whether the distribution of action potential (AP) velocities for the size-range of axons is sufficient to explain all phases of the XPS, a model that depicts the spreading AP birefringence signal as a function of distance from the stimulus point in the lobster WLN was generated in Matlab®. This simulated compound XPS was calculated as the sum of the individual axons comprising it. The shape of each axon's XPS was designed to match the shape of the optical response measured by Cohen et al. (Cohen et al. 1970), by using a 5$^{th}$ order chi-squared

distribution (chosen strictly to shape the computational signal appropriately) with a variable time window ($T_w$) for the XPS, and assigning the amplitude of the peak to be on the order of $10^{-6}$. This magnitude was chosen through trial-and-error to produce the correct summed compound signal of $10^{-4}$ to $10^{-3}$.

The relative velocities of axon APs was calculated as the ratio of the square root of the axon diameters; which holds true for unmyelinated axons (ignoring, for simplicity, membrane resistance, which varies randomly between adjacent axons) (Hodgkin 1954; Nicholls et al. 2012). The empirically determined maximum velocity of ~5 mm/ms (from the initial rise of the electrical recording) was assigned to the largest axons (~100 μm). The relative contributions of the XPS (*rXPS*) as a function of axonal diameter was treated as an adjustable parameter, since it has been reported that smaller neuronal processes may have a higher relative XPS (Carter et al. 2004). The simulated compound birefringence signal is a sum of the individual contributing axon XPSs ($XPS_{Axon}$, an example of which is shown in Figure 3-7A), each of which can be represented by Equation 3-1.

$$XPS_{Axon} = rXPS * T_w * \left( 5mm/ms \frac{\sqrt{d}}{100\mu m} \right) \qquad \text{Equation 3-1}$$

This model assumes an axon size distribution in three groups as described, in particular, by De Lorenzo et al. (Darin De Lorenzo et al. 1968). For simplicity, axon diameters across the nerve were assigned using three normal probability distribution functions $\Phi$, defined around a mean μ and standard deviation σ as per Equation 3-2,

$$\Psi = k\Phi\left(d,\mu,\sigma\right)\begin{Bmatrix} k=0.5\mu m, & \mu=1.2\mu m, & \sigma=5\mu m, & 0.1\mu m < d < 5\mu m \\ k=0.25\mu m, & \mu=26.7\mu m, & \sigma=8\mu m, & 20\mu m < d < 30\mu m \\ k=0.25\mu m, & \mu=67\mu m, & \sigma=10\mu m, & 50\mu m < d < 100\mu m \end{Bmatrix} \quad \text{Equation 3-2}$$

where $\Psi$ is a probability density function for the axon distribution, $k$ is a scaling factor based on the percentage of total axons falling into that size range, and $d$ is the axon diameter. $\Psi$ is evaluated for the total number of axons in the nerve (typically ~1000). σ is not described previously, and therefore was approximated to smooth the output compound signal. Equation (2) is an idealization of three size groups and is used to provide the distribution of values for $d$ and $rXPS$ and for the loop that calculates $XPS_{Axon}$. A depiction of the computed axon size distribution is shown in Figure 3-7B. All calculated $XPS_{Axon}$ waveforms are summed to construct the simulated compound XPS waveform.

As shown in Figure 3-7D, the model can reliably reproduce the slow and fast phases of the onset, as well as the initial fast recovery, present in the XPS traces (refer to measured traces in Figure 3-6B). We found that the smaller overall number and larger range of diameters of the giant and medium axons was sufficient to reproduce the distinct onset phases of the XPS at approximately the correct times. Said another way, the general shape of the XPS peak is a product primarily of the axon size distribution, with sharp features smoothed out presumably due to subthreshold ephaptic and capacitive coupling. No adjustment of the relative XPS as a function of axon diameter was necessary to reproduce the data for those phases. The gradual recovery phase, however, could not be reproduced, regardless of the size of the temporal window for the constituent axons. If the physiological parameters such as AP velocity, axon diameter distribution and number of

axons are artificially adjusted outside the normal ranges, then the gradual recovery can be reproduced, but the peak then becomes too wide and the onset phases are merged (not shown). In short, the gradual recovery phase cannot be explained on the basis of a range of AP propagation speeds, but could be explained by a capacitive smoothing due to charge accumulation and capacitive effects from surrounding non-axonal tissues.

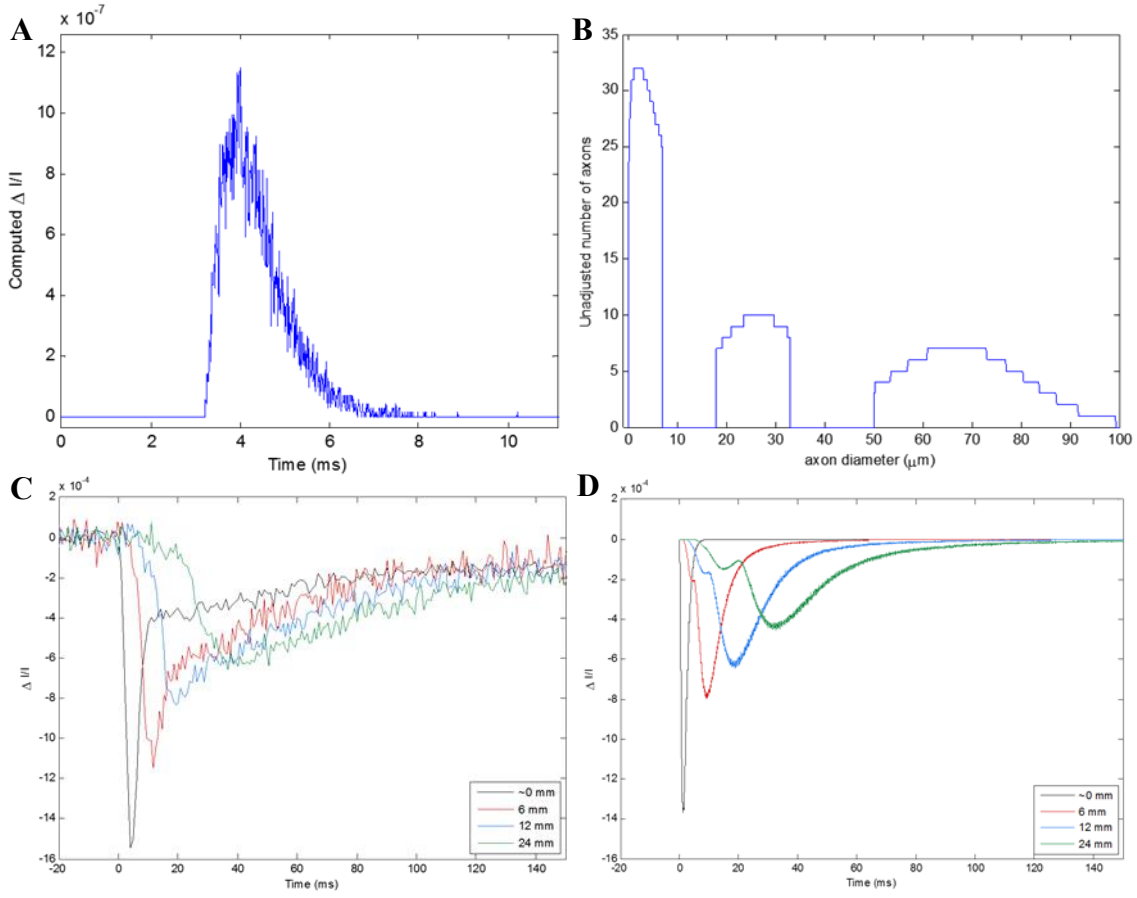


Figure 3-7. AP model comparison to distance-based XPS peak and recovery timecourse (Badreddine et al. 2015).

A) A computation of the simulated single axon XPS is shown. B) The distribution of the axon sizes is computed for three distinct groups which represent the morphology of the lobster WLN. C) For reference, the measured XPS traces at distances from the stimulus of 0, 6, 12 and 24 mm are shown. D) At those same distances, the computed compound

XPS timecourses are shown. The peak is reproduced fairly well, but the gradual recovery is not.

### *3.4.4. Correlation with electrical recording*

In Fig. 3-8, a comparison of the electrical recording and XPS measured close to the electrical recording site for both 2-Hz (A) and 14-Hz (B) stimulation rates is shown. As is the case with the XPS, the electrical signal in the faster stimulation rate is forced to return to baseline just before the subsequent stimulus event. For the 2-Hz stimulation rate, the duration of the return to baseline of the electrical signal is in a range 300–450 ms (depending on the sample), and is generally about the same for the XPS. The temporal widths of the peaks of the electrical recordings coincide with the XPS peaks for both the 2-Hz and 14-Hz stimulation rates. The gradual recovery of the XPS also coincides well with a slow recovery in the electrical recording, further indicating the effect is correlated to capacitive charging and discharging. Features of the peaks which are evident in the electrical signal due to the different in arrival times of axon size groups are not as clear in the XPS traces, presumably due to subthreshold electrical phenomena and surrounding tissue capacitance. Previously, groups did not report on these comparisons because the traditional recording methods rely on a much higher cutoff frequency for the high pass filter.

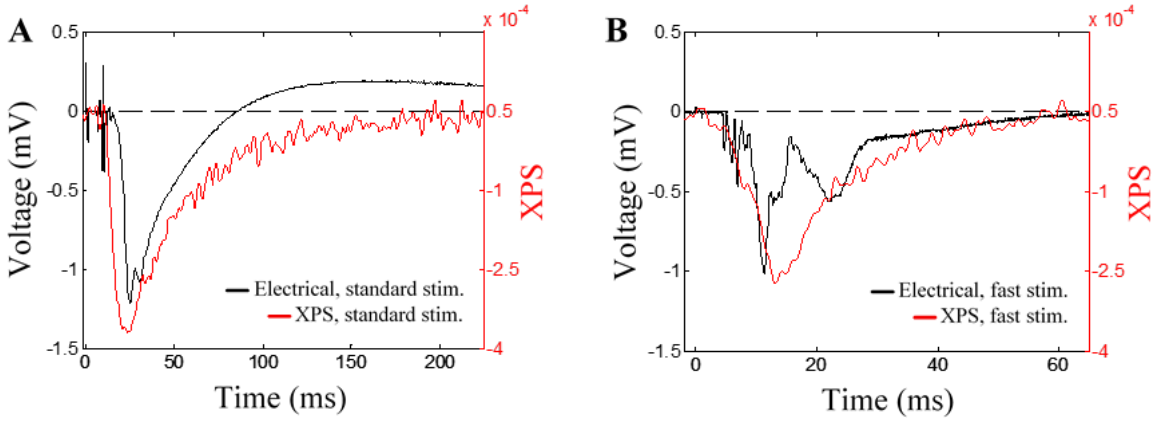


Figure 3-8. XPS overlaid with the electrical recordings.

A) The electrical recording (black) and XPS (red) at a standard stimulation rate, 2 Hz. The nerve demonstrates an adaptive response to the faster stimulus, and no reversal of polarity, which is evident with a standard stimulation rate. B) The electrical recording (black) and XPS (red) at a faster stimulation rate, 14 Hz. The XPS peak width is reduced with a faster stimulation, which may indicate a reduction in the recruitment of axons to generate action potentials as a result of adaptation to fast stimulation. The peak of the XPS coincides with the peak of the electrical recording for both fast and standard stimulation rates.

### *3.4.5. Live and 'dead' nerve XPS response comparison*

Once extracted, lobster WLNs generally remain viable for up to ~2 hours, after which they will no longer generate action potentials in response to stimuli. Nonetheless, the applied electric field in the stimulus wells can force local changes in ion distributions and in the polarization of the nerve fiber structures in that location (hyperpolarizing or depolarizing), thereby inducing dynamic changes in birefringence, independent of action potentials. Standard 1-ms, 1-mA, and stronger 1-ms, 10-mA pulses, were applied to a live nerve, and to the same nerve after it no longer generated APs (>2 hours after extraction), and the XPS was recorded at the windows of either the positive or negative stimulus electrode (see Figure 3-1B). This provided new information on the optical effects of an

externally-applied electric field on the nerve tissue structures, without the confounding perturbations of generated action potentials or the use of exogenous substances.

When standard stimulus pulse currents of 1 mA and a 10 mA (and 1 ms width) were applied to a nerve in both live and 'dead' conditions, and the XPS was measured in the positive and negative stimulus wells, the birefringence was found to follow the applied field, both in polarity and magnitude (Figure 3-9). The positive-well XPS for a 1 mA stimulus in a live nerve (Figure 3-9A) demonstrated a short increase in birefringence attributed to the stimulus itself, followed by a standard XPS time-course associated with the firing of APs. For the 10-mA stimulus, again in the positive polarity well, both live and dead nerves exhibited a gradual recovery from above baseline (Figures 3-9B and 3-9D). The gradual recovery time-course was extended by greater than a factor of 2 for the 10-mA stimulus compared to the 1-mA stimulus. The shape of the XPS in the negative-stimulus well was similar regardless of the stimulus amplitude or whether the nerve was alive or dead.

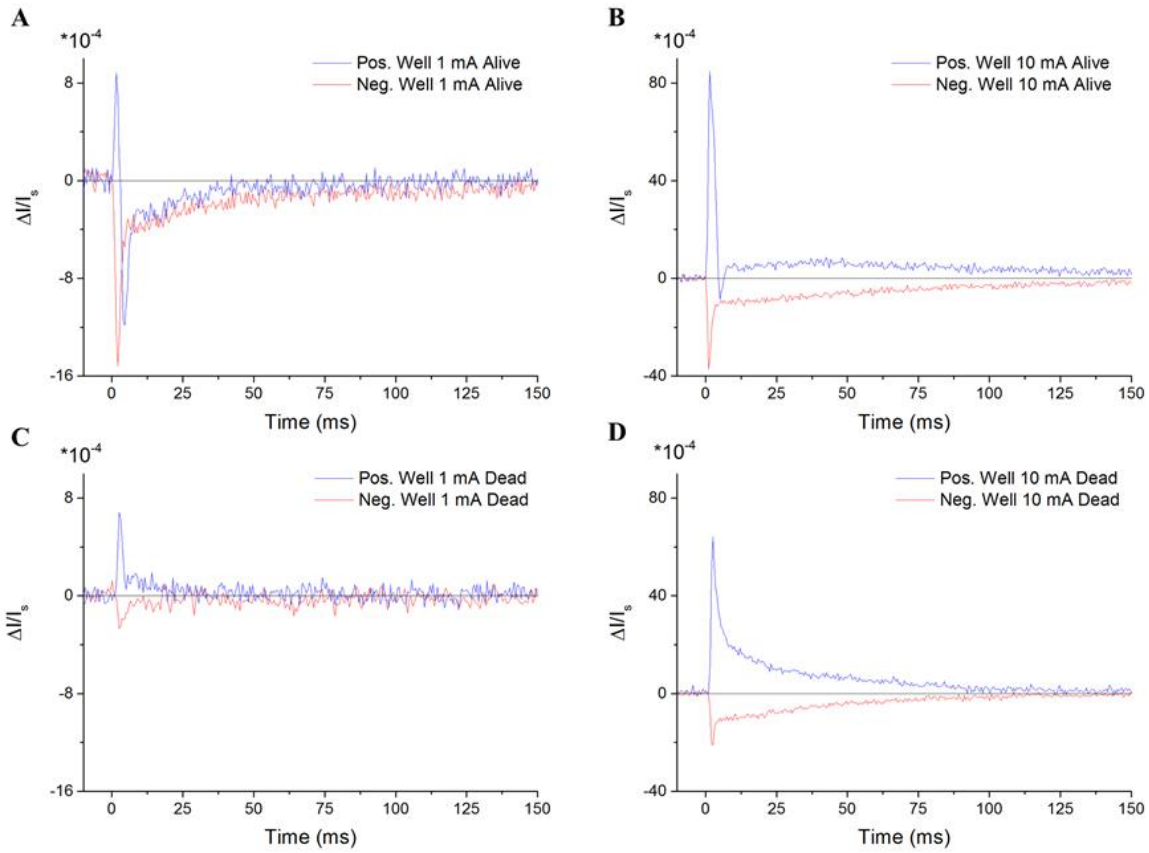


Figure 3-9. XPS response at stimulus site to applied fast current pulses (Badreddine et al. 2015).

A) The XPS in the positive and negative stimulus wells with a 1-ms, 1-mA stimulus pulse in a live nerve shows an immediate peak correlated with the stimulus pulse followed by a standard shape associated with normal AP activity. B) A 10-mA stimulus pulse in a live nerve causes the XPS to recover from above baseline instead of below. C) The dead nerve XPS for a 1-mA stimulus is much smaller than for the live nerve, but is still present. D) For a 10-mA stimulus on a dead nerve, the XPS onset is an order of magnitude larger than for a 1-mA stimulus, and the gradual recovery is significantly longer (>2x).

### *3.4.6. Linear electro-optic response*

To investigate the effect of applied fields on both the amplitude and temporal response of the nerve, square voltage pulses, 128 ms wide, were applied to the nerve with voltage amplitudes of 100 mV, 200 mV, 400 mV, 750 mV, 1 V, 2V and 5V. The voltage

was generated by the DAQ card (National Instruments) and passed through an analog output channel. The XPS of the nerve was measured at the positive stimulus electrode well (as opposed to the negative well, for consistency due to the fact that the signal has a polarity dependence). The time constants of 63% of the rise and fall times for the resulting dynamic birefringence signals were calculated. The electrical resistance of the nerve (and thus the current applied) was measured during stimulation by recording the voltage across a 10 Ω resistor in series with the nerve.

The XPS closely followed both a positive and a negative applied voltage, with a small delay, as shown in Figure 3-10A. Rising and falling time constants of 14 ms and 19 ms were found for the positive stimulus XPS. These are significantly longer than the values reported by Cohen et al. (Cohen et al. 1971) for individual squid giant axons (~68 μs). If we assume the system can be represented as an RC circuit with a resistance of around 1 kΩ (as measured in previous experiments), this provides a tissue capacitance of around 0.5 $\mu$F/cm$^2$, which is actually comparable to the membrane capacitance of individual axons (Foster & Schwan 1989), indicating that the two values may be correlated.

The WLN XPS was found to be approximately linear with applied voltages in the range -2 V to +2 V (Figure 3-10B), consistent with a linear electro-optic effect, or Pockels effect. This is in contrast to data reported for individual squid giant axons (Cohen et al. 1971), which demonstrated a Kerr-like effect, or quadratic electro-optic effect, when measured at the membrane. The stimulation currents corresponding to this voltage

range were 0.1 mA to 5 mA (not shown), depending on the applied voltage amplitude and varying with the impedance of each particular nerve. Beyond approximately the range of -2 V to +2 V, the applied-field effect saturates for both polarities.

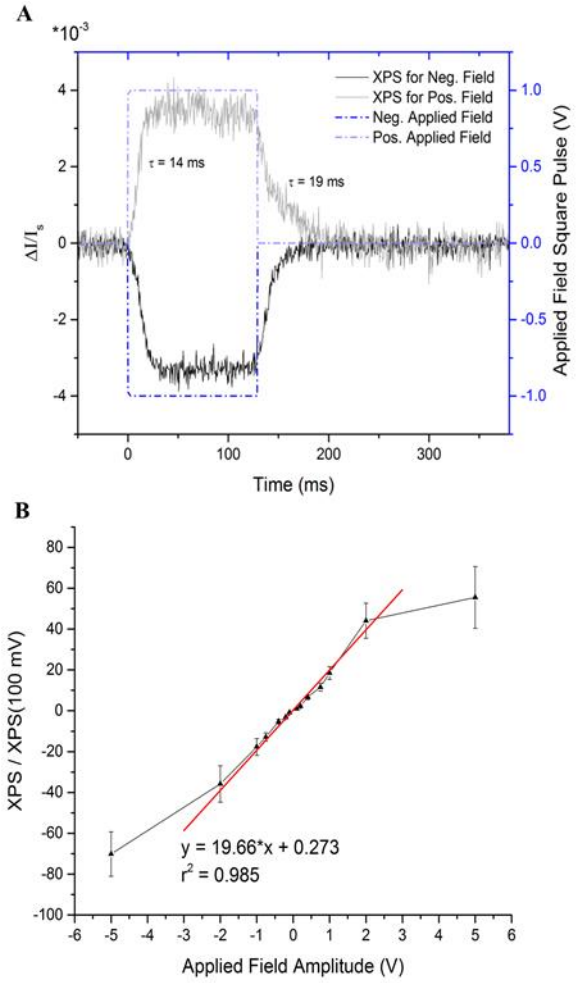


Figure 3-10. XPS relationship to applied electric field magnitudes (Badreddine et al. 2015).

A) Example of a stimulus used in the experiment. 1V and -1V, 128-ms square voltage pulses were applied to nerve, and the XPS and stimulus voltage traces are shown together. The birefringence signal closely follows the applied electric field, with time constants of 14 ms rising and 19 ms falling. B) The XPS demonstrates a positive, linear relationship (shown here with a linear fit) to the amplitude of an applied voltage stimulus in the range -2 V to 2 V (data is normalized to the XPS at 100 mV for each nerve, n=5).

The signal saturates beyond that range, possibly related to limitations in the availability of the physiological structures causing changes in birefringence.

### *3.4.7. Sinusoidal electric fields*

Sinusoidal voltages were applied directly to the nerve, across the stimulation wells, using an analog voltage output from the NI DAQ card. This application of electric fields (proportional to applied voltage) to a small longitudinal section of the nerve, can provide information regarding the response timing and adaptive nature of the whole nerve bundle to changing electric stimuli. To investigate this, sinusoidal field voltages of 100 200, and 400 mV were applied over sinusoidal frequencies of 1, 2, 3, 5 and 10 cycles per second, for a duration of 500 ms. Figure 3-11 shows the nerve's XPS response to voltage frequencies of 1, 2, and 10 cycles/s at 200 mV (A–C, respectively). The XPS leads the timing of the applied field at 1 cycle/s, but lags at higher frequencies, which is indicative of a capacitive phenomenon most likely involving the non-axonal tissue structures (in combination with the axonal ones). Figure 3-11D shows the XPS response to the amplitudes of the sinusoidal fields for a given frequency (in this case 1 cycle/s), which depicts a linear response, in agreement with results from section 3.4.6 on non-oscillating applied fields.

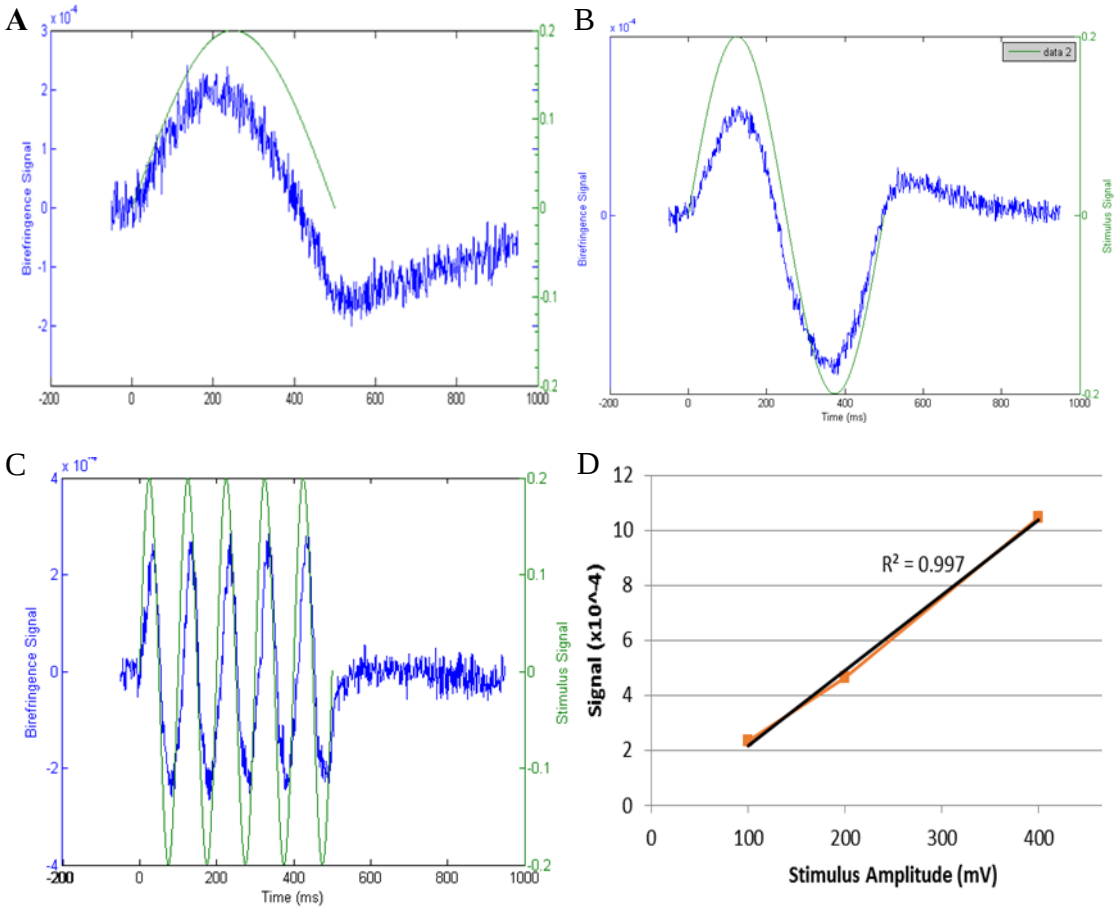


Figure 3-11. XPS in response to sinusoidal applied fields.

A) An applied voltage of 200 mV at 0.5 cycles/0.5s for 500 ms shows a slow, leading XPS. B) At 1 cycle/0.5s, the XPS begins to lag and reduce in relative amplitude. C) At 5 cycles/s, the trend is more obvious. D) A linear electro-optic response is observed in response to the applied sinusoidal voltage amplitudes at a given frequency (here, 1 cycle/s).

Figure 3-12 (top) shows the XPS response to sinusoidal frequency of the applied field normalized to the initial value. The trend appears to be logarithmic with base 2, with the amplitude of the XPS decreasing with increasing frequency of the applied field. The XPS decreases by around 25% as the stimulus frequency is doubled. This reflects an inverse power law that is ubiquitous in biology and indicates a dampening oscillator

response that is expected for a system resembling an RC circuit.

Figure 3-12 (bottom) shows the phase lags between the heights of the peaks of the XPS and sinusoidal fields, normalized to the initial value. The same logarithmic trend as above is found with increasing frequency until a point of 'saturation' is reached, where the lag of the XPS reaches the falling part of the applied field sinusoid (see Figure 3-11C). Additionally, the maximum of the XPS peak initially leads the applied field peak at 0.5 cycles/s, but begins to lag as the frequency increases to 1 cycle/s. The point of transition varies between nerves, but always occurs in that range. These behaviors are indicative of a capacitive phenomenon and of the nerve's adaptive response.

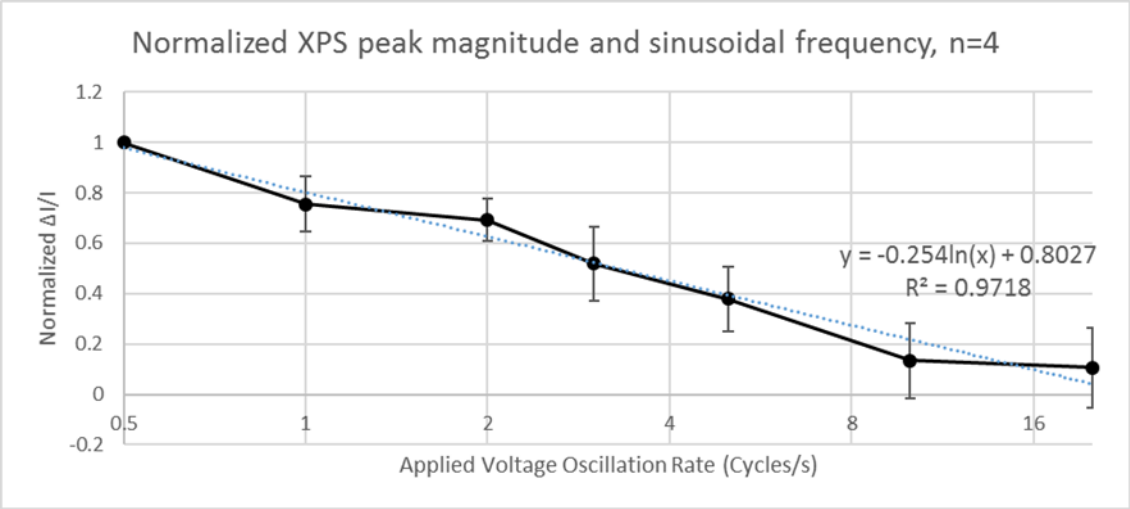


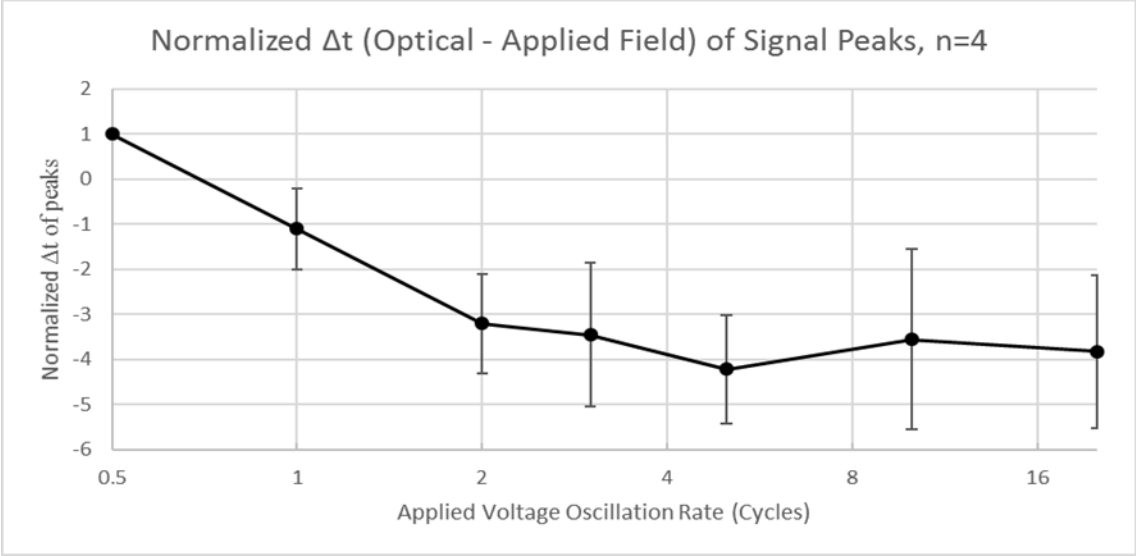


Figure 3-12. XPS magnitude and phase lag relative to sinusoidal frequency

*Top:* The normalized XPS decreases logarithmically with base 2 in response to the applied voltage frequency. *Bottom:* The phase difference between the peak of the applied field and the XPS shows the same logarithmic trend until a point of 'saturation.'

### *3.4.8. Discussion*

The results of these experiments further characterize the dynamic birefringence signal associated with both action potential activity and applied electric fields in complex, heterogeneous nerves, and also with nerves having narrow axon size

distributions, while providing new information regarding the temporal characteristics of the spreading and gradual recovery of the crossed-polarized signal. The data suggest that the gradual recovery of the XPS cannot be explained only by the spread of arrival times of individual axonal action potentials (APs). Further, the temporal dynamics of axon swelling are also incompatible with the slow recovery(Tasaki & Byrne 1993; Yao et al. 2003). We hypothesize that a direct electric-field-induced change in polarizability due to capacitive-like charging and discharging from traveling APs in adjacent tissues is responsible for this portion of the XPS.

Previous researchers have hypothesized that the shape of the XPS (fast onset and slow recovery) in heterogeneous nerves such as the lobster walking leg nerve (WLN) is due in large part to the range of AP propagation velocities for the wide range of axonal diameters (and thus a wide range of arrival times) (Carter et al. 2004; Schei et al. 2008; Cohen et al. 1970; Yao et al. 2003). They did not, moreover, report distinct phases in the XPS, possibly due to a lack of detector sensitivity or noise from electronics. Our nerve chamber and detection electronics enabled a more comprehensive investigation of XPS as a function of distance from the stimulation site with higher sensitivity. We found, in both the computational model and experimental measurements, that the (initial) slow onset, the (second phase) fast onset, and the (initial) fast recovery, are consistent with the velocity-distribution hypothesis, but that the distribution of AP velocities for the constituent axons cannot explain the long tail of the gradual recovery phase. The gradual recovery phase is similar (lasting 100s of ms), regardless of distance of the measurement point from the stimulus site.

One possible explanation for the gradual recovery is a slow release of ions/charges that are stored at nearby tissue structures in response to a perturbation by the fluctuating electric field of the adjacent traveling APs. The electric fields of these stored charges would act to increase, or decrease, the optical polarizability (hence refractive index) of the nerve tissue. This would be consistent with, but alternative to the hypothesis previously proposed that considers the change in birefringence to be caused by a reorientation of sodium channels and other membrane-bound protein channels (Landowne 1985; Cohen 1973) or membrane phospholipid dipoles (Cohen 1973). The fact that the nerve electrical recording (shown in Figure 3-8) exhibits a gradual recovery with temporal duration similar to that of the XPS (despite the relative polarity change) may be significant and is consistent with our hypothesis. Additionally, the electrical recording indicates that the vast majority of APs have subsided by the time the gradual recovery phase begins.

The computational model was able to reproduce both onset phases, as well as the initial fast recovery phase, demonstrating results similar to observations by Carter et al. (Carter et al. 2004), indicating that these phases of the XPS are consistent with the arrival times of the medium and giant axon groups of the WLN. The other size group is composed of small axons (~0.1–5 μm) (Darin De Lorenzo et al. 1968), which spread out in time more significantly due to the large relative range of diameters within that size group. The model serves as additional evidence that indeed the observed gradual recovery is not related to AP activity. No adjustment of any of the parameters, neither those treated as variables nor the physiologically defined values, could fully reproduce

the empirical XPS traces. Adding a gradual capacitive decay to the overall waveform produced by the model would be the simplest way to reproduce the empirical gradual recovery phase.

Studies involving ‘dead’ nerves are not commonly performed, since they do not directly pertain to neuronal activity. In this study, the use of AP-inactive (as verified by an absence of activity in the electrical recording) but structurally sound nerves (as verified by both a similar static birefringence to that in the live nerve and through microscopic inspection) informs on the effects of electric field fluctuations in the entire tissue. APs originate in the negative stimulus well (evident by the earlier arrival time of the peak), which is consistent with a depolarization of the axonal membranes, causing a decrease in birefringence. The XPS for a ‘stimulated’ dead nerve is qualitatively similar in shape to that of a live nerve (in Figure 3-9). The primary difference is that, in live nerves, generated APs cause a reversal of polarity of the XPS at the positive stimulus well, and also shift the gradual recovery downward compared to dead nerves. Furthermore, AP activity (in the live nerve) in the WLN always is accompanied by a decrease in birefringence. The application of a 10-mA stimulus pulse in a live nerve produced an upward shift in the section of the XPS trace associated with APs, followed by a gradual recovery from above baseline. This is consistent with a superposition in the XPS of both the arriving APs, and a capacitive charging that can induce a hyperpolarizing effect of axonal membranes, thus increasing the effective birefringence (the XPS). A more obvious capacitive-like discharging effect in both stimulus wells is evident in the XPS traces for the dead nerve in response to both the 1-mA and 10-mA

stimuli. This provides evidence that not only is there a polarity dependence in the XPS, but that the tissue exhibits a charging and discharging phenomenon induced by a stimulus field, whose magnitude directly corresponds to the magnitude of the XPS.

The experiment for data in Figure 3-10 for our fluid-coupled nerve stimulation, resembles an experiment presented by Cohen et al. (Cohen et al. 1971), obtained by voltage-clamping individual squid giant axons. This demonstrates that hyperpolarization and depolarization were accompanied reliably by direct electric-field-induced changes in birefringence in the membrane. In our experiments, the whole WLN nerves (bundles of axons with a complex organization of surrounding tissues) were 'clamped' to specific voltages over a ~2 – 4 mm distance, and we found that the time constants for the whole nerve tissue are significantly slower (>2 orders of magnitude difference) than those observed in individual squid giant axons. The increased delay in whole nerves is likely caused by the influence of inter-axonal effects and non-axonal tissue structures. Furthermore, as shown in Figure 3-10B, the nerves exhibit a linear electro-optic effect. Given that Cohen et al. (Cohen et al. 1971) demonstrated that individual axons exhibit a quadratic Kerr effect at the membrane, this indicates that other tissue structures and mechanisms may be involved in the response of whole nerves to fluctuating electric fields, possibly, in part, related to a bulk tissue capacitance (Butson & McIntyre 2005; Foster & Schwan 1989). The XPS associated with these fluctuations, from both applied fields and APs, also may be related to a coupling effect of adjacent axons, similar to ephaptic coupling (MacVicar & Hochman 1991; Debanne et al. 2011). Non-synaptic, or ephaptic, transmission between adjacent axons may be responsible for smoothing the

peaks of XPS traces, which otherwise might be expected to have sharper features due to large gaps between the size-groups of the lobster WLN axon distribution. Furthermore, tissue capacitance and dielectric property changes are known to occur and have been studied associated with phenomena such as cortical spreading depression in migraines (Dreier 2011). These observations imply that the gradual recovery from changes in birefringence associated with AP activity may occur in axon-adjacent tissue structures and are associated with a bulk tissue capacitance.

The aforementioned electrical phenomena were further explored by applying sinusoidal voltages across the nerves. We found the same linear trend to AC sinusoids as we did with the previous experiment using DC-like square pulses, which is further evidence that the nerve behaves like a Pockels cell, in following a linear electro-optic response. That the same relationship is observed in the chosen range of frequencies lends weight to any information gained from this experiment. We again observed that the tissue has a capacitive behavior and that it is detected in the XPS. The transition in the phase of the maximum of the XPS peak, from leading to lagging the applied field peak, demonstrates an adaptive response of the nerve to the voltage. The nerve tends to oppose the applied field, with the XPS beginning to return to baseline before the field is even at a maximum. This may be related to pumps that are actively shuttling ions around to readjust the membrane potentials throughout the tissues, which have been severely disrupted from the applied fields. Regardless of the phenomenon, this indicates that the birefringence response is almost certainly following the application of the field, and

changes in birefringence are following changes in the electric fields, such as those induced by propagating action potentials.

### 3.5. Aim 1 Conclusions

The noise surrounding the XPS is significant and often requires averaging to be detected. Digital filtering is also often a requirement. While previous research has yielded signals which are relatively good and even work in single-pass trials (Carter et al. 2004), obtaining these is infrequent and further improvements to the electronics and optics setups are necessary to improve the SNR enough for the XPS to be useful in more advanced applications. The improvements to the methods and SNR in part 1 made obtaining the XPS easier and provided data which looked cleaner than that presented in the past.

The results of the experiments in part 2 utilized some of the developments from part 1 to further characterize the dynamic birefringence signal associated with both action potential activity and applied electric fields in complex, heterogeneous nerves, while providing new information regarding the temporal characteristics of the spreading and gradual recovery of the XPS. Our data collectively serves as a strong indication that there is a capacitive-charging-like effect directly inducing a gradual recovery of the XPS to baseline, and also causing a smoothing of the XPS trace. Determining specifically which physiological structures may be behind these changes in birefringence involving the peak of the XPS and the gradual recovery is left for future investigation.

# CHAPTER 4. AIM 2: "REAL-TIME" TRACKING OF THE BIREFRINGENCE SIGNAL

## 4.1. Introduction

Dynamic changes in birefringence, measured as the "crossed-polarized signal" (XPS), arise when axonal membranes exhibit a rapid momentary change, typically a decrease, in birefringence as a consequence of the dynamic changes in local electric fields due to propagating APs (Cohen et al. 1969). Limited two-dimensional spatial resolution of the XPS (over a small length and width of the nerve) has been obtained using a charge-coupled device (CCD), although a low signal-to-noise ratio (SNR) allowed only the strongest peak of the signal to be reliably detected after significant binning and filtering, and the imaging was an average of multiple stimuli, and thus not real-time (Schei et al. 2008). These were, nonetheless, steps in the right direction toward real-time imaging of AP propagation using changes in birefringence.

Here, we utilize the information on improved instrumentation and SNR from Aim 1, and develop a new benchtop system that enables reliable tracking of the propagation of APs in real-time using the XPS measured in the lobster walking leg nerve (WLN). The rapid onset and gradual recovery times of the XPS signal that were discussed in section 3.4.2 are also demonstrated here, both in stimulus-averaged data and for a single stimulus period, depicting real-time imaging. First, the system is used to study averaged stimuli in the manner described in section 3.2; then, single stimulus periods are extracted from the data and filtered, revealing the 'real-time' XPS. Data for a

faster stimulus rate is also provided. These results establish a basis upon which this technique could be further developed for neuroscience research or eventual clinical use.

## 4.2. General methods

A diagram depicting the experimental imaging and electronic setup is shown in Figure 4-1. All optical elements are housed in 30 mm cage mounts (Thorlabs, Inc.). Illumination is provided by a 625-nm high-power LED (Thorlabs, Inc. M625L3) driven by an LED driver (Thorlabs, Inc. T-Cube) with variable output current control. Light from the LED is approximately collimated using a spherical plano-convex lens, and then focused to a line at the nerve by a cylindrical lens. Light from the nerve is then imaged (using a second spherical lens) onto the central ~40 pixels of a fast 64-element Si-photodiode (PD) array with a built-in low-noise amplifier (Hamamatsu S8865-64). The PD array is combined with a dedicated driver circuit (Hamamatsu C9118). Our custom-designed chamber housing the nerve was described previously (Badreddine et al. 2015). The chamber is positioned such that a ~2 cm length of the nerve in the electrically-grounded central well is illuminated. The incident light is polarized by a linear polarizer ($LP_i$) (Edmund Optics #47-316), and the light transmitted through the nerve is analyzed by another linear polarizer ($LP_a$), oriented 90º to $LP_i$. The pair of crossed polarizers are placed with their optic axes at ±45° relative to the length of the nerve, providing the maximum birefringence signal (Cohen et al. 1970).

The driver circuit for the PD array is operated by the reset signal (RES), which establishes the line rate, and a clock signal (CLK), both of which are controlled by a pulse generator (PG) (Berkeley Nucleonics, BNC 555). The circuit outputs the video

signal (VID), as well as two TTL signals ─ when each individual pixel is being read out (TRIG), and at the end of each line scan (EOS). Two National Instruments (NI) data acquisition (DAQ) cards are used. The first (NI DAQ 1) is a 16-bit, 1 MS/s analog-to-digital converter (National Instruments, PXI-6120) that uses the TRIG signal as a sample clock, to coincide with a data point recorded for the analog input for the VID signal. The second (NI DAQ 2) is used to time the electrical stimulation of the nerve and downstream recording. The electrical signals and data collection are controlled by LabVIEW (NI), as shown in Figure 4-2. Queue functions are used to ensure that the start of the data vector recorded is indeed pixel #1 in the array, rather than an arbitrary pixel. This is necessary because the readout is continuous.

An algorithm, written in Matlab© (Mathworks), is used to parse the VID data into a matrix containing each pixel's data in a column, to facilitate data analysis. The static birefringence, $I_s$, is measured as light transmitted through the crossed polarizers with no stimulation of APs, and is evaluated as the mean of a short time-span of the pixel readout prior to administering a stimulus pulse. The optical signal is expressed as the relative dynamic birefringence $\Delta I/I_s$, which is henceforth referred to as the crossed-polarized signal (XPS). To obtain this signal, we subtract $I_s$ from the pixel readout for each stimulus period and divide the resulting difference by $I_s$. Except for the real-time measurements described below, $\Delta I/I_s$ is calculated by first averaging the traces generated by 100 consecutive stimuli, and then applying a 5-point moving average filter, and a computational bandpass filter between 0.1 Hz and 1000 Hz to the averaged traces, which do not remove relevant signal information, since an AP spike occurs in around 1–2 ms.

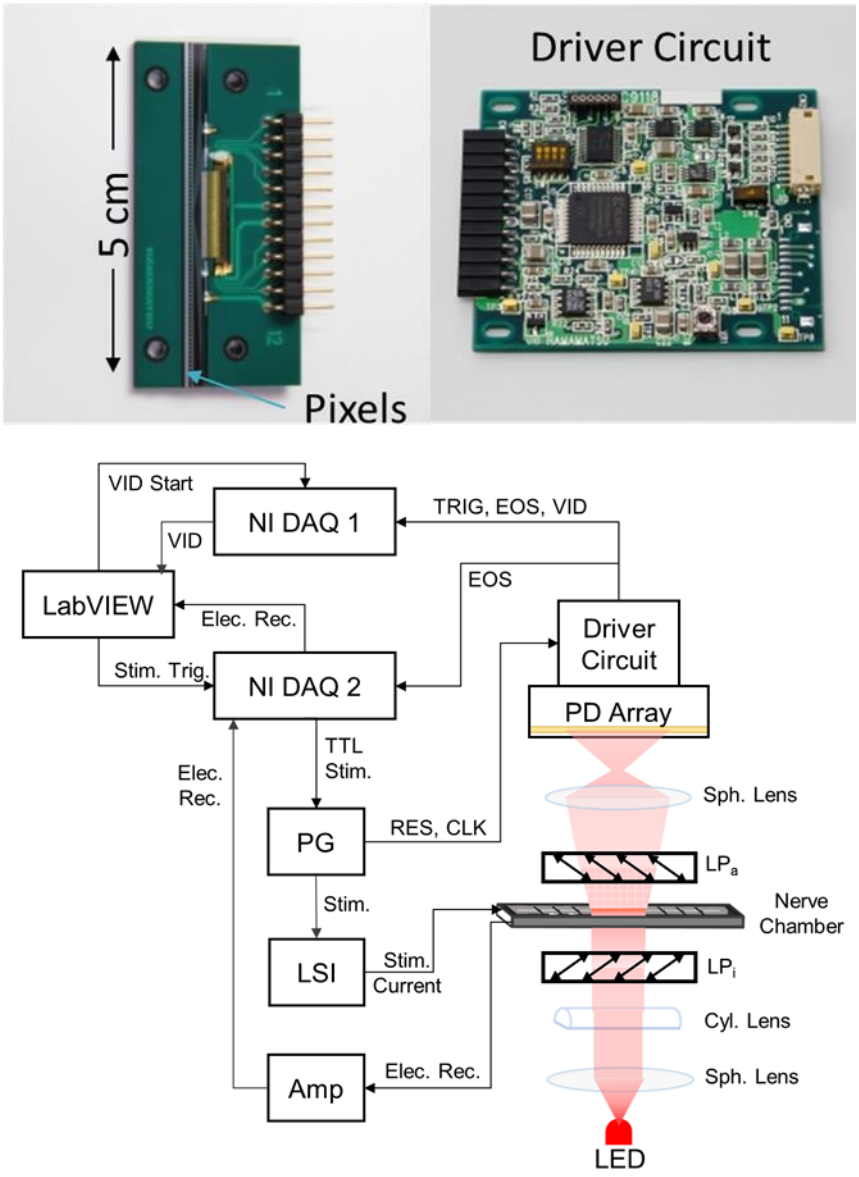


Figure 4-1. The setup for AP tracking using a linear array (Badreddine et al. 2016).

*Top:* The PD linear array and driver circuit are shown. Images taken from http://www.hamamatsu.com/us/en/index.html. *Bottom:* On the right is the optical setup used for line-illumination and imaging of nerve birefringence onto a photodiode (PD) array, and using two crossed linear polarizers ($LP_i$ and $LP_a$). A pulse generator (PG) sends reset (RES) and clock (CLK) signals to the driver circuit to run the PD array. The driver circuit outputs the analog video (VID) signal, as well as TTL pulses for both the end-of-scan (EOS) and each pixel's individual readout (TRIG). The first data acquisition card (National Instruments, NI DAQ 1) synchronizes the analog input for the video signal with

a sample clock from TRIG, so that no pixel readout is skipped. The second data acquisition card (NI DAQ 2) relays a stimulation pulse (Stim. Trig.) to the PG, which outputs a 1-ms, 10-V pulse to the linear stimulus isolator (LSI), which sends a 1-ms, 1-mA stimulus to one end of the nerve; it also records the electrical signal from the other end of the nerve, passed through a bandpass amplifier (Amp). The electronics and data collection are controlled by LabVIEW.

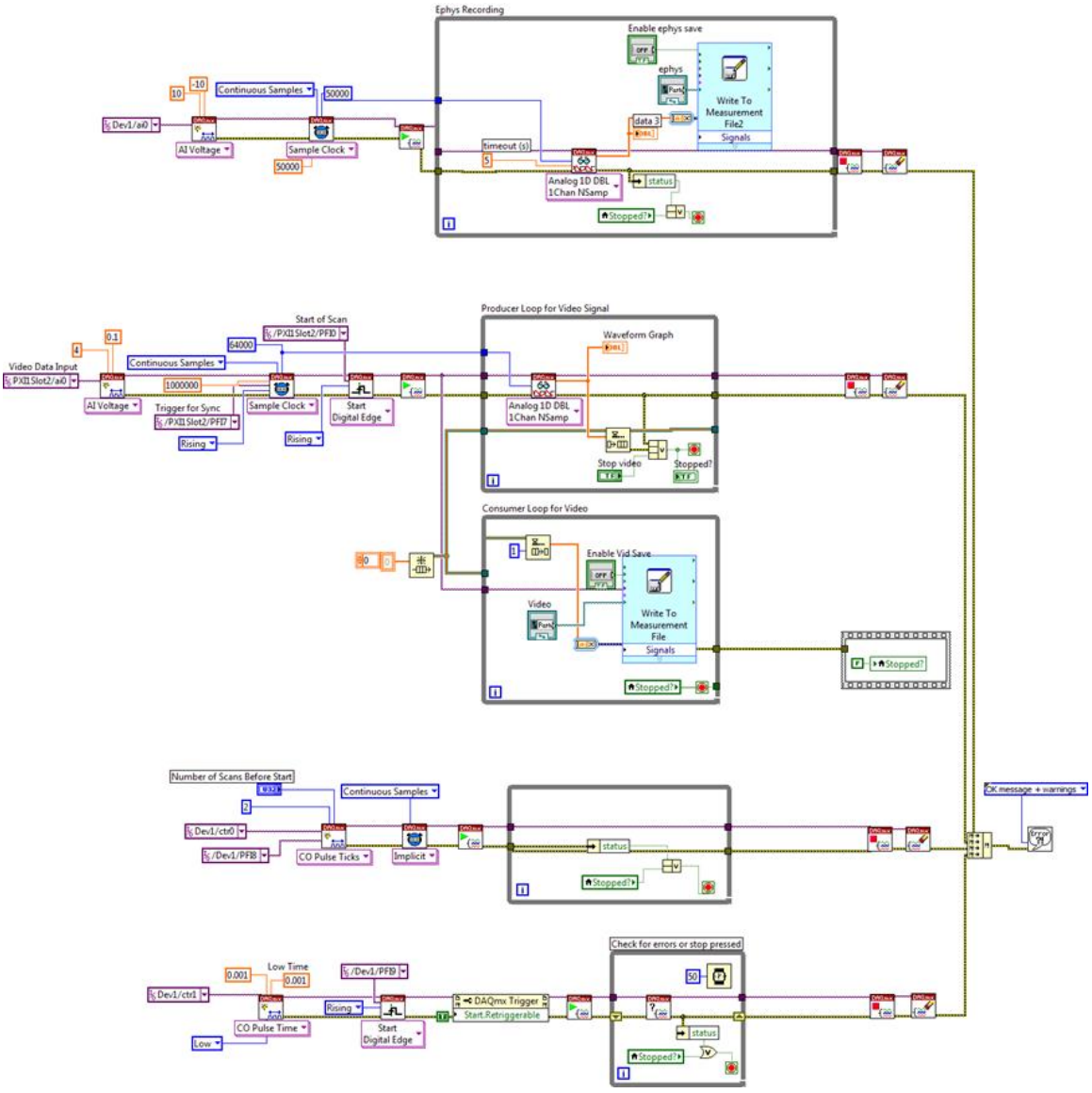


Figure 4-2. Example of the Labview software for stimulating and recording.

Shown is the software in Labview used to stimulate and record the signals detected by the array of photodiode elements. Recursive loops are used to maintain a continuous

operation and queues are used to organize the data into 64-pixel groups, ensuring that the start of a data vector is pixel #1.

A walking leg nerve (WLN) from one of the four rostral-most walking legs of a lobster, *Homarus americanus,* is removed using the Furusawa pull-out method (Furusawa 1929) and placed into the nerve chamber. The nerve is immersed in *Homarus* Ringer's solution (Evans et al. 1976; Derby & Atema 1982).The nerve has ~1000 axons, whose diameters vary from ~0.1 to 100 μm in three groupings of small (0.1–5 μm), medium (20–30 μm) and "giant" (50–100 μm) axons (Derby & Atema 1982; Young 1936; Darin De Lorenzo et al. 1968). The nerve is stimulated at 2 Hz (unless otherwise noted) using a 1-ms, 1-mA (single-polarity) square pulse from a linear stimulus isolator (WPI, Inc. A395R-C), initiated by another channel of the PG that is gated by a trigger from NI DAQ 2 using a count of the EOS signal. A stimulus current of 1 mA was found to recruit a near-maximum number of axons, while not overstimulating, as discussed previously (Badreddine et al. 2015). The PD array is operated near the maximum rate, ~7000 lines/sec, so for a typical stimulus period, this provides ~3500 frames per stimulus. The electrical recording is amplified by a factor of 1000 using a low-noise bandpass amplifier (AMP) (A-M Systems, 3000) with a bandpass filter between 0.1 Hz and 10 kHz. In Figure 4-3, an early depiction of the setup is shown (top), and a later improved version is also shown (bottom). For the purposes of this chapter, data from one particular nerve is shown, but multiple nerves provided good data.


Figure 4-3. Images showing the setup.

*Top:* Original setup with a custom detector housing and most electronics used. *Bottom:* An improved version of the setup is shown and removes many lose cables which previously allowed some EMI to be picked up in the video readout.

### 4.3. Repeated-stimulus-averaged tracking

The distribution of light over the linear array for a nerve is shown in Figure 4-4. The light output from an LED is roughly Gaussian, so, despite using a cylindrical lens, the distribution of light along a focused line is still Gaussian. Any attempt to provide uniform illumination would reduce the intensity substantially. Furthermore, the nerve does not induce a uniform static birefringence across its length. This complicates any

attempt to maximize light over the length of the nerve to improve SNR. By careful handling and positioning of the nerve, it is possible to get a fairly uniform distribution, but for these purposes, the distribution of light shown in Figure 4-4 is acceptable.

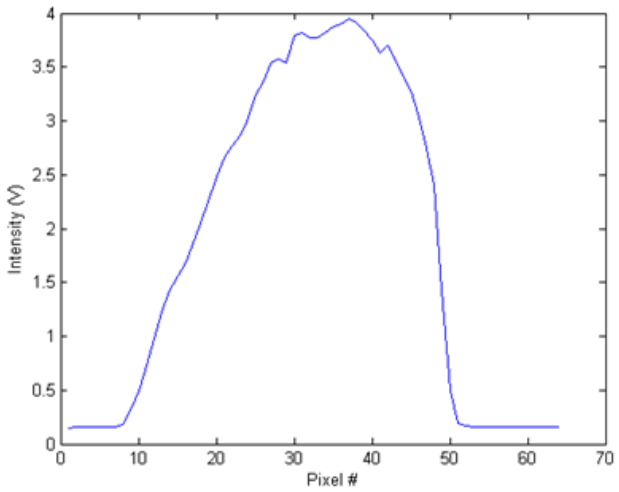


Figure 4-4. Distribution of light intensity on photodiode array.
The photodiode array is a line of pixels about 5 cm long, and the light distributed across those 64 pixels is shown for the given nerve. The peak is at pixel #38.

In Figure 4-5, depictions of the average of one hundred stimulus periods of the propagating crossed-polarized signal (XPS) associated with action-potential activity are shown for times of 10, 12, 17, 32, 70 and 200 ms post-stimulus. Each bar represents the XPS for a single pixel, and the signal propagates from left to right, over a ~2 cm length of the nerve. The reduction in peak magnitude, increasing temporal width of the peak, and gradual recovery, reported previously (Badreddine et al. 2015), are seen here as well. The traveling signal is reliably tracked.

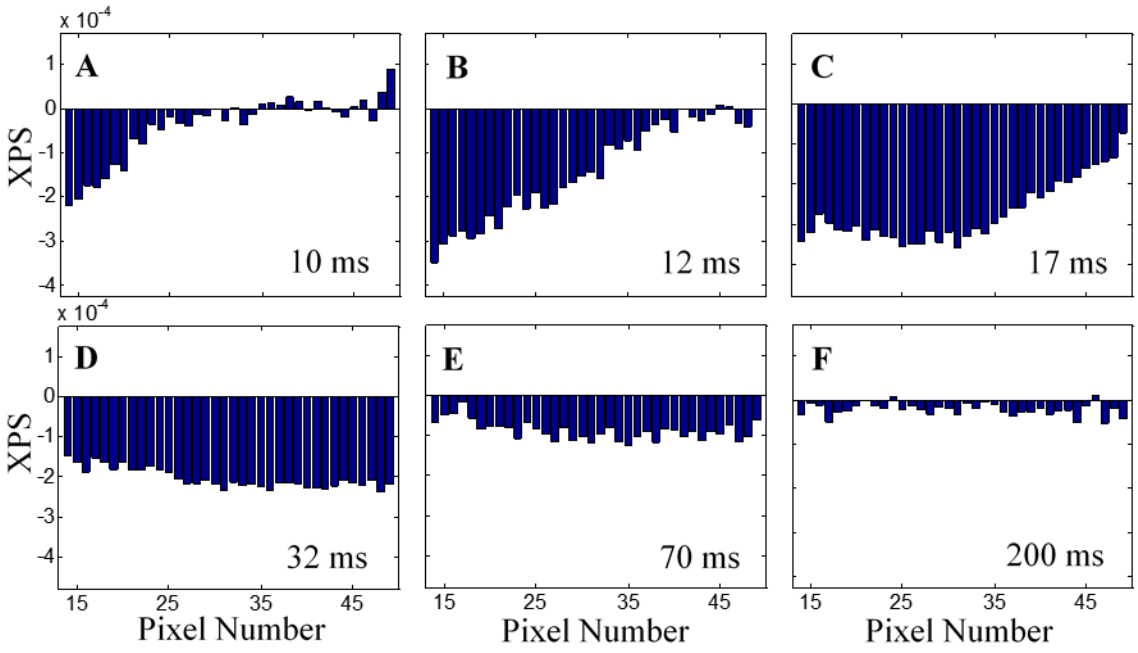


Figure 4-5. The propagating AP averaged over multiple stimuli (Badreddine et al. 2016). The average of the XPS over 100 stimulus periods as a function of pixel number are shown at post-stimulus times of 10, 12 17, 32, 70 and 200 ms (A–F, respectively). The onset of the peak resulting from the compound action potential is evident (A–C) and the gradual recovery to baseline (D–F) lasts hundreds of milliseconds. The propagating peak of the XPS takes ~20 ms to travel a distance of ~2 cm.

### 4.4. Extracted "real-time" single stimulus tracking

To demonstrate 'real-time' XPS detection, the frames associated with a single stimulus period, from among the hundred were averaged. One such example is shown in Figure 4-6. We found that a computational 4$^{th}$-order Butterworth filter with cutoff frequencies at 0.3 Hz and 100 Hz provides smooth data without significantly removing relevant information. In this sample, the central ~1.5 cm of the nerve length is depicted. The 'real-time' traveling XPS from left to right is observed, and the same temporal characteristics of the onset and recovery of the peak are evident, as were seen in the averaged data.

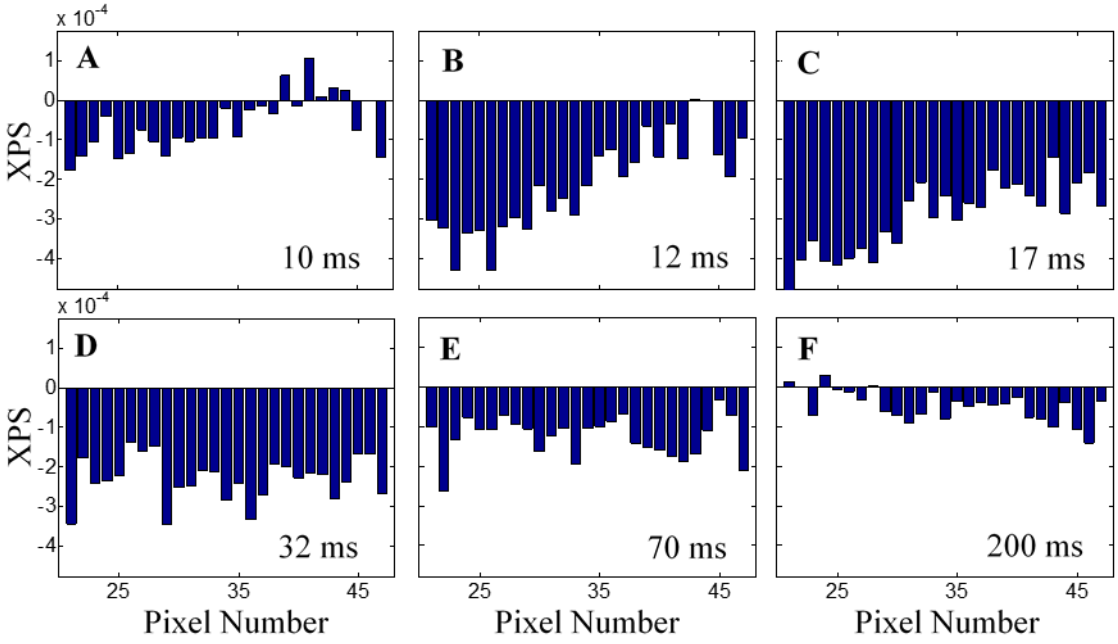


Figure 4-6. Real-time tracking of APs (Badreddine et al. 2016).

A random, single stimulus period is extracted from the data, and a smoothing computational filter with cutoff frequencies of 0.3 Hz and 100 Hz is applied. These data provide a demonstration of a 'real-time', fast tracking of the XPS signal. Timepoints of 10, 12, 17, 32, 70 and 200 ms are shown (A–D, respectively). The onset and recovery of the peak can be reliably detected without averaging. This effectively demonstrates real-time tracking.

Figure 4-7 shows XPS traces for specific pixels correlating to two distances from the stimulus site along the length of the nerve. These are shown for both the average of one hundred stimulus periods (A and B) and for a single stimulus (C and D). The delayed onset and broadened width of the peak as a function of distance is evident when comparing data from the location at 18 mm with that from 6 mm, for both averaged and 'real-time' data. The noise is on the order of $10^{-4}$ relative to the baseline intensity in a non-averaged, single trial after filtering, and the signal is consistently $>10^{-4}$. With one hundred averages, the noise is reduced by a factor of ~10.

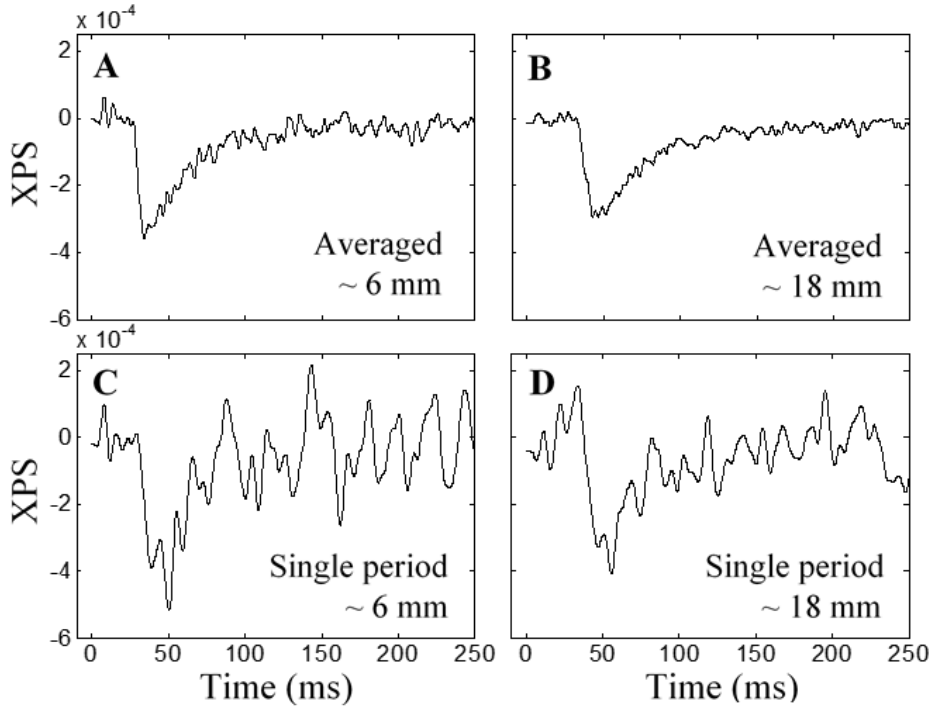


Figure 4-7. Traces of the XPS for averaged and real-time data (Badreddine et al. 2016). Traces of the XPS are shown for 100 stimulus-averaged periods at ~6 mm (A) and ~12 mm (B) from the stimulus. Extracted single stimulus periods (C and D) are also shown. The broadening of the peak as a function of distance and the gradual recovery to baseline are evident in both averaged and real-time signals.

### 4.5. Varying stimulus frequency and amplitude

When the repetition rate of stimulation is increased from 2 Hz to 14 Hz, the shape of the XPS peak is altered, as shown in Figure 4-8. The magnitude and slopes are decreased. As shown in Figure 4-9, for post-stimulus times 15, 20, 35 and 65 ms, the temporal width decreases substantially and the recovery is forced to occur at a much faster rate. Whereas the gradual recovery lasts hundreds of milliseconds under less-frequent stimulation, when stimulated at a faster rate, the recovery lasts only until the next stimulation event. XPS peak features were different most likely as a result of axons unable to repeatedly fire from a single stimulus, and the nerve adapting so that only a

smaller group of axons fired, causing the features (relating to the arrival of axon size groups) to appear more pronounced than for the slower stimulation rate (Figure 4-7).

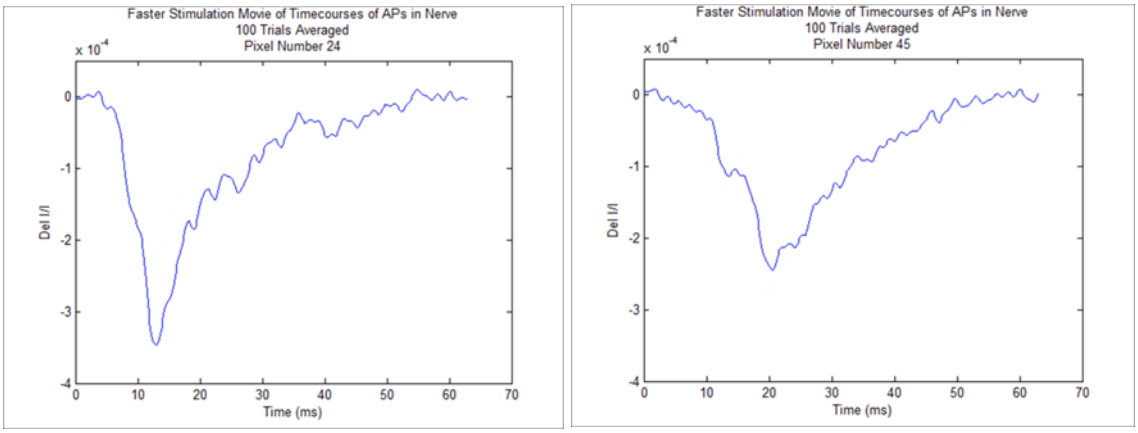


Figure 4-8. Traces for the faster stimulus.

The traces shown for a pixel closer to the stimulus (left) and further (right) demonstrate that the magnitude and slopes of the XPS decrease as a function of distance, but gradual recovery is forced to return to baseline before the start of the next stimulus.

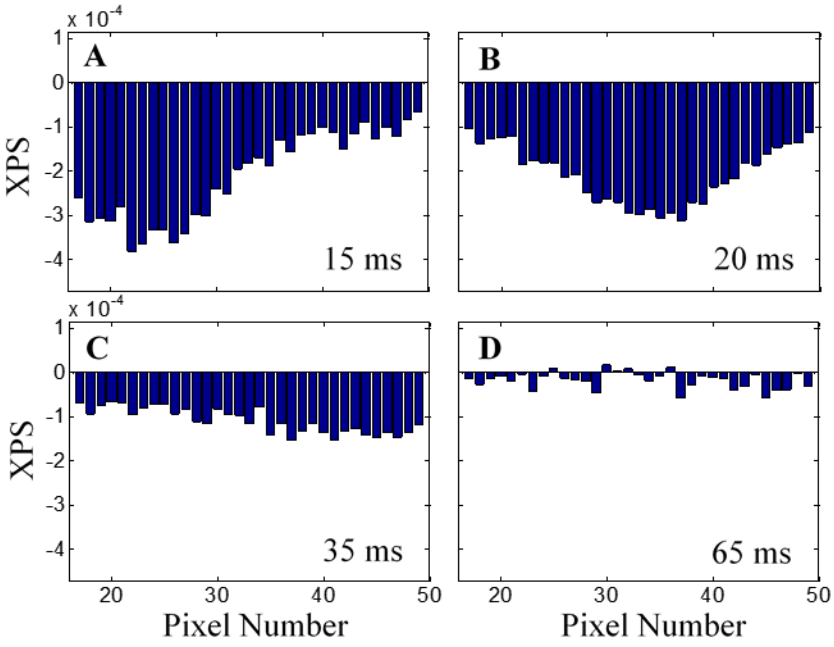


Figure 4-9. Sample frames from movie of XPS at faster stimulation rate (Badreddine et al. 2016).

XPS data for averaged stimulus periods at a faster stimulation rate of 14Hz are shown for post-stimulus times of 15, 20, 35 and 65 ms. The recovery of the peak occurs at a faster rate and the gradual recovery is forced to return to baseline just before the initiation of the next stimulus pulse. The temporal width of the peak is reduced.

## 4.6. Discussion

Fast, noninvasive methods for real-time imaging of neuronal signals are lacking. Changes in birefringence of nerve tissues occur as a result of the direct polarization changes induced by local electric fields fluctuating with propagating action potentials (APs) (Cohen et al. 1970; Foust & Rector 2007; Badreddine et al. 2015). As discussed in our previous work (Badreddine et al. 2015), other intrinsic tissue phenomena, such as cellular swelling, may marginally contribute to these changes in birefringence, but the effects are largely overshadowed by those caused by changes in the electric field. The measurement of changes in birefringence is adequate for fast, real-time detection in

structured neuronal tissues such as peripheral nerves. In this study, we demonstrate real-time imaging based on changes in birefringence along a lobster walking leg nerve (WLN).

In previous work, we described the temporal characteristics of the crossed-polarized signal (XPS) for the WLN in detail, finding that the evolution of the XPS peak and gradual recovery to baseline can be explained by the spreading compound APs, a bulk tissue capacitance, and ephaptic coupling between adjacent axons (Badreddine et al. 2015). Here, using a fast linear photodiode array, we observe the same phenomena in real time, including the temporal broadening of the peak as a function of distance from the stimulus location (and the concomitant loss of peak height), and a gradual recovery to baseline. This serves as a verification that our new setup and detection method are capable of capturing in a "movie" much of the same detail as our previous method, which captured the temporal history at a single point using a single photodiode. Repeated stimulus averaging is helpful to reduce the relative shot noise and increase the SNR, but would be a limitation when attempting to study spontaneous neuronal activity *in vivo*. In analyzing a single stimulus period, we show that real-time tracking of the XPS is feasible.

With the type of instrumentation employed in this set of experiments, the compound AP electrical recording is measured between two electrodes across a ~4 mm length of nerve, through Ringer's solution. When subjected to a faster stimulation rate, the nerve exhibits an adaptation, which is evident in the electrical recording seen in section 3.4.4. The shapes of the XPS traces in Figure 4-8 further demonstrate this adaptation, as the width and magnitude of the peak decreases with a faster stimulation

rate (note the time scales). The XPS appears to recover just before a subsequent stimulation event, which is due in part to a DC drift in the pixel readout caused by the rate of stimulation being higher than the recovery time of the XPS. Despite the rapidity of the fast stimulation rate, the signal is still cleanly tracked and the characteristic phases of the XPS in the WLN are evident (shown in Figure 4-9).

## 4.7. Aim 2 Conclusions

Our setup successfully demonstrated the feasibility of tracking propagating compound APs in a peripheral nerve using the XPS. This is supported by the detection of all features of the XPS in any decently illuminated PD as well as in the movies of the tracked XPS across all PDs. By extracting a single stimulus interval, we demonstrated that this setup can be used to investigate real-time signal propagation. These data demonstrate the potential for real-time imaging of AP propagation using changes in birefringence.

# CHAPTER 5. AIM 3: MYELINATED TISSUE AND THE BIREFRINGENCE SIGNAL

## 5.1. Introduction

Changes in birefringence associated with action potentials have never been detected in myelinated neuronal tissue, such as mammalian nerves, but static birefringence has been studied, as far as it relates to the underlying structural anatomy (as discussed in section 2.4.2). More information about birefringence in myelinated tissue is needed to better understand these signals and make predictions on what to expect when the dynamic birefringence signal (the XPS) is observed. One expectation is that it would appear like the XPS from crustacean nerves, but with a different magnitude and significantly faster timecourse, from the faster propagation of APs due to myelination. Since the dynamic birefringence signal (the XPS) has not yet been seen, we could estimate what form the signal might take, based on the structural properties of the myelinated tissue, and the expected effects of myelination.

Myelination is a series of wrapped cellular membranes from Schwann cells (glial cells) that encase large sections of axons in a peripheral nerve and are maintained by myelin membrane proteins (Lodish et al. 2000). Myelin blocks the flow of ions across the membrane, which restricts changes in membrane voltage from APs to just the nodes of Ranvier. Since changes in birefringence have been shown to be caused by fluctuations in the electric field, we might expect the signal to originate only at the nodes. However, there may be contributions from the flow of ions that occurs along either side of the myelin-encased sections of the membranes as well.

With the aim of finding and studying the XPS in myelinated neuronal tissues, we first attempted to study these signals in simple mammalian hippocampal neuron cultures. We then moved on to more complex mouse brain slices, hoping that the XPS could be detected in an anisotropic pathway. The next samples we attempted were from songbird laryngeal nerves, which are fairly simple in structure, and highly anisotropic (as all peripheral nerves are). Finally, we concluded our studies using mouse sciatic nerves, which yielded an interesting new XPS, and provided a path toward utilizing changes in birefringence as a means to study mammalian AP activity intrinsically.

## 5.2. Mammalian hippocampal neuron cultures

### *5.2.1. Methods*

Hippocampal cell cultures were provided by the Han Lab at Boston University. The cultures were made by extracting hippocampal cells from live mice and growing them on glass plates in petri dishes in artificial cerebrospinal fluid (aCSF). Neurons in the culture were not patterned and were allowed to grow intrinsically. Axons in these cultures often overlapped substantially, as can be seen in the differential interference contrast (DIC) microscopy image in Figure 5-1. DIC reveals boundary information cleanly, and the image reveals that axons are projecting in random directions. This lack of anisotropy presents a challenge when attempting to image changes in birefringence, which works best with oriented media.

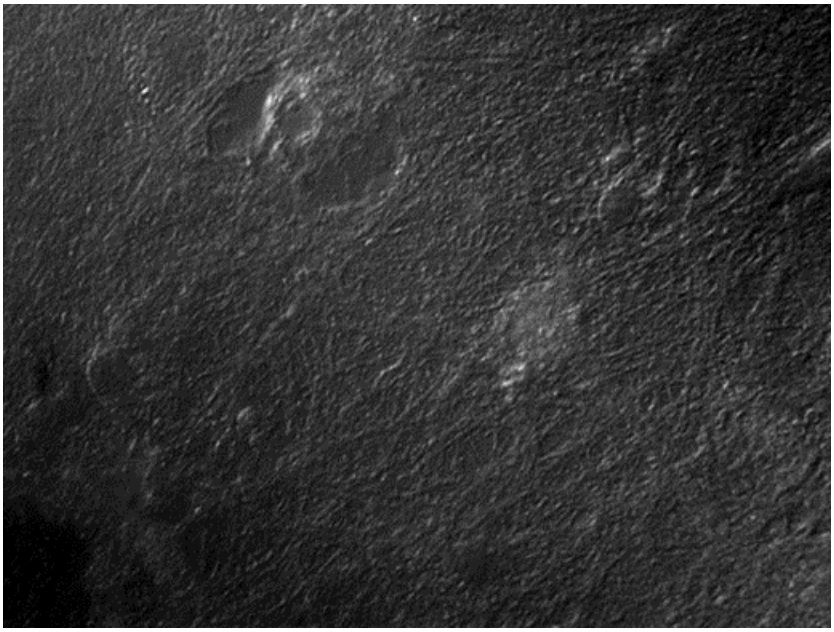

Figure 5-1. DIC image of axonal projections in hippocampal culture.
The DIC image reveals randomly oriented axonal projections. The lack of an overall anisotropy will reduce the static birefringence and make detecting signal changes difficult.

The imaging experiments were performed using optics and electronics similar to that described in section 3.2. Modifications had to be made for electrical stimulation and recording. Exposed tips of silver wires were placed against the neurons in various points along the cultures. Typically, the stimulus electrodes were placed on either end to elicite as many APs as possible. One recording electrode was placed somewhere in the middle, and the other serves as a reference in the medium. To verify that birefringence was a dominant signal in this setup, the pair of polarizers were rotated together from 0° to 180° in increments of 15°, in the manner described previously (Cohen et al. 1968; Yao et al. 2005). For the XPS, the same standard stimulus parameters were attempted with averaging as in section 3.2.

### *5.2.2. Results and analysis*

The neuron cultures are monolayers with overlapping axons, and this allows a significant amount of light to pass through without interacting with the tissue. The cultures placed in the setup (Figure 5-2 on the left) appeared to scatter light in random directions significantly, and only a small amount of light made it through the crossed polarizers. Nonetheless, rotating the polarizer pair revealed that there is a not-insignificant amount of birefringence, or at least polarization-dependence, as shown in Figure 5-2 on the right. If randomly polarizing scattering of light was the only signal present, this angle dependence would not be observed. The peaks and valleys of the polarization angle dependence of the signal were random depending on the sample, due to the random nature in which the axons are distributed.

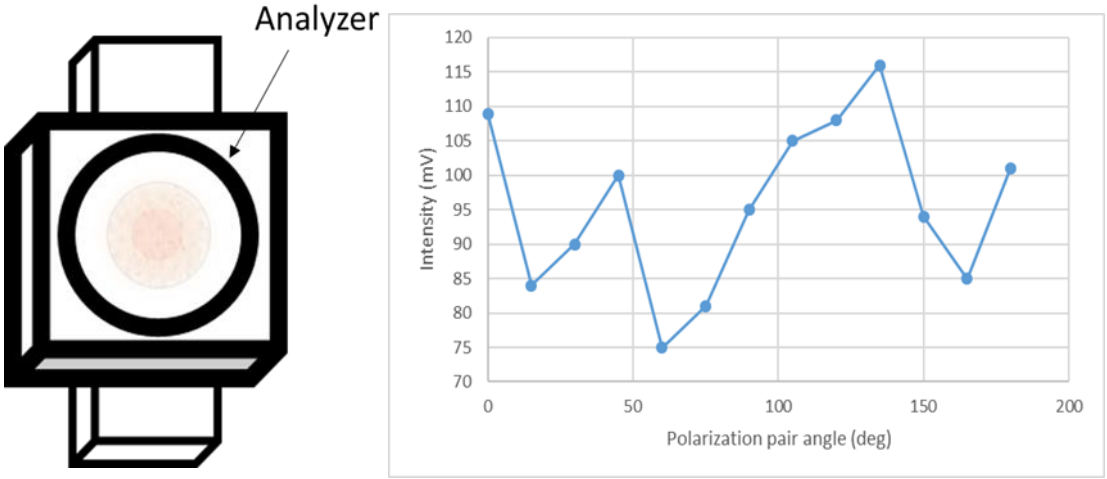


Figure 5-2. Static optical signal of neuron culture.
*Left:* Depiction of the neuron culture in between crossed linear polarizers under red light.
*Right:* Light intensity reaching the photodiode

When stimulated, the electrical recordings showed no significant activity. Noise

from the stimulus electrodes was picked up and may have masked any activity from the neurons themselves. More likely, due to the difficulty in stimulating neurons extracellularly in this manner, the neurons were not firing APs significantly. The stimulus current was bypassing the neurons, being short-circuited by the solution. The XPS also did not show any detectable signal. If this is to be a useful imaging method for monolayer *in vitro* activity, cultures would have to be grown to form clear overarching anisotropies, and the stimulation and recording methods improved.

## 5.3. Mouse brain slices

### *5.3.1. Specific background and methods*

To perform a study of XPS in brain slices, an area of the brain slice with a high degree of anisotropy was chosen. The entorhinal-hippocampal area was chosen due to its structured pathway of connectivity (Canto et al. 2008), as discussed in section 2.4.3, and shown in Figure 5-3. If stimulated at the DG, the Schaffer collaterals projecting from the DG to CA3 to CA1, will allow AP activity in the area between the CA3 and CA 1 neurons (an area with a relatively large degree of anisotropy) to be detected.

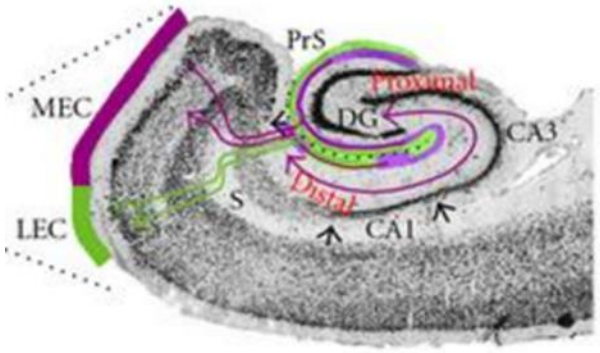


Figure 5-3. Image of the mouse brain slice and entorhinal-hippocampal area of interest (Canto et al. 2008).

A depiction of a mouse brain slice with relevant areas of interest is shown. Those areas involve the Schaffer collaterals projecting from DG to CA3 to CA1 neurons.

Brain slices from mice were provided by the Hasselmo Lab at Boston University. A standard protocol was followed in extracted the slices (Mathis, D. M., Furman, J. L., Norris et al. 2011). Briefly, mice were anesthetized with isoflurane, and, after extracting the brain, a vibratome is used to slice the brain into ~350 $\mu$m slices. The slices are bathed in oxygenated aCSF immediately and allowed to rest for 1 hr before beginning the experiments. Then a slice was placed into a custom chamber.

To image the XPS, a new chamber needed to be developed. The simplest solution was to 3D print the chamber using acrylonitrile butadiene styrene (ABS) plastic in a 3D printer provided by the Boston University Engineering Product Innovation Center (EPIC). Standard protocols were followed. The designs were created in Autodesk Inventor© (Autodesk, Inc.). Images of a printed chamber and iterative designs are shown in Figure 5-4, along with a depiction of the mount (also 3D printed) used to hold the chamber in our optical setup.

The first chamber design (Figure 5-4A) included a glass coverslip to reduce the effects of fluid surface vibrations, and both input and output wells to enable a flow of oxygenated aCSF. Later designs modified the chamber to improve flow of aCSF, and to ease manipulation of stimulation and recording electrodes around the glass, using sloped sides and a thinner coverslip mount. The center of the well is left transparent with a glass microscope slide epoxied to the bottom for measuring the XPS. In the most recent design, a tube is attached to the outlet and the fluid is released into a waste beaker. Gravity perfusion is used to feed the inlet through another tube.

Brain slices require constant perfusion or their neurons begin to quickly die. The fluid needs to be a species-specific aCSF, and it has to be kept oxygenated at the source. Here, it was provided by the Hasselmo Lab. The temperature of the solution needs to be maintained at near-physiologically relevant temperatures to encourage formation of APs. This was done by housing the solution in a custom-built, temperature-controlled system, shown in Figure 5-5. A 200 W, 120 V silicone rubber heat pad (SRW040-100, Heating Elements Plus.com) was affixed to a stainless steel canister using thermal adhesive, and then insulated using a layer of foam encased in aluminum. A proportional–integral–derivative (PID) controller and a relay were used to control the temperature through the heating pad leads, to regulate aCSF inside the canister at around 37°C with a small hysteresis.

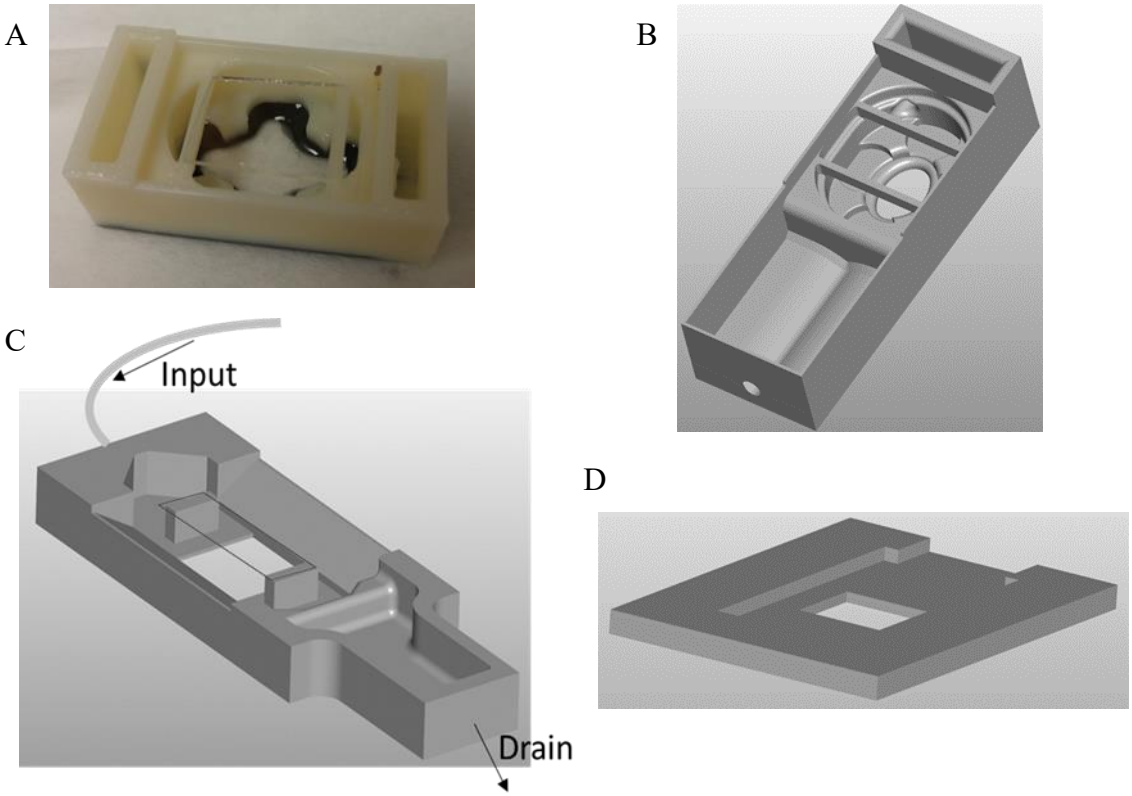


Figure 5-4. Iterative brain slice chamber designs.

A) The first 3D printed chamber contained an aCSF input well, an output well, and a central imaging well with a glass coverslip. B) A modified design changed the output reservoir to be more effective. C) Manipulating the electrodes proved difficult, so the chamber design was modified to have sloped sides to make maneuvering around the glass easier. D) The mount for the chambers was also 3D printed.

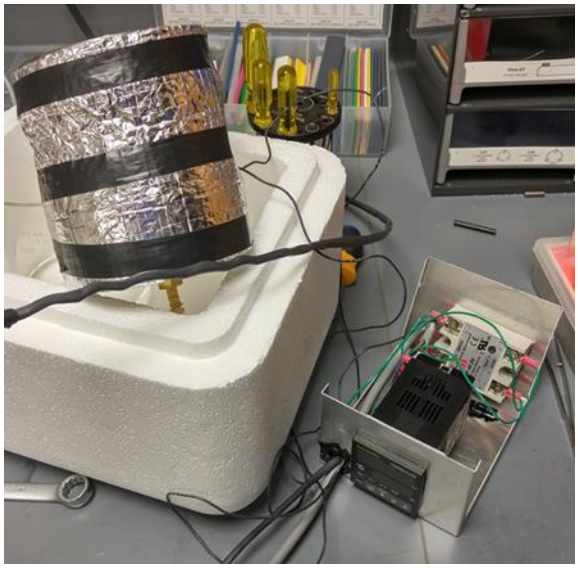

Figure 5-5. Temperature controller for aCSF.

A PID controller was used to control the temperature of the aCSF inside a stainless steel canister by heating a silicone rubber pad wrapped in insulation.

New techniques were needed for stimulating and recording the electrical signals from brain slices in this setup. The stimulation electrodes were free silver leads encased in a soft plastic, with just the tips of the leads making electrical contact with the aCSF. The positive lead was placed in the area near the DG, and the negative lead was placed in the aCSF away the slice, to serve as a reference. Recording electrodes were housed inside a custom suction electrode, following a previous design (Johnson et al. 2007). The optical signal was recorded in the area in the middle of the pathway between the CA3 and CA 1 neurons. A diagram depicting this setup and a microscopy image of the area of illumination are shown in Figure 5-6.

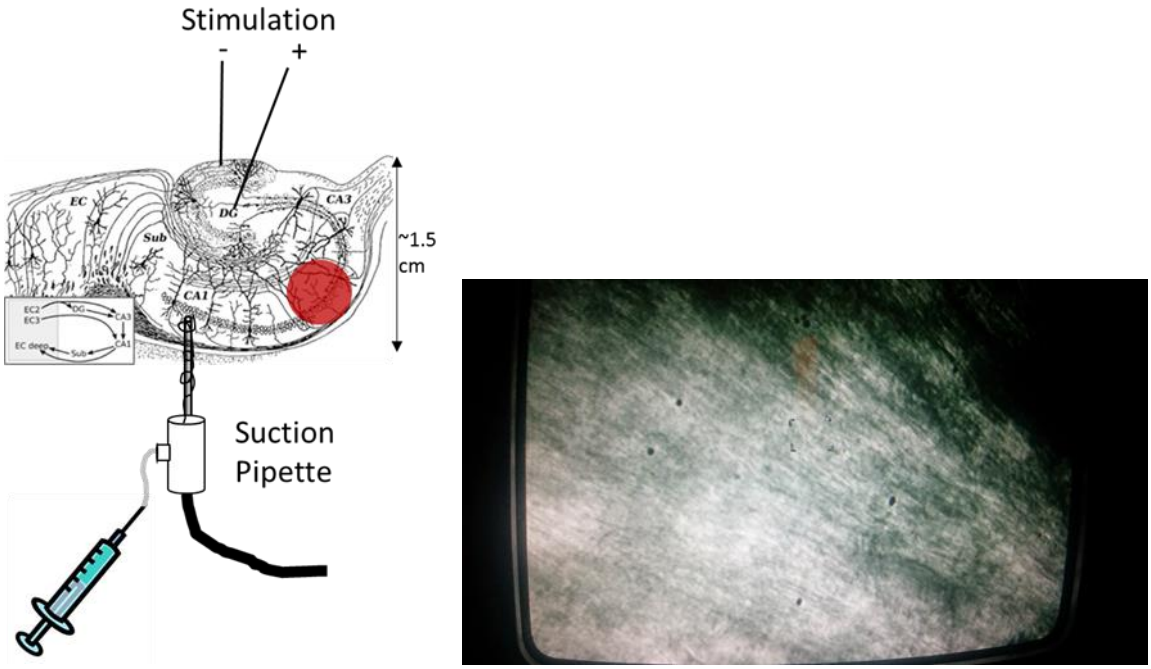


Figure 5-6. Brain slice positioning of the electrodes and light.

*Left:* Stimulation electrodes, silver electrodes with only the tips exposed, were placed in the dentate gyrus and outside the slice as a reference. The recording suction electrodes were placed downstream in the area near the CA1 neurons. The optical signal was recorded in the pathway in the middle. Basis of image taken from https://en.wikipedia.org/wiki/Hippocampus_anatomy#/media/File:CajalHippocampus_(modified).png. *Right:* Microscope image of the area of interest, showing an overall anisotropy.

### *5.3.2. Results and analysis*

An electrical recording of a brain slice as measured through the suction electrodes is shown in Figure 5-7. A stimulus period of 1 s was used here, and stimulus artifacts can be seen. A capacitance charging effect is also evident, and here it is caused by the electrodes being non-isolated, as the positive and negative electrodes are coupled by the aCSF. Periodic noise spikes were often picked up by the recording electrodes and likely were introduced by the stimulation electronics, such as the LSI. Nonetheless, when

magnified, postsynaptic potentials are evident, as shown in Figure 5-7 on the right. This served as a verification that at least some AP activity was present downstream. However, where that activity is specifically occurring, and to what degree, remained unknown.

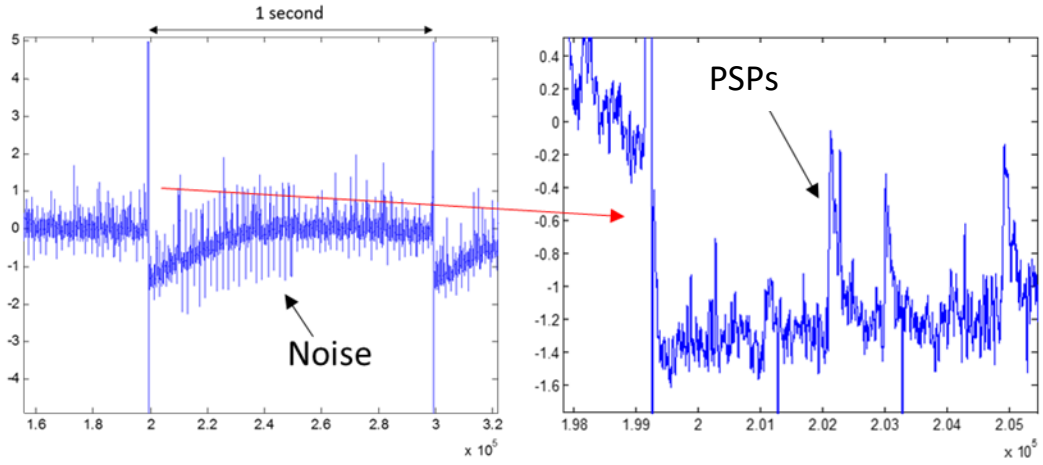


Figure 5-7. Electrical recording of the brain slice.

*Left:* With a stimulus period of 1 s, the electrical recording shows an artifact, followed by a capacitance effect from the electrodes, followed by random spikes. *Right:* When some of the spikes are magnified, postsynaptic potentials are evident, which indicate the presence of post-synaptic potential (PSP) activity, which indicative of APs.

To verify that the light transmitted to the photodiode was birefringence, rather than scattering or other phenomena, the pair of polarizers were rotated from 0° to 90°, and the data is shown in Figure 5-8. In the particular area illuminated, peaks occurred at 0° and 60° for this particular slice in the setup. The minima were not near zero, as in the case of peripheral nerves, because of the complexity of the tissue. Even when a very small area is magnified, the structures have some isotropy (Witter & Moser 2006). Regardless, there appeared to be enough static birefringence in this area to detect the XPS.

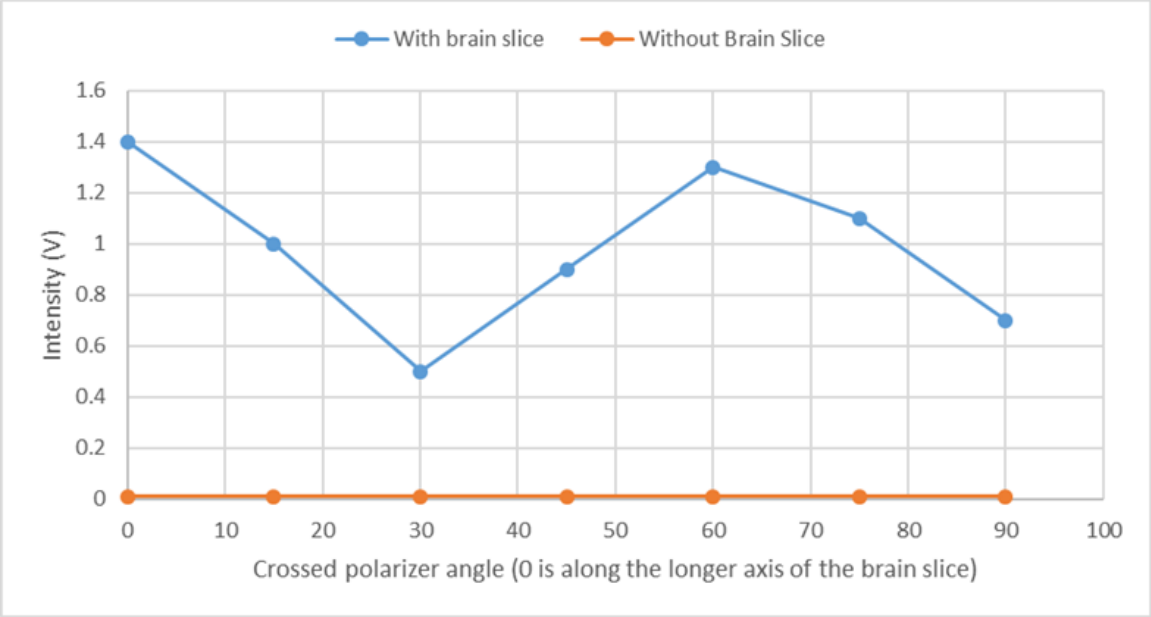


Figure 5-8. Birefringence verification for brain slice.

The pair of crossed polarizers was rotated from 0° to 90°, relative to the longer axis of the brain slice, and clear peaks and valleys were observed, indicating that there is a significant birefringence in this area.

Unfortunately, attempts to detect the XPS were not successful. No signal could be detected from the noise. Attempts to move the illumination area closer to the stimulus site also did not produce a signal. One possible cause of this could be due to a limited contrast between the isotropic and anisotropic contributions to the light reaching the photodiode, limiting the magnitude of the compound signal. Another likely possibility is that many neurons in the pathway died before an adequate amount of signal could reach the XPS recording site. This is made complicated by a lack of expertise in our lab in handling these tissues.

## 5.4. Songbird laryngeal nerve

### *5.4.1. Methods*

Extraction of the Zebra Finch laryngeal nerve was performed by the Gardner Lab at Boston University. A maximal segment of trachea was removed in birds which were to be sacrificed due to age or post-breeding. A depiction of the extracted segment is shown in Figure 5-9. The segments were typically around 1.5 cm long and up to 5 mm in diameter. A pair of laryngeal nerves are embedded in connective tissues on opposite sides of the trachea. Each nerve is usually about 80 $\mu$m in diameter and as long as the trachea segment. The nerves are removed by carefully tearing apart the connective tissue encasing them. Closed tweezers are inserted under the nerves, moving along their length, as the tweezers are expanded to remove the nerve from the trachea.


Figure 5-9. Songbird trachea segment.
*Left:* Maximal extracted segments of the trachea were around 1.5 cm long and contained a pair of laryngeal nerves on opposite sides. The nerves were carefully removed from their connective tissues. *Right:* Chicken trachea is shown for reference. Image taken from http://www.poultrymed.ir/atlases/avian-atlas/search/examfinding/585.html.

The laryngeal nerves are too small to fit into the original nerve chamber used in Aims 1 and 2. A new, smaller chamber was needed. A design was made in Autodesk Inventor with an opening for the nerve that is around 1.5 cm in length, and about 7 mm

wide, and is shown in Figure 5-10. The design has a pair of stimulation wells on one end and recording wells on the other. The central well and the closest stimulation and recording wells are transparent for measuring the XPS. Channels are left open for the placement of silver electrodes. The chamber was printed by the Gardner Lab using a Form 1+ printer (formlabs) with black ABS. 18 gauge silver wires were epoxied in the channels to be used as electrodes. A connector was soldered onto the silver leads and encapsulated in hot glue.

Thin suture wires were used to attempt to ligate the exposed ends of the nerves. Nerves were stimulated and recorded using the methodology described in section 3.2.

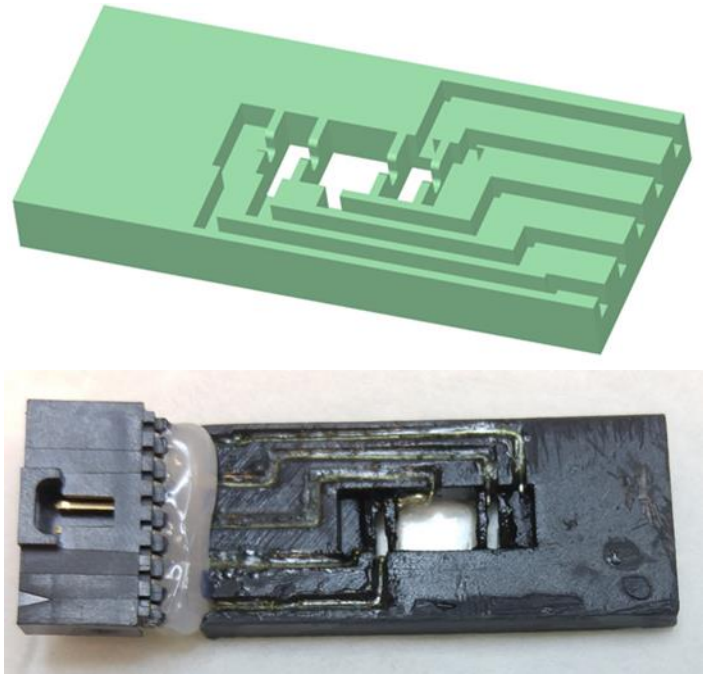

Figure 5-10. Smaller nerve chamber.

*Top:* Shown is the Autodesk Inventor design of a smaller nerve chamber. The area for the nerve is about 1.5 cm long. As with the previous nerve chamber design, fluid-coupled extracellular stimulation and recording is used. *Bottom:* An image of the 3D printed chamber and attached connector is shown. Silver wires are epoxied into printed channels.

### *5.4.2. Results and analysis*

The nerves were small and difficult to carefully extract without damaging the axons. This led to complications in placing them in the chamber and keeping them alive. Ligation of exposed nerve ends is normally important to prevent the coupling of intracellular and extracellular fluids. Ligation of nerves this size proved difficult, and often was not successful. Electrical recordings never showed AP activity, and the XPS was never detected. The intensity of light due to static birefringence was low, often < 100 mV, due to two primary problems: 1) the tissue being fairly small, and 2) the difficulty of focusing light from an LED onto an area that small, while magnifying only the light passing through the nerve onto the detector without losing too much light.

## 5.5. Mouse sciatic nerve

### *5.5.1. Extraction methods*

Mice for extracting the sciatic nerves were provided by the Hasselmo Lab, as discussed in section 5.3. The mice were already sacrificed for brain slice experiments. We extracted maximum lengths (up to 2 cm) of the sciatic nerves from these decapitated mice using a modification of a procedure established by Bala et al. (Bala et al. 2014), and shown in Figure 5-11. Briefly, the modified procedure is as follows. The skin is first removed. An incision is then made at the base of the tail, and the tail is then pulled away from the legs, exposing the sciatic nerves projecting from the lumbar vertebrae. The bilateral nerves are traced along each leg, cutting away surrounding muscle and connective tissues, down to the area near the knee, where the nerves bifurcate. The nerves are then ligated on either end (modification) using suture wire, and cut at the knee and

spine. The extracted nerves, examples of which are shown in Figure 5-12 (unligated), were then bathed in aCSF. The use of a mammalian Ringer's solution was investigated, but aCSF was readily available and proved to work without any issues, so it was used instead, and a species-specific Ringer's solution formula was difficult to find.

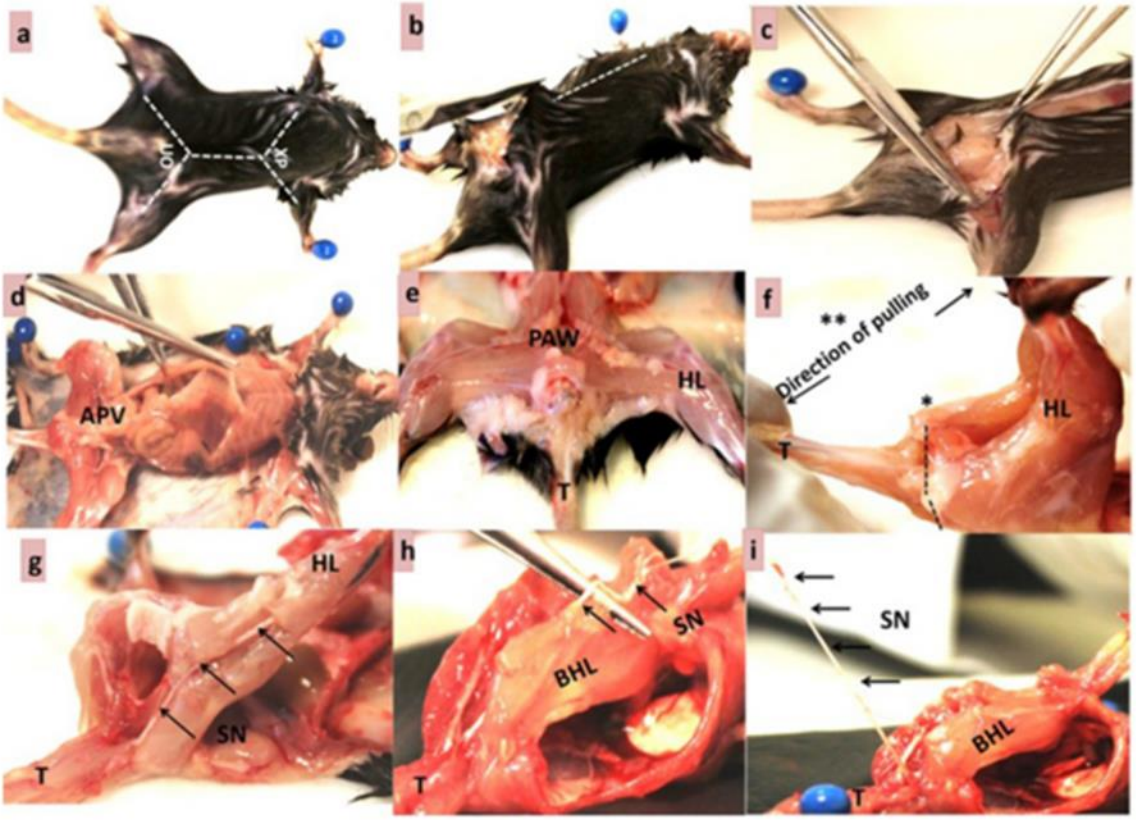


Figure 5-11. Extraction procedure for maximum length of sciatic nerves (Bala et al. 2014).

The procedure followed for extracting mouse sciatic nerves allowed for obtaining a maximum length of up to 2 cm. The skin is first removed, then an incision is made on the tail, which is pulled away from the legs to expose the nerves. The nerves are dissected from the surrounding tissues. The nerves are then ligated and removed, then bathed in aCSF.

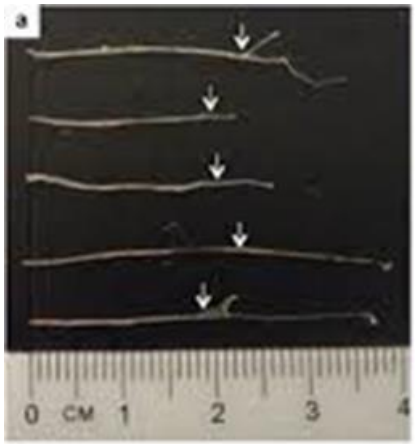


Figure 5-12. Extracted sciatic nerves at maximum length (Bala et al. 2014).

The nerves extracted using the aforementioned procedure are of a maximum length. They are up to 1 mm in diameter, which is a good size for ease of handling and optical imaging methods.

*5.5.2. Investigating static birefringence under a modified DIC microscope*

Birefringence of myelination has been investigated, as discussed in section 2.4.2, but the focus largely was on the anatomical aspects of myelination, rather than its contribution to a functional signal. The studies also did not explore the birefringence of whole myelinated nerves, as they are fairly complex. To get a better understanding of the static birefringence of myelinated peripheral nerves, we used a DIC microscope (Olympus IX81) in the Boston University Micro/Nano Imaging Facility to image birefringence at high resolution. To do this, the DIC microscope was modified by removing the Nomarski prisms and phase contrast plate, effectively turning the scope into a simple polarization microscope. A nerve was placed into a No. 0, 35 mm glass bottom dish (Mattek), with the nerve either whole or splayed out to image smaller groups of individual axons for clarity. The dish was placed on the microscope mount, which could be rotated. Images were taken on a 16 bit scientific CMOS camera. Anna Slatterty, a

student as part of the Undergraduate Summer Program in Neuroscience, aided in these experiments, and collected many of the images.

A whole nerve fiber was imaged and rotated from 45° to 90° relative to the polarizers. The birefringence of the nerve, shown in Figure 5-13, was significant. At 45°, light intensity was up to three orders of magnitude greater than at 90°. The highly anisotropic structure of the nerve bundle and boundaries of the axons were visible, as well as some connective tissues at the edge of the bundle. This served as verification that we were imaging static birefringence, and that individual axons were able to be visualized.

A

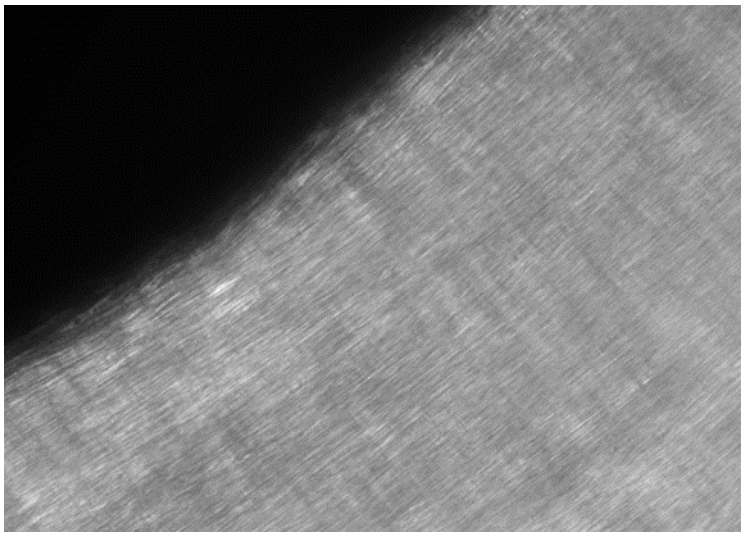

B

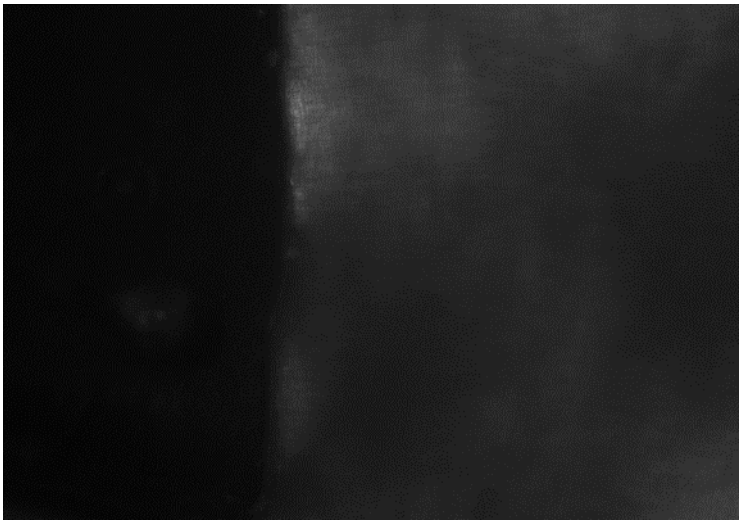

Figure 5-13. Birefringence of whole nerve.

A) The whole nerve is positioned at 45°. The axon boundaries are evident, despite a high number overlapping in the image. The nerve's anisotropic structure is obvious. B) The nerve is at 90°, coinciding with incident polarizer, with significantly reduced intensity.

The angle dependence of the birefringence was made more evident when a crooked section of the bundle was imaged, as in Figure 5-14. At 135°, the light intensity and edge contrast was high, but as the nerve curved to 0°, the intensity dropped off significantly, and then increased again as the nerve passed 0° and moved toward 45°.

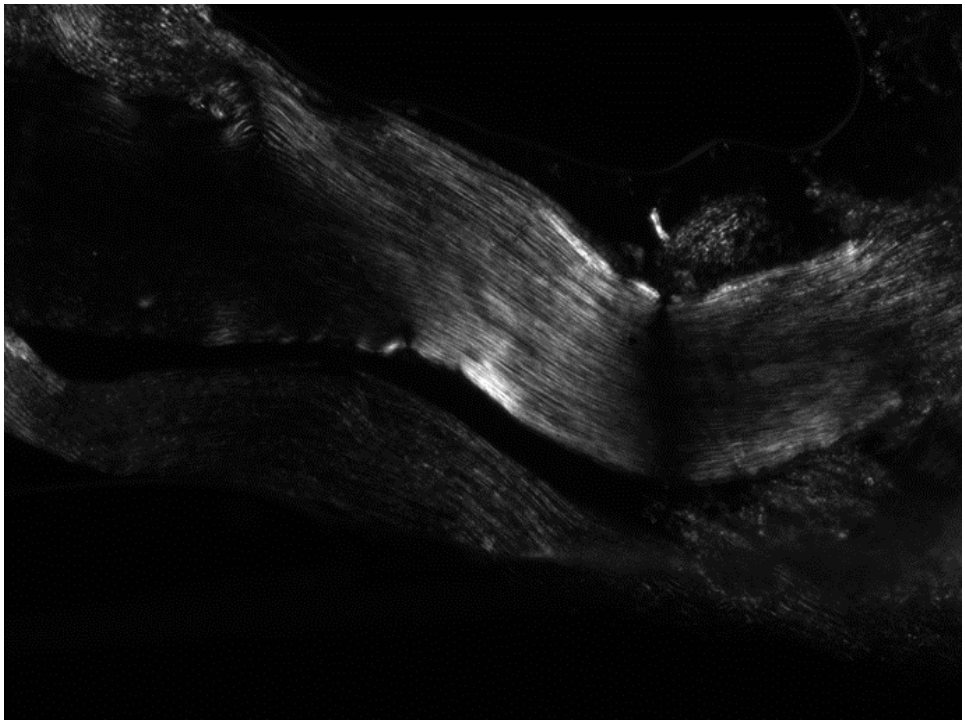

Figure 5-14. A crooked section of the nerve shows intensity pattern.

A section of a nerve made crooked in the illumination area reveals the angle-dependence of the birefringence.

Figure 5-15 shows magnified images of the flattened nerve bundle, revealing more individual axon information. A–C are 40x images of a nerve subset, while D–F are 60x images of individual axons separated from a subset. As the nerve subset is rotated, features of the axons are revealed. Overlapping edges of axons are the primary sources of the birefringence, and give a striated appearance in the images. This trend is even clearer in the images of individual axons. The long thin lines tracing the outer edges of the axons are indicative of a strong birefringence in the myelin sheath. This is to be expected, since the optic axis is known to be radial, as discussed in section 2.4.1, and the myelin sheath is a series of overlapping phospholipid bilayers. As this sheath breaks down, such as during cellular death (Figure 5-15F), the myelin and membranes break apart and congeal into

globules, which heavily scatter light. At this stage, when the nerve was rotated, local intensities did not change as significantly.

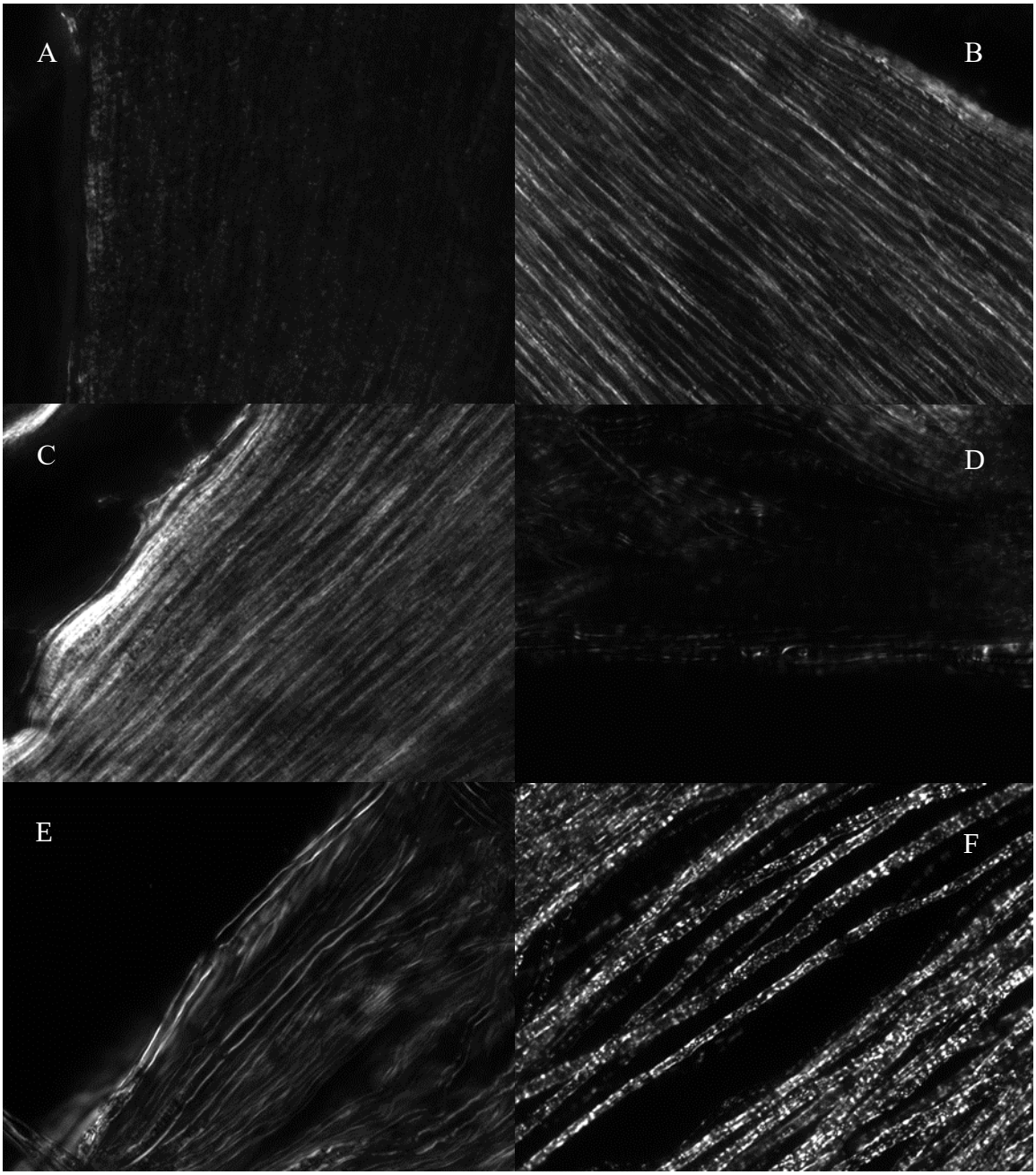


Figure 5-15. Angle dependence of nerve subset birefringence.

A) A subset of the whole nerve at 90° is shown with low intensity. B) The same subset when viewed at 135° reveals a much stronger intensity at the axonal boundaries. The

signal is present almost exclusively where myelin is located. C) The same subset is shown at 45°. D) A splayed out section of the nerve revealing individual axons is shown at 0° with low intensity of light as in image A. Components of axons at some oblique angle to the polarizers show some birefringence and scattering effects. E) The same section of the nerve from image D is shown at 45°. The vast majority of light undergoing rotation is due to birefringence of the myelin sheath and axonal membrane. The highest intensity of light came from the axonal membranes whose widest sides were in the focal plane. F) As the nerve dies, the membranes and myelin begin to deteriorate and the membranes form droplets which scatter light significantly.

The nodes of Ranvier were able to be detected, as shown in Figure 5-16. A–C are birefringence images of small flattened sections or individual axons, and D is an image of a subset. The circled areas indicate the position of nodes of Ranvier, where the membrane appears to be 'pinched' and the birefringence seems to decrease significantly. We are convinced that these are nodes, as they match the appearance of "Ranvier constriction zones" that were observed previously (de Campos Vidal et al. 1980).

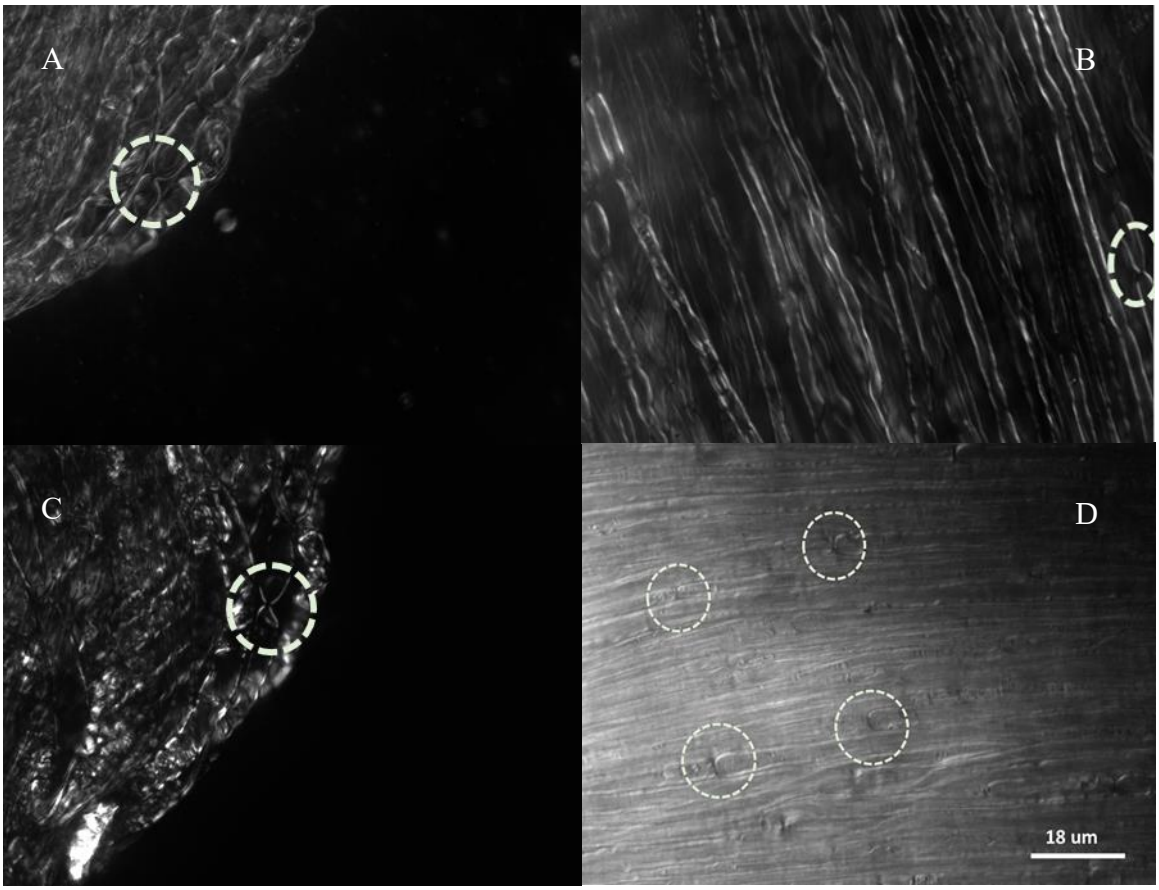


Figure 5-16. Birefringence of nodes of Ranvier.

A) One example of a detected node of Ranvier is shown. B) Another example of a node is shown. C) A clearer example of a node shows that the birefringence signal seems to disappear at the node. D) A clear depiction of the nodes of Ranvier in a nerve subsection. Four nodes were detected in this image, despite the loss of clarity due to the overlapping axons. The birefringence is lower at the nodes than where oriented myelin is.

The information gained thus far has strongly indicated a specific location of the largest birefringence at the widest edges of the axonal membranes. This was verified during experiments. As the focal plane was shifted vertically, the distinct lines at the edges came into and out of focus, rather than a presence of new lines along the radial axes of the axons. A simple explanation can be given for this. If the optic axes are radial, then the rotation induced on light by the incident side of the axonal membrane and

myelin sheath occurs in one direction, and when passing through the exiting side of the axon, it is effectively canceled out by being rotated in the opposite direction. This would occur for any centrosymmetric axonal region, which is a fairly common approximation of an axon. The only part of the axon which would not have this rotation event canceled, is the outermost edges of the axonal membranes (radial axes perpendicular to the propagation direction of light). A depiction of this is shown in Figure 5-17.

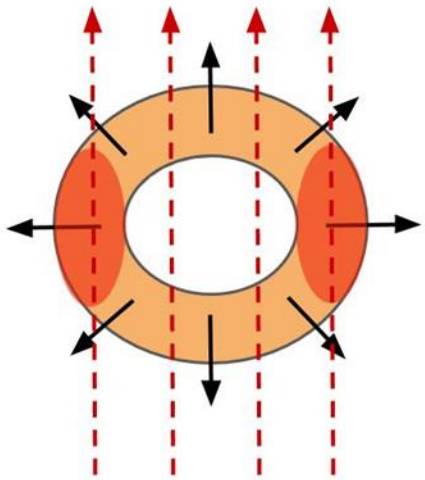

Figure 5-17. Depiction of birefringence from myelin sheath and axonal membrane. The majority of the birefringence signal appeared to originate in the membranes at the widest part of the axons, for light propagating perpendicular to the long axis of the axons, as depicted. This only works if the axon's optic axis is radial, which agrees with previous reports. Birefringence outside of the widest part of the axon was much less significant. Image was created by Anna Slatterty.

The explanation for the nature of the static birefringence signal in myelinated axons depicted in Figure 5-17 presents a complication. Since the XPS has a polarity-dependence on the electric field, and because the orientation of those fields would be in opposing directions at the periphery of the axon perpendicular to the propagation

direction of light, the rotation of light would occur in opposite directions on one side compared to the other. If that is the case, then one axon overlaid with its right side over the left side of an adjacent axon would result in a signal that is reduced, due to cancelation effects on the rotation of light. Occasionally, this seemed to be observed due in some images, where one edge of an axon appeared darker than the other, such as in figure 5-15E. This is not an issue for imaging large-scale compound signals in a nerve, but if one axon is of interest, it could complicate measurements.

Areas where the nerve had inadvertently crossed back over itself revealed interesting information. Figure 5-18 shows two such conditions. When the two section of the crossing nerve are orthogonal to one another and placed at about 45° to the polarizers, the effective birefringence is either decreased (A) or increased (B), depending on the direction of the two layers. This indicates that the nerve birefringence induces a consistent overall rotation of light which can be effectively un-rotated in the manner that a waveplate can be used to rotate a field of light. Thus, to some extent, myelinated nerves behave as a waveplate of sorts.

A

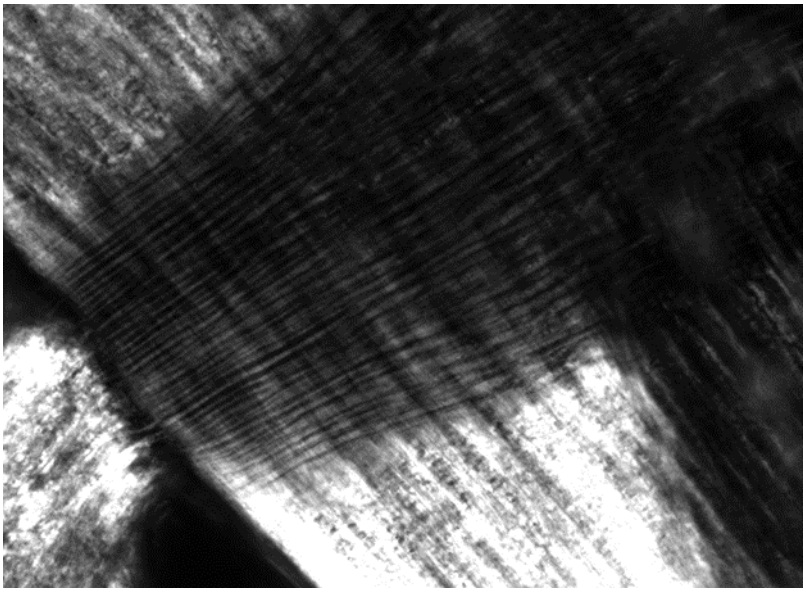

B

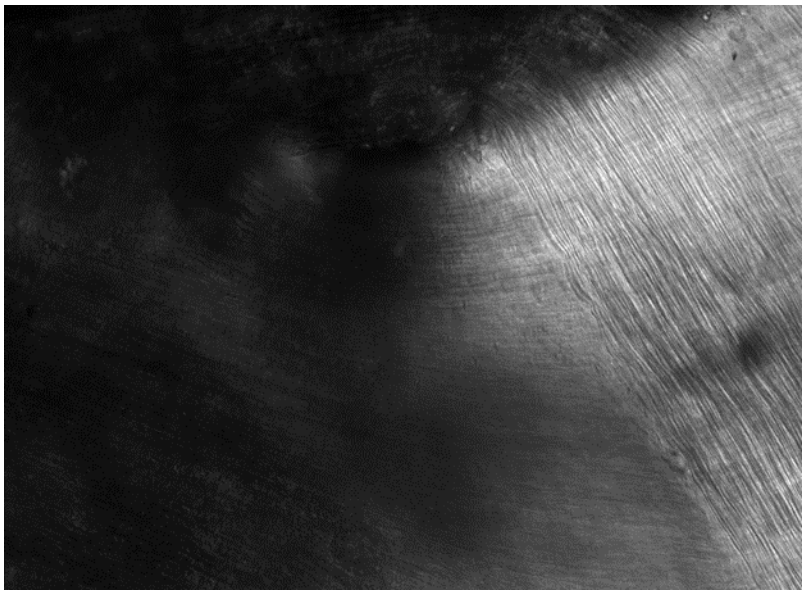

Figure 5-18. Crisscrossing nerve sections canceling-out birefringence.

A) When the nerve was overlapped over itself at 45° and 135°, one layer had the effect of masking the layer behind it. The rotation effects of the first layer were replaced by the rotation events of the optically active parts of the second layer underneath. However, in this configuration it was difficult to determine if the effects were mostly related to absorption. B) When a section of a nerve was found in which the layers were overlapping in the other position, it was found that the intensity was increased, compared to where it does not overlap. Therefore, in this configuration, this section of the nerve's effective birefringence was increased.

### *5.5.3. Manipulating the static birefringence intensity using a quarter waveplate*

Using a QWP to reduce the static birefringence level was attempted with the lobster WLN, as mentioned in section 3.3.3, but the experiment failed. The experiment was revisited for sciatic nerves, with modifications to the design. A HeNe laser was used to illuminate a flattened subset of a nerve at 633 nm, and a QWP designed for that wavelength was placed before the analyzing linear polarizer, for manipulating the nerve birefringence. The 2D detector array and readout circuit from a Logitech webcam was exposed and repurposed to image light from the nerve, through Logitech software. A depiction of this setup is shown in Figure 5-19. As with the previous section, Anna Slatterty aided in data collection and optical setup design for this work.

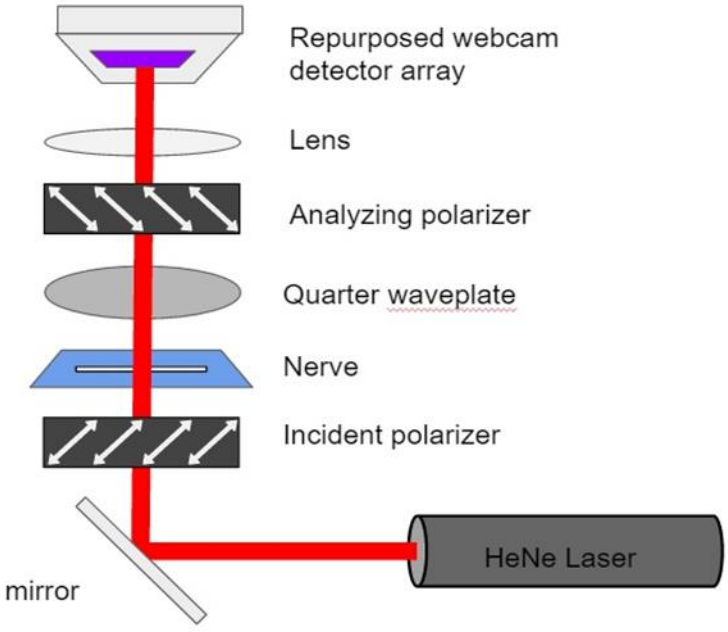


Figure 5-19. Setup for quarter waveplate experiment.

A HeNe laser was used to illuminate the nerve at 633 nm, which maximized the QWP efficiency. The QWP was positioned before the analyzer, to manipulate the birefringence

of the nerve. The detector and circuit from a webcam was used to image in 2D. Image was created by Anna Slatterty.

Images were first taken without the QWP, to image birefringence in the nerve with this setup, and to verify that other optical signals were not significant, as shown in Figure 5-20. With the nerve parallel to the incident linear polarizer's axis, only a small amount of light reached the detector, in large part due to randomly-polarized scattering. The nerve at 45° to the polarizers produced a maximum birefringence, with a significant amount of light reaching the detector. The pattern of the birefringence in Figure 5-20B appeared to be random, from a combination of speckle from the laser and randomly positioned axons within the bundle subsection. However, as long as the structures and optics remained stationary, the pattern for a given experimental trial was consistent.

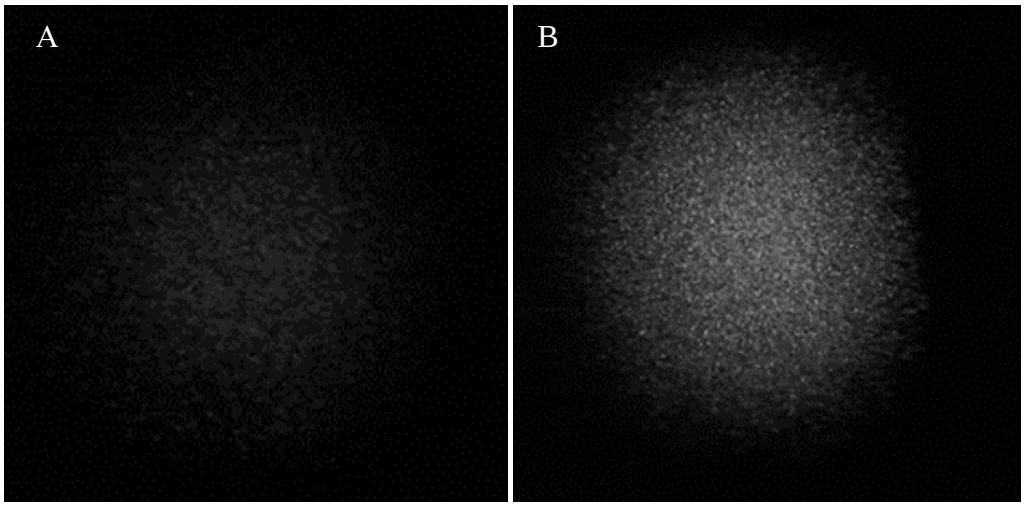


Figure 5-20. Verification of birefringence in setup without a quarter waveplate.
A) When the nerve is placed with its long axis oriented in parallel with the incident polarizer, the intensity of light is low, but non-zero, due in large part to randomly-polarized scattering. B) When the nerve is placed at 45°, a significant birefringence is demonstrated. The pattern demonstrates a random pattern of light arriving at the detector.

Birefringence was manipulated using a QWP whose fast axis was at angles of 0° (incident polarizer), 45° (long axis of nerve), 90° (analyzer), and 135° (perpendicular to long axis of nerve), as shown in Figure 5-21. The birefringence pattern was off-axis slightly from the background due to small discrepancies in the angles of the optical components, and possibly refraction effects related to the imperfect anisotropic structure of the nerve. With the QWP's fast axis oriented in the direction of either polarizer, its effect on rotating light was minimal, and negligible, with exception to a small amount of noise due to the non-ideal nature of the waveplate's microscopic structure. With the QWP fast axis oriented either parallel or perpendicular to the nerve, background light (to the left or right of the 'speckle pattern') is circularly polarized and therefore reaches the detector. Light which passed through the nerve and already experienced birefringence ('speckle pattern') was either rotated less (Figure 5-21B) or more (Figure 5-21D). This indicated, as in Figure 5-18, that the nerve induces an overall rotation in one direction, and that rotation can be increased or decreased with a quarter waveplate. That the nerve effectively behaves as a waveplate is itself an interesting result.

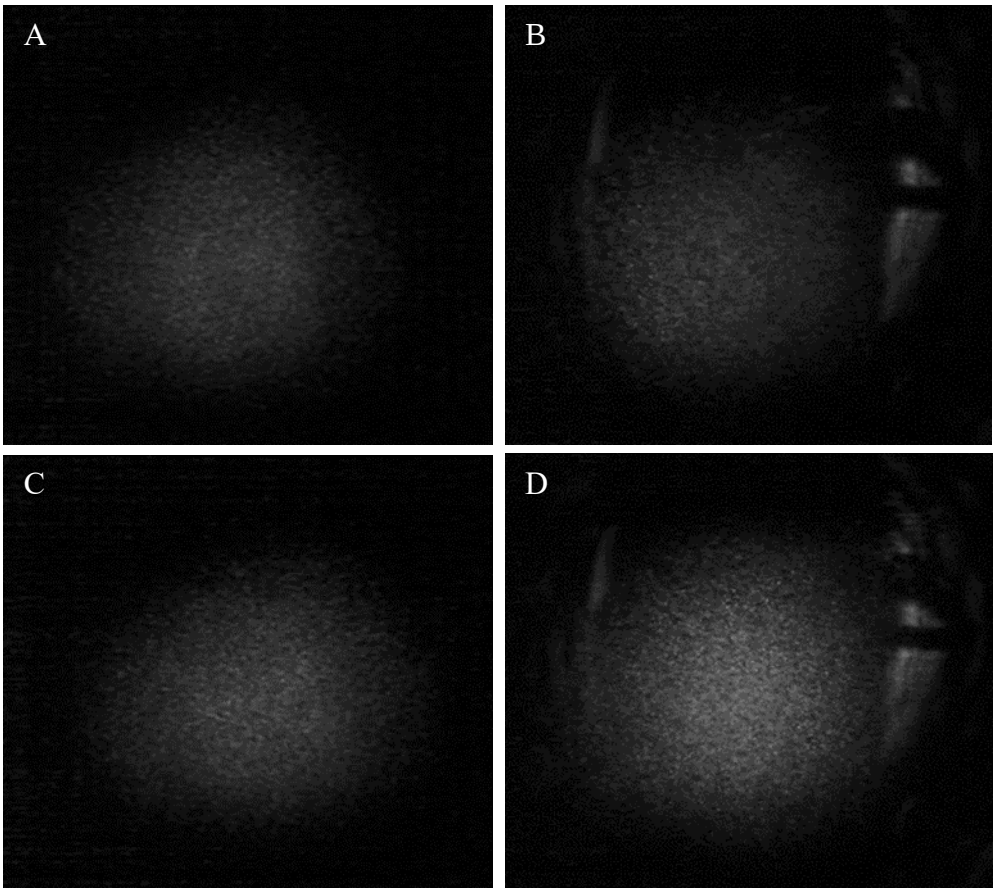


Figure 5-21. Effect of QWP angle on intensity from sciatic nerve.

Birefringence was manipulated using a QWP whose fast axis was at angles of A) 0° (incident polarizer), B) 45° (long axis of nerve), C) 90° (analyzer), and D) 135° (perpendicular to long axis of nerve). With the QWP's fast axis oriented in the direction of either polarizer, it's effect on rotating light was minimal. When the QWP's fast axis was oriented either parallel or perpendicular to the nerve, background light (to the left or right of the 'speckle pattern') was circularly polarized and therefore reached the detector, but light which passed through the nerve and already experienced birefringence ('speckle pattern') was either rotated less (B) or more (D).

Light from the laser effectively formed a Gaussian distribution, with the center two thirds of the birefringence area of the image containing the majority of the light. The intensity of this area was quantified for each of the four images in Figure 5-21, and normalized to the brightest, from Figure 5-21D (QWP fast axis perpendicular to the

nerve's long axis). These measurements for each image (A–D) were 34%, 28%, 41%, and 100%, respectively. This served as a quantification of the manipulation of birefringence by a QWP and demonstrated that the nerve's overall birefringence could be increased or decreased, but only at the loss of signal-to-background contrast.

The QWP was also manipulated with very minute changes in angle when the fast axis was oriented parallel with the incident polarizer (as for Figure 5-21A). Each pixel in the area of birefringence in the image showed random increases or decreases as the QWP was manipulated in this manner. However, the summed intensity of the whole birefringence area did not change significantly. These results reveal that the nerve has a large-scale birefringence that can be manipulated, but each individual part of the birefringence area (containing summed information from overlapping axons and connective tissue) behaves independently and randomly, as the QWP angle is changed. Due to the complex nature of this signal, use of a QWP to improve the SNR would prove difficult. Even if the static birefringence is decreased by using the QWP as in the configuration for Figure 5-21B, contributions from increased background light would complicate signal collection, and be worse for thin tissues. It could be useful if the setup accounts for these issues.

### *5.5.4. Measuring the XPS*

Measuring the XPS in a myelinated nerve was the biggest component of Aim 3. Changes in birefringence have previously never been detected in myelinated neuronal tissue, and detecting these signals in myelinated sciatic nerves, whose APs travel much

faster on average than in the previously studied crustacean nerves, would open the door toward application to imaging XPS of AP activity in more clinically relevant research.

#### 5.5.4.1. Methods

Methods for measuring the XPS of mouse sciatic nerves were generally the same as those used in Chapter 3 for the lobster WLNs. The primary differences were the nerve chamber used, the light source, and the stimulation parameters. Sciatic nerves were shorter in length (usually ~1.5 cm) than the WLNs (4–5 cm), so the nerve chamber that was designed for the songbird nerve experiments (Figure 5-10) was used. The LED was difficult to focus tightly enough to produce a large intensity on the nerve and detector to maximize the SNR, so the SLD mentioned in section 3.3.7 was used.

The stimulation parameters were adjusted to empirically determine the optimal stimulation amplitude and duration, which differ based on the type of nerve and the nerve chamber. Compared to the WLN, APs travel much faster in a myelinated nerve, so a reduced stimulus duration was used. For the nerve chamber used here the distance between the stimulus and recording sites is only around 8 mm. If some APs are traveling > 50 mm/ms, then they will arrive at the first recording electrode after only ~150$\mu$s. At a duration of 1 ms, the standard duration for the lobster WLN, the entire electrical signal for the sciatic nerve APs was hidden behind the stimulus artifact, regardless of amplitude. A duration of 100 $\mu$s was also attempted, but seemed to produce a response that was too wide and even overlapped somewhat with the artifact, even when reducing the amplitude

to low levels. A stimulus duration of around 10 $\mu$s seemed to elicit the best response when stimulated at amplitudes ranging from 600 $\mu$A to 14 mA.

5.5.4.2. Experiments and analysis

Obtaining a signal was difficult, as the compound signal travels at a rapid rate and had never been measured, so the nature of the signal relating to myelination was not known. The first step taken to determine if measuring the AP-related XPS was viable was to measure an easier signal to obtain, the XPS in response to applied fields, as in section 3.4.6 for the lobster WLN. The same square voltage pulses used in the WLN experiments were applied to the sciatic nerves and the XPS measured at the site of application, and the un-averaged results are shown in Figure 5-22. The 'on' and 'off' responses were much slower than what was found for the WLN, with the nerves exhibiting a slow, capacitive-like charging and discharging. For higher amplitudes, the discharging response was bipolar, recovering from above baseline, which was never observed for the WLN. These features may be related to the presence of myelination.

The amplitude of the XPS followed a linear electro-optic response to the applied voltages (Figure 5-22C). This is in complete agreement with data from the WLN, with exception to the specific range of voltages across which the linearity transpires, which may just be related to differences in the chambers and dielectric properties of the nerves. This linear response implies that much of the same phenomena in the WLN related to the XPS are involved with the XPS for the sciatic nerve, particularly that changes in the electric fields in the tissues directly induce changes in the XPS.

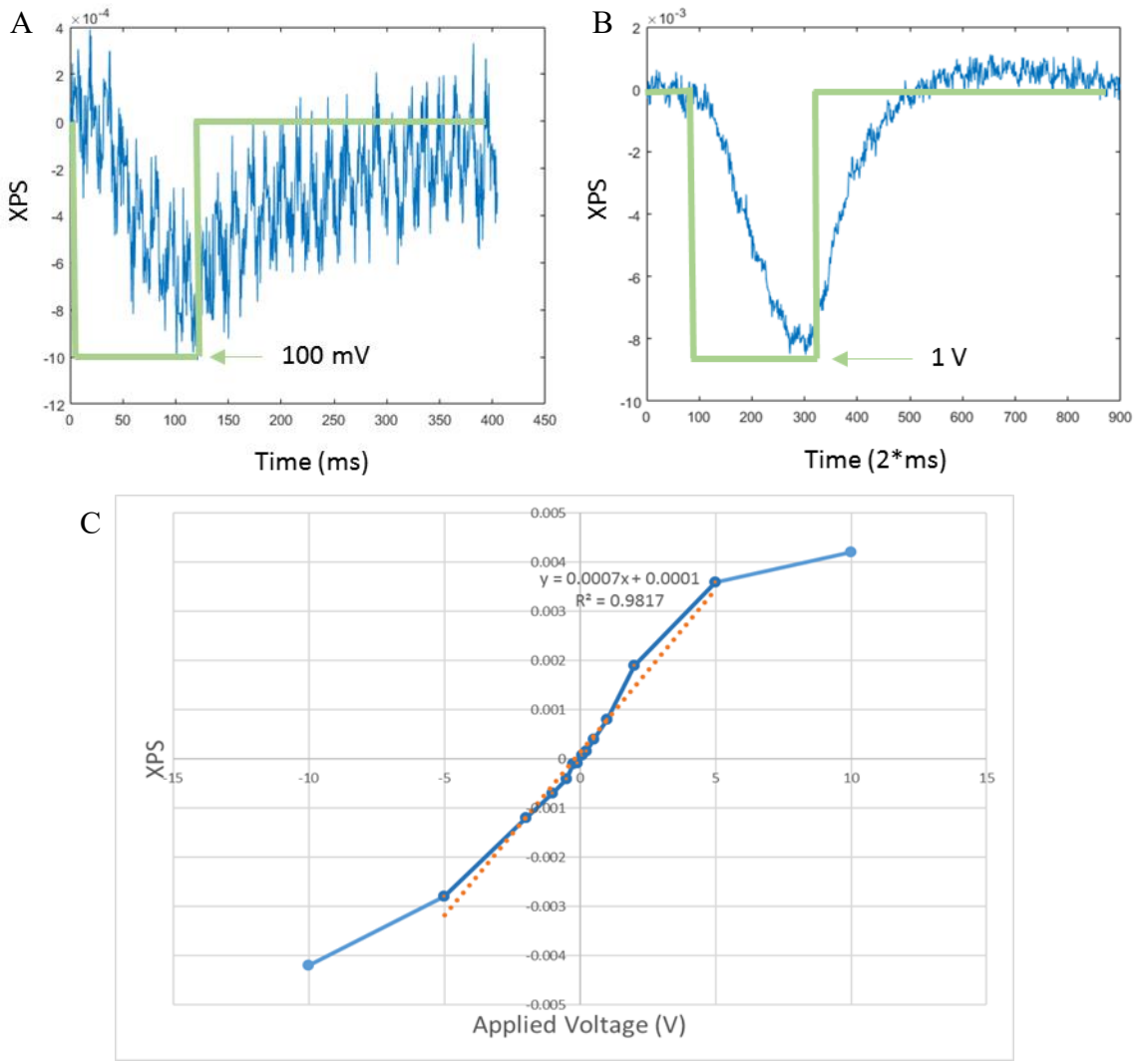


Figure 5-22. Sciatic nerve XPS in response to applied field.

A) A 100 mV square pulse of 128 ms was applied to the nerve, and the XPS followed the onset and recovery, with a capacitive-like decay, as was the case with the lobster WLN. B) A 1 V pulse demonstrates a response in magnitude of the XPS that is around ten times that of the 100 mV pulse. The time constants are much slower than those of the WLN. This may be related to the presence of the myelin sheaths. C) The response of the XPS as a function of applied voltage magnitude was linear in the range of -5 V to 5V, which was similar to the WLN.

The specific stimulus amplitude at which APs are generated differs for each nerve. For one sciatic nerve, traces of the electrical recordings are shown in Figure 5-23.

At 500 $\mu$A, the stimulus artifact was evident, but no signs of subsequent AP activity were present. When the stimulus was increased to 600 $\mu$A, however, the threshold for AP generation was reached and a bipolar response related to APs arose in the recording. One polar side of the signal was larger than the other for almost every measurement, which likely is due to the ligated end of a nerve being located in the middle of the second recording well. This bipolar response was never observed for the WLN, because the slow nature of the compound APs in the WLN spread out significantly by the time they reach the recording wells. These electrical traces provided valuable knowledge as to when to expect the XPS and what we might expect, as the XPS is almost instantaneously correlated to changes in the electric field associated with propagating APs.

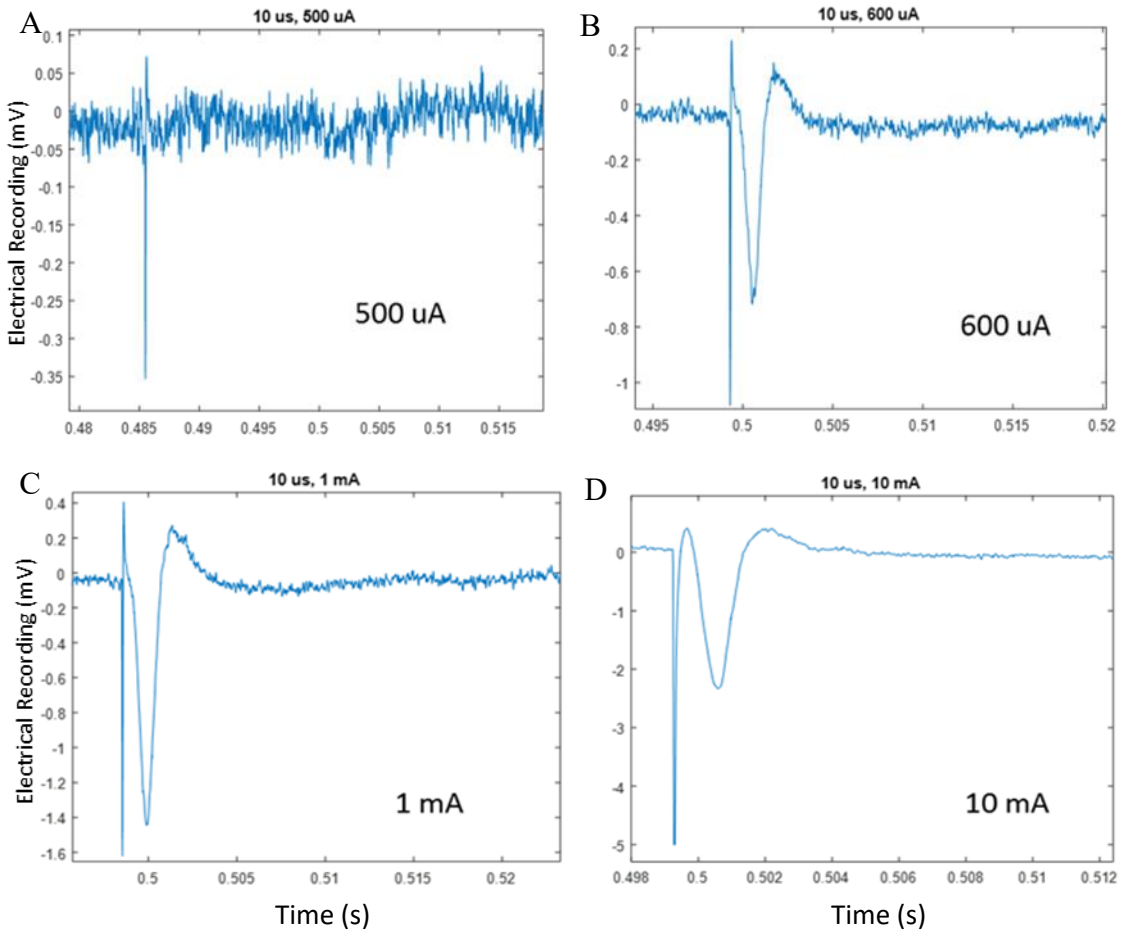


Figure 5-23. Electrical recordings of AP activity at various stimulus amplitudes.

A) A recording of the electrical signal for a stimulus magnitude of 500 $\mu$A shows little to no AP activity, but the stimulus artifact is evident. B) When a 600 $\mu$A stimulus was applied to the nerve, a bipolar response was recorded, which is standard for sciatic nerves when measuring the compound AP with the pair of electrodes spaced apart along the length of the nerve. The velocity of the compound AP was around 15–20 mm/ms, as measured by the arrival of the peak. C) At 1 mA, many of the axons are recruited, and the compound signal increases substantially. D) At 10 mA, most of the axons have been recruited to fire APs (note the y-axis scale).

Obtaining an XPS proved to be difficult, as many sudden sources of noise had to be fixed over time. Eventually, a trace of the XPS was recorded at a stimulus amplitude of 14 mA (to maximally recruit axons, but not shown as it appears very similar to the plot

shown in Figure 5-23D), shown in Figure 5-24, with only 20 periods averaged. The response observed lasted a duration of only around 500 $\mu$s at a site ~4 mm from the stimulus (at the area of illumination), with the peak occurring around 0.4 ms (~10 mm/ms compound AP velocity). It is possible that the number of axons recruited was not high, but the amplitude of the XPS was higher than typically observed for the lobster WLN, which is expected for concurrently arriving APs. The bipolar nature of the XPS was not expected, since it had not been observed in other nerves, with exception to the slow recovery of the horseshoe crab LON. Nonetheless, this was the first recorded XPS in a mammalian nerve.

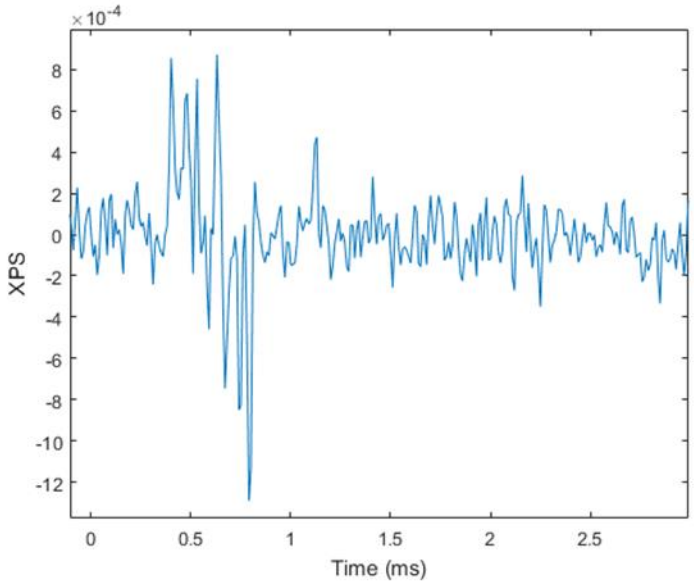


Figure 5-24. XPS recording of a sciatic nerve.

The XPS response was so rapid, that the digital bandpass filter had to be changed to a low-pass cutoff frequency of 20 kHz to prevent loss of detail. The signal appears to be bipolar, which is different compared to the lobster WLN, whose XPS never goes positive in value.

## 5.6. Discussion

The primary goal of Aim 3 was to demonstrate changes in birefringence in mammalian neuronal tissues, and to investigate the effects that myelination may have on the signal, since until now it has only been detected in unmyelinated crustacean axons and nerve bundles. The first attempts to detect the XPS in neuronal monolayers were unsuccessful due mostly to a lack of general anisotropy in the samples. Due to the difficulty of growing samples with such an anisotropy, and the availability of *ex vivo* tissue samples for research, we moved on to mouse brain slices, with the hope that it would open up the path for the XPS to be a viable brain imaging method. The anisotropic nature of the Schaffer collaterals between the CA3 and CA1 neurons were known to be significantly birefringent (Zeineh et al. 2016), so this area was chosen for the XPS. It proved difficult to handle the slices and keep enough neurons alive that could propagate the APs downstream to the imaging location.

Since the XPS had been reliably detected in unmyelinated crustacean peripheral nerves, we changed our focus to myelinated mammalian peripheral nerves. The first samples we could obtain were zebra finch laryngeal nerves, but these were found to be difficult to handle due to their size and significant connective tissue structure, and would not produce a reliable electrical response to an external stimulus. Mouse sciatic nerves were a good size for handling and external stimulation, and are heterogeneous in axon size distribution, making them a great comparator for the lobster WLN. We were fortunate in being able to use mice sacrificed for other purposes, whose sciatic nerves otherwise remained intact.

While static birefringence of myelin has been studied (de Campos Vidal et al. 1980), we sought to investigate how it could affect the birefringence in a way that changes the XPS from unmyelinated axons. Placing the nerve in a modified DIC microscope allowed us to image static birefringence from myelination with high resolution under a variety of conditions. The best images yet taken of nerve birefringence are shown in section 5.5.2. The most significant result from this study was the crisscrossing nerve sections in Figure 5-18. That the direction of overlap of the two nerve layers causes the birefringence to either increase or decrease, depending on orientation, is a strong indication of the nerve's overall birefringent properties. The rotation events induced by the constituent axons and connective tissues have an overall direction of preference. This was further verified through use of a quarter waveplate placed before the analyzer, which was used to either increase or decrease the birefringence of the nerve, based on the orientation of the waveplate relative to the myelinated nerve and polarizers. When this study was performed on unmyelinated nerves, this response was not found, or not as pronounced.

Repeating the applied field experiment from section 3.4.6 in sciatic nerves demonstrated that the presence of myelination does not affect the nerve's linear response to the magnitude of applied electric fields. This is informative, as it indicates that the myelin sheath does not change the manner in which fluctuating electric fields alter the nerve birefringence. The myelin does, however, appear to decrease the response time of the nerve to external fields. As its purpose is to act as an electrical insulator, this not

surprising. The total tissue capacitance and impedance should be affected by the presence of myelin.

The XPS was able to be detected in a sciatic nerve. This is the first detection of the XPS in a non-crustacean nerve, or in any myelinated tissue. Its bipolar nature was not expected, but bipolar features were present in the horseshoe crab lateral optic nerve. Perhaps bipolar features appear in the XPS when APs from a large number of different axons arrive at a location in a short time span, with depolarization and hyperpolarization events occurring around the same time. Another possible explanation is that the XPS in nerves with myelination may follow the change in the electric fields, rather than their amplitudes. More studies are needed to determine the basis of this XPS shape, and more work is needed to reliably obtain these signals. Regardless, the detection and characterization of this signal paves the way toward using this as an imaging modality in humans.

## 5.7. Aim 3 Conclusions

Extending this work in the direction of clinical applications first required a demonstrate that the signal is present. The effects of myelination on changes in birefringence was previously unknown. We made significant progress in the attempt to investigate birefringence of myelination. For the first time, the XPS of a myelinated tissue has been detected. Further work in investigating the nature of this signal is needed.

# CHAPTER 6. CONCLUSIONS

## 6.1. Summary of Specific Aims

Since changes in birefringence in neurons are associated instantaneously with electrophysiological phenomena, they are well-suited for fast imaging of propagating action potentials in neuronal tissue. Overall, the goal of this work was to further investigate these signals and gain a better understanding of them, both in unmyelinated and in higher order myelinated neuronal tissues. The focus was on steering this work in the direction of eventual pre-clinical or surgical application.

In Aim 1, Part 1, improvements to our methodology and to the SNR of the signal in our setup were investigated. The crossed-polarized signal (XPS) in nerves (and individual axon) is small, and improving the signal-to-noise would make detecting this signal an easier task, and present the XPS as a viable candidate for detecting AP activity in anisotropic nervous tissue.

In Aim 1, Part 2, we carried out a series of experiments with a goal of better understanding the XPS of the lobster WLN. The physiological mechanisms underlying the cause of these changes in birefringence in neuronal tissue remain under discussion. Our data collectively serves as a strong indication that there is a capacitive-charging-like effect directly inducing a gradual recovery of the XPS to baseline, and also causing a smoothing of the XPS trace. Determining specifically which physiological structures may be behind these changes in birefringence involving the peak of the XPS and the gradual recovery is left for future investigation.

In Aim 2, we utilized the information on improved instrumentation and SNR from Aim 1, and develop a new benchtop system that enables reliable tracking of the propagation of APs in real-time using the XPS measured in the lobster walking leg nerve (WLN). Our setup successfully demonstrated the feasibility of tracking propagating compound APs in a peripheral nerve using the XPS. This is supported by the detection of all features of the XPS in any decently illuminated PD as well as in the movies of the tracked XPS across all PDs. By extracting a single stimulus interval, we demonstrated that this setup can be used to investigate real-time signal propagation. Although far from clinical applications, these data demonstrate the potential for real-time imaging of AP propagation using changes in birefringence.

In Aim 3, The primary goal of Aim 3 was to demonstrate changes in birefringence in mammalian neuronal tissues, and to investigate the effects that myelination may have on the signal, since until now it has only been detected in unmyelinated crustacean axons and nerve bundles. More information about birefringence in myelinated tissue was needed to better understand these signals and make predictions on what to expect when the XPS is observed. Since the dynamic birefringence signal (the XPS) has not yet been seen, we could estimate what form the signal might take, based on the structural properties of the myelinated tissue, and the expected effects of myelination. Extending this work in the direction of clinical applications first required a demonstrate that the signal is present. Although efforts to first detect the XPS in monolayer cultures, brain slices and the songbird laryngeal nerves were unsuccessful, we made significant progress in the attempt to investigate birefringence of myelination with mouse sciatic nerves. For

the first time, the XPS of a myelinated tissue has been detected, and appeared to have a bipolar shape. Further work in investigating the nature of this signal is needed.

## 6.2. Future Directions

Our lab will continue to investigate birefringence of myelination and how it affects the XPS. We also will be looking more into the nature of the observed bipolar XPS in the sciatic nerve.

While changes in birefringence have been imaged primarily in a transmission setup, measurement has also been demonstrated in a backscattering geometry, although the SNR was lower than in transmission (see Figure 6-1) (Yao et al. 2005). Both regimes may be useful toward utilizing these signals to noninvasively image AP activity in nerves. Backscattering geometry could be used to image activity in higher-level neuronal tissues, such as the cortex, but due to their less-oriented structure, the XPS would be more difficult to detect. Polarization-maintaining fibers could be used to direct light to and from a sample *in vivo* for transmission or reflection geometry. Additionally, circularly polarized light may be advantageous for imaging back-scattered light in thicker tissues, since circularly-polarized light retains its polarization state through more scattering events than linearly polarized light (Morgan & Ridgway 2000). In summary, imaging based on polarization sensing of changes in birefringence offers promise for an improved noninvasive method of detecting and tracking AP activity in nervous tissues, and may eventually be developed for clinical application, such as surgical detection.

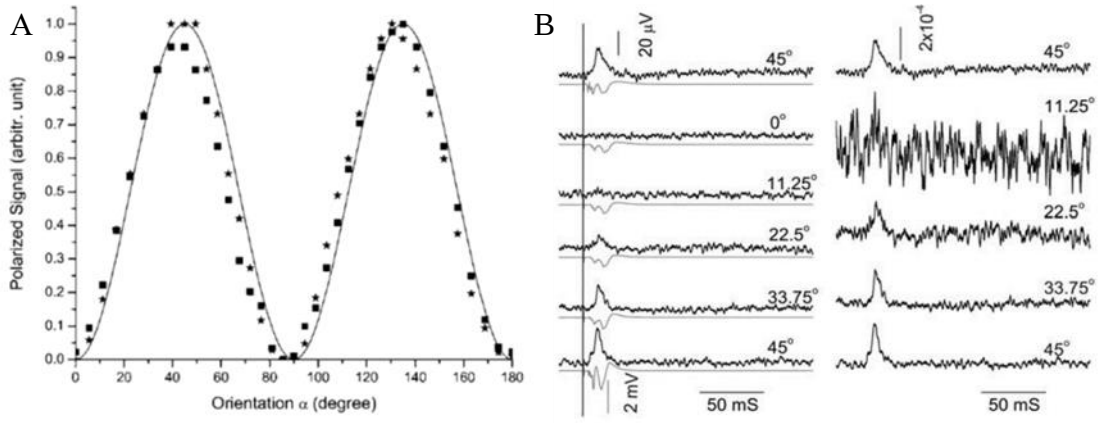


Figure 6-1. XPS measured in reflection geometry (Yao et al. 2005).

A) A verification that the signal was birefringence was performed in a similar manner to previous work. B) The XPS in reflection geometry for different angles of the nerve.

### 6.3. Final conclusion

The data presented in this work serves as a strong indication that changes in birefringence can be utilized to image action potential propagation in neuronal tissues, while providing invaluable insights into the nature of these signals in different neuronal tissues. Since changes in birefringence in neurons are associated instantaneously with electrophysiological phenomena, they are well-suited for fast imaging of propagating action potentials in neuronal tissue. In summary, imaging based on polarization sensing of changes in birefringence offers promise for an improved noninvasive method of detecting and tracking AP activity in myelinated and unmyelinated nerves and could be designed for pre-clinical and surgical applications.

# REFERENCES


Assaf, Y. et al., 2008. AxCaliber: a method for measuring axon diameter distribution from diffusion MRI. *Magnetic resonance in medicine*, 59(6), pp.1347–54.

Ba, A.M. et al., 2002. Multiwavelength optical intrinsic signal imaging of cortical spreading depression. *Journal of neurophysiology*, 88(5), pp.2726–35.

Badreddine, A.H., Jordan, T. & Bigio, I.J., 2016. Real-time imaging of action potentials in nerves using changes in birefringence. *Biomedical optics express*, 7(5), pp.1966–73.

Badreddine, A.H., Schoener, K.J. & Bigio, I.J., 2015. Elucidating the temporal dynamics of optical birefringence changes in crustacean nerves. *Biomedical optics express*, 6(10), pp.4165–78.

Bala, U. et al., 2014. Harvesting the maximum length of sciatic nerve from adult mice: a step-by-step approach. *BMC research notes*, 7(1), p.714.

Battelle, B.-A., 2006. The eyes of Limulus polyphemus (Xiphosura, Chelicerata) and their afferent and efferent projections. *Arthropod structure & development*, 35(4), pp.261–74.

Brázdil, M. et al., 2005. Reorganization of language-related neuronal networks in patients with left temporal lobe epilepsy - an fMRI study. *European journal of neurology*, 12(4), pp.268–75.

Briggman, K.L., Abarbanel, H.D.I. & Kristan, W.B., 2005. Optical imaging of neuronal populations during decision-making. *Science*, 307(5711), pp.896–901.

Broussard, G.J., Liang, R. & Tian, L., 2014. Monitoring activity in neural circuits with genetically encoded indicators. *Frontiers in molecular neuroscience*, 7, p.97.

Butson, C.R. & McIntyre, C.C., 2005. Tissue and electrode capacitance reduce neural activation volumes during deep brain stimulation. *Clinical neurophysiology*, 116(10), pp.2490–500.

de Campos Vidal, B. et al., 1980. Anisotropic properties of the myelin sheath. *Acta histochemica*, 66(1), pp.32–9.

Canto, C.B., Wouterlood, F.G. & Witter, M.P., 2008. What does the anatomical organization of the entorhinal cortex tell us? *Neural plasticity*, 2008, p.381243.

Carter, K.M., George, J.S. & Rector, D.M., 2004. Simultaneous birefringence and scattered light measurements reveal anatomical features in isolated crustacean nerve. *Journal of neuroscience methods*, 135(1–2), pp.9–16.

Chinn, P. & Schmitt, F.O., 1937. On the birefringence of nerve sheaths as studied in cross sections. *Journal of Cellular and Comparative Physiology*, 9(2), pp.289–296.

Cohen, LB, Keynes, RD and Landowne, D., 1972. Changes in light scattering that accompany the action potential in squid giant axons: potential-dependent components. *Journal of physiology*, 224(3), pp.701–725.

Cohen, LB and Keynes, R., Cohen, L.B. & Keynes, R.D., 1971. Changes in light scattering associated with the action potential in crab nerves. *Journal of Physiology*, 212(1), pp.259–275.

Cohen, L.B. et al., 1971. Analysis of the potential-dependent changes in optical retardation in the squid giant axon. *Journal of Physiology*, 218(1), pp.205–237.

Cohen, L.B., 1973. Changes in neuron structure during action potential propagation and synaptic transmission. *Physiological reviews*, 53(2), pp.373–418.

Cohen, L.B. et al., 1969. Light scattering and birefringence changes during activity in the electric organ of Electrophorus electricus. *Journal of physiology*, 203(2), pp.489–509.

Cohen, L.B. & Haven, N., 1973. Changes in Neuron Potential Propagation Structure During Action and Synaptic Transmission. *Physiological reviews*, 53(2), pp.373–418.

Cohen, L.B., Hille, B. & Keynes, R.D., 1970. Changes in axon birefringence during the action potential. *Journal of physiology*, 211(2), pp.495–515.

Cohen, L.B., Keynes, R.D. & Hille, B., 1968. Light Scattering and Birefringence Changes during Nerve Activity. *Nature*, 218(5140), pp.438–441.

Csicsvari, J. et al., 2003. Massively parallel recording of unit and local field potentials with silicon-based electrodes. *Journal of neurophysiology*, 90(2), pp.1314–23.

Darin De Lorenzo, A.J., Brzin, M. & Dettbarn, W.D., 1968. Fine structure and organization of nerve fibers and giant axons in Homarus americanus. *Journal of ultrastructure research*, 24(5), pp.367–84.

Debanne, D. et al., 2011. Axon physiology. *Physiological reviews*, 91(2), pp.555–602.

Derby, C.D. & Atema, J., 1982. Chemosensitivity of Walking Legs of the Lobster Homarus Americanus: Neurophysiological Response Spectrum and Thresholds. *Journal of experimental biology* 98(1), pp.303–315.

Dreier, J.P., 2011. The role of spreading depression, spreading depolarization and spreading ischemia in neurological disease. *Nature medicine*, 17(4), pp.439–47.

Evans, P.D. et al., 1976. The association of octopamine with specific neurones along lobster nerve trunks. *Journal of physiology*, 262(1), pp.51–70.

Factor, J.R., 1995. *Biology of the Lobster Homarus Americanus*, London: Academic.

Fahrenbach, W.H., 1971. The morphology of the Limulus visual system. *Zeitschrift für Zellforschung und Mikroskopische Anatomie*, 114(4), pp.532–545.

Fahrenbach, W.H., 1975. The visual system of the horseshoe crab Limulus polyphemus. *International review of cytology*, 41, pp.285–349.

Foster, K.R. & Schwan, H.P., 1989. Dielectric properties of tissues and biological materials: a critical review. *Critical reviews in biomedical engineering*, 17(1), pp.25–104.

Foust, A.J. et al., 2008. In vitro and in vivo noise analysis for optical neural recording. *Journal of biomedical optics*, 13(4), p.44038.

Foust, A.J. & Rector, D.M., 2007. Optically teasing apart neural swelling and depolarization. *Neuroscience*, 145(3), pp.887–99.

Furusawa, K., 1929. The depolarization of crustacean nerve by stimulation or oxygen want. *Journal of physiology*, 67(4), pp.325–42.

Grinvald, A. & Hildesheim, R., 2004. VSDI: a new era in functional imaging of cortical dynamics. *Nature reviews. Neuroscience*, 5(11), pp.874–85.

Hodgkin, A.L., 1954. A note on conduction velocity. *Journal of Physiology*, 125(1), pp.221–224.

Iwasa, K., Tasaki, I. & Gibbons, R.C., 1980. Swelling of nerve fibers associated with action potentials. *Science*, 210(4467), pp.338–9.

Johnson, B.R., Hauptman, S.A. & Bonow, R.H., 2007. Construction of a simple suction electrode for extracellular recording and stimulation. *Journal of undergraduate neuroscience education,* 6(1), pp.A21–6.

Landowne, D., 1993. Measuring nerve excitation with polarized light. *Japanese journal of physiology*, 43 Suppl 1, pp.S7–11.

Landowne, D., 1985. Molecular motion underlying activation and inactivation of sodium channels in squid giant axons. *Journal of membrane biology*, 88(2), pp.173–85.

Lodish, H. et al., 2000. The Action Potential and Conduction of Electric Impulses. Section 21.2 in *Molecular Cell Biology*, 4th ed. New York: W.H. Freeman.

Logothetis, N.K. & Pfeuffer, J., 2004. On the nature of the BOLD fMRI contrast mechanism. *Magnetic resonance imaging*, 22(10), pp.1517–31.

Luft, A.R. et al., 2005. Brain activation of lower extremity movement in chronically impaired stroke survivors. *NeuroImage*, 26(1), pp.184–94.

MacVicar, B.A. & Hochman, D., 1991. Imaging of synaptically evoked intrinsic optical signals in hippocampal slices. *Journal of neuroscience*, 11(5), pp.1458–69.

Mathis, D. M., Furman, J. L., Norris, C.M. et al., 2011. Preparation of Acute Hippocampal Slices from Rats and Transgenic Mice for the Study of Synaptic Alterations during Aging and Amyloid Pathology. *Journal of visualized experiments*, 49(49), p.e2330.

Maturana, L.G. et al., 2013. Enhanced peripheral nerve regeneration by the combination of a polycaprolactone tubular prosthesis and a scaffold of collagen with supramolecular organization. *Brain and behavior*, 3(4), pp.417–30.

Morgan, S. & Ridgway, M., 2000. Polarization properties of light backscattered from a two layer scattering medium. *Optics Express*, 7(12), p.395.

Nicholls, J. et al., 2012. *From Neuron to Brain* 5th ed., Sunderland, MA: Sinauer Associates, Inc.

Rector, D.M. et al., 1997. Light scattering changes follow evoked potentials from hippocampal Schaeffer collateral stimulation. *Journal of neurophysiology*, 78(3), pp.1707–13.

Ross, W.N. et al., 1977. Changes in absorption, fluorescence, dichroism, and Birefringence in stained giant axons: Optical measurement of membrane potential. *Journal of membrane biology*, 33(1–2), pp.141–83.

Rowland, C.E. et al., 2015. Electric Field Modulation of Semiconductor Quantum Dot Photoluminescence: Insights Into the Design of Robust Voltage-Sensitive Cellular Imaging Probes. *Nano letters*, 15(10), pp.6848–54.

Schei, J.L. et al., 2008. Action potential propagation imaged with high temporal resolution near-infrared video microscopy and polarized light. *NeuroImage*, 40(3), pp.1034–1043.

Schmitt, F.O. & Bear, R.S., 1937. The optical properties of vertebrate nerve axons as related to fiber size. *Journal of Cellular and Comparative Physiology*, 9(2), pp.261–273.

Schoener, K., 2010. Non-invasive, high-resolution spatiotemporal mapping of neuronal activity through field-induced changes in birefringence. Unpublished doctoral dissertation, Boston University.

Shuttleworth, C.W., 2010. Use of NAD(P)H and flavoprotein autofluorescence transients to probe neuron and astrocyte responses to synaptic activation. *Neurochemistry international*, 56(3), pp.379–86.

da Silva, G.A.R. et al., 2016. Recurrent laryngeal nerve alterations in developing spontaneously hypertensive rats. *Laryngoscope*, 126(1), pp.E40–7.

Smetters, D., Majewska, a & Yuste, R., 1999. Detecting action potentials in neuronal populations with calcium imaging. *Methods*, 18(2), pp.215–21.

Stepnoski, R.A. et al., 1991. Noninvasive detection of changes in membrane potential in cultured neurons by light scattering. *Proceedings of the National Academy of Sciences of the United States of America*, 88(21), pp.9382–6.

Tasaki, I. et al., 1968. Changes in fluorescence, turbidity, and birefringence associated with nerve excitation. *Proceedings of the National Academy of Sciences of the United States of America*, 61(3), pp.883–8.

Tasaki, I. & Byrne, P.M., 1993. The origin of rapid changes in birefringence, light scattering and dye absorbance associated with excitation of nerve fibers. *Japanese journal of physiology*, 43 Suppl 1, pp.S67–75.

Tasaki, I. & Byrne, P.M.M., 1992. Rapid structural chances in nerve fibers evoked by electric current pulses. *Biochemical and Biophysical Research Communications*, 188(2), pp.559–564.

Wininger, F.A., Schei, J.L. & Rector, D.M., 2009. Complete optical neurophysiology: toward optical stimulation and recording of neural tissue. *Applied optics*, 48(10), pp.D218–24.

Witter, M.P. & Moser, E.I., 2006. Spatial representation and the architecture of the entorhinal cortex. *Trends in neurosciences*, 29(12), pp.671–678.

Yao, X.-C. et al., 2005. Cross-polarized reflected light measurement of fast optical responses associated with neural activation. *Biophysical journal*, 88(6), pp.4170–7.

Yao, X.-C., Rector, D.M. & George, J.S., 2003. Optical lever recording of displacements from activated lobster nerve bundles and Nitella internodes. *Applied Optics*, 42(16), p.2972.

Young, J.Z., 1936. The structure of nerve fibres in cephalopods and crustacea. *Proceedings of the Royal Society B: Biological Sciences*, 121(823), pp.319–337.

Zeineh, M.M. et al., 2016. Direct Visualization and Mapping of the Spatial Course of Fiber Tracts at Microscopic Resolution in the Human Hippocampus. *Cerebral cortex,* pii: bhw010. [Epub ahead of print].

VITA

**Ali H. Badreddine**
32 Eastburn St. ● Boston, MA 02135 ● badredah@bu.edu ● 615-598-3023
https://www.linkedin.com/in/alihbadreddine

## SUMMARY

Biomedical engineer with 7+ years experience in independent and collaborative research. Multidisciplinary Ph.D. in biomedical neuroscience and optics involving device design, medical instrumentation, circuit design, 3D print design, signal analysis, and noise reduction. Successfully navigated low-budget conditions while delivering results, including two first-author publications. Mentored and trained graduate and undergraduate students.

## EDUCATION

**Doctor of Philosophy in Biomedical Engineering** **January 2017**
Boston University, College of Engineering, Boston, MA
*Dissertation:* "Optical tracking of nerve activity using intrinsic changes in birefringence"
Research Concentrations: Biomedical Optics, Neuroimaging

**Master of Science in Biomedical Engineering** **September 2012**
Boston University, College of Engineering, Boston, MA
*Thesis:* "Using birefringence to track action potentials in brain tissue"
Relevant Coursework: Biophotonics, Optical Microscopy, Quantitative Physiology, Applic. of Tissue Eng.

**Bachelor of Engineering in Biomedical Engineering,**
*Magna Cum Laude (GPA 3.71/4.0)* **May 2009**
Vanderbilt University, College of Engineering, Nashville, TN
Relevant Coursework: Imaging, Design in BME, Neuroscience, Modeling Living Systems, Biomedical Instrumentation, Systems Physiology, Physiological Transport Phenomena, Circuits I and II, Biomedical Materials

## PROFESSIONAL AND RESEARCH EXPERIENCE

**Boston University, Department of Biomedical Engineering,** Boston, MA

**September 2009 – July 2016**

*Research Assistant, Biomedical Optics Laboratory*

- Developed a novel optical system for tracking nerve signal propagation without the need for cell-killing dyes
- Designed and constructed optical and electronic experimentation systems (including photodiode and LED circuits, lenses, polarizers, control systems, noise insulation, and 3D printed components/chambers)

- Adapted use of pre-existing instrumentation, including NI DAQ cards, pulse generators, and oscilloscopes reducing cost of project significantly
- Advised rotating graduate students for several months and mentored/trained an undergraduate in the laboratory for several years
- Facilitated inter-department collaborations with Departments of Biology and Electrical Engineering
- Successfully applied for an NIH fellowship

**Boston University, Department of Biomedical Engineering,** Boston, MA

**Jan. – May, 2011 and 2012**

*Teaching Assistant, Biomedical Instrumentation*

- Instructed all laboratory experiments and taught occasional lecture, for two semesters
- Taught physiological signals, biomedical sensors, data acquisition, analog and digital filtering and processing, and an overview of medical instrumentation platforms.

**Vanderbilt Medical Center, Vascular Research Laboratory,** Nashville, TN

**Oct. 2008 – Aug. 2009**

*Research Assistant and Laboratory Technician*

- Performed experiments measuring forces from drug-induced vessel constriction/relaxation

**PharmaSys, Inc.,** Cary, NC **May 2008 – August 2008**

*Data Analysis Intern*

- Programmed auto-generating business reports for pharmaceutical consultants
- Obtained copyright for company manuals

## TECHNICAL SKILLS

**Software:** Matlab, Labview, Visual Basic, C, 3D CAD (Autodesk Inventor, Solidworks), Express PCB, ImageJ, MS Office

**Laboratory:** Optical setup, imaging, microscopy, instrumentation, data acquisition, signal processing, constructing circuits, hardware and cabling, dissection, cell culture, gel electrophoresis, circuit design

## ENGINEERING PROJECT EXPERIENCE

**Vanderbilt University Department of Biomedical Engineering,** Nashville TN

**November 2008 – May 2009**

*Senior Design Project*

- Designed a method of measuring emotional response during deep brain stimulation on a team of five

**Vanderbilt University Department of Biomedical Engineering,** Nashville, TN

**Jan. 2008 – Mar. 2008**

*Instrumentation Laboratory Project*

- Constructed a device using electrodes measuring EMG potentials in a four-member team

**Vanderbilt University Department of Biomedical Engineering,** Nashville, TN

**July 2004**

*Beta-tester and Design Consultant for an NSF-Funded Project*

- Designed affordable imaging experiments for underprivileged youths, in a team environment

## PUBLICATIONS

- *Ali H. Badreddine, Tomas Jordan, and Irving J. Bigio, "**Real-time imaging of action potentials in nerves using changes in birefringence,**" Biomed. Opt. Express 7, 1966–1973 (**2016**)*
- *Ali H. Badreddine, Kurt J. Schoener, and Irving J. Bigio, "**Elucidating the temporal dynamics of optical birefringence changes in crustacean nerves,**" Biomed. Opt. Express 6, 4165–4178 (**2015**)*

## PRESENTATIONS

- OSA Biomedical Optics Conference and Exhibition (BIOMED) **2016** | Badreddine A. H., Jordan T., Bigio I. "***Real-Time Movies of Neuronal Activity by Imaging Intrinsic Changes in Optical Birefringence.***" *(talk and poster)*
- Quantitative Biology and Physiology and Translation Research in Biomaterials Annual Symposium **2015** | Badreddine A. H., Schoener K., Bigio I. "***Live tracking of action potentials in nerves.***" *(poster)*
- Quantitative Biology and Physiology and Translation Research in Biomaterials Annual Symposium **2014** | Badreddine A. H., Schoener K., Bigio I. "***Tracking action potentials using intrinsic birefringence*.**" (talk)

## AFFILIATIONS AND AWARDS

- Professional Memberships in OSA, SPIE, BMES, Tau Beta Pi
- QBP/TRB Graduate Research Symposium, Best Poster, 2015
- Edmund Optics 2014 Educational Award (Silver), (for products for my research)
- Quantitative Biology and Physiology Fellowship through NIH, 2009–2010
- Magna Cum Laude, 2009
- College Scholarships: Hope Scholarship and Tractor Supply Company